1-1-2013

Structural Origin of Mechanical Prowess In Conch Shells

Haoze Li
University of South Carolina - Columbia

STRUCTURAL ORIGIN OF MECHANICAL PROWESS IN CONCH SHELLS

by

Haoze Li

Bachelor of Materials Science and Engineering
Harbin Engineering University, 2007

Master of Materials Science
Harbin Institute of Technology, 2009

Submitted in Partial Fulfillment of the Requirements

For the Degree of Doctor of Philosophy in

Mechanical Engineering

College of Engineering and Computing

University of South Carolina

2013

Accepted by:

Xiaodong (Chris) Li, Major Professor

Chen Li, Committee Member

Djamel Kaoumi, Committee Member

Goutam Koley, Committee Member

Lacy Ford, Vice Provost and Dean of Graduate Studies

DEDICATION

To my beloved parents

ACKNOWLEDGEMENTS

I owe my deep gratitude to all the people who have helped me for my doctoral study at University of South Carolina. First, I would like to thank my advisor, Professor Xiaodong (Chris) Li, for his insightful guidance, generous support, encouragement through every step of my research, as well as the career promotion afterwards. His passion for research has been an inspiration to my career. I would also like to thank Professor Chen Li, Professor Djamel Kaoumi and Professor Goutam Koley for serving as my committee members of dissertation review and defense. Their insightful suggestions greatly improve the quality of this dissertation.

I sincerely appreciate the financial support of China Scholarship Council during my degree pursuing. As well, I thank the kind help of Professor Morehouse and Professor Kidane for my teaching assistance job.

All the group members and colleagues are truly grateful; they are like family to me. I will always cherish the quality time spent with Dr. Zhihui Xu, Professor Gangsheng Zhang, Professor Dalai Jin, Dr. Lihong Bao, Dr. Jianfeng Zang, Dr. Yong Sun, Dr. Zaiwang Huang, Dr. Yanming He, and doctor-to-be Rui Li, Peng Huang, Yingchao Yang, Jianchao Chen, Yang Sun, Ningning Song, Zan Gao, and thank their help in both my research and daily life. The administrative staffs and technicians in the Department of Mechanical Engineering are highly appreciated.

Finally, I express deepest gratitude to my parents, my father Zhongchen Li, my mother Wenmin Zang, for their love, wise guidance and unwavering belief in me. Without you, I would not be the person I am today.

ABSTRACT

Conch shells are natural nanocomposites with an exquisite multiscale hierarchical architecture which exhibit coupled ultrahigh mechanical strength and toughness. What materials design strategy renders conch shells such mechanical prowess? In this study, micro/nanoscale structural and mechanical characterization of conch shells (*Busycon carica*) has been carried out. We demonstrate, for the first time, direct evidence that the previously claimed single-crystal third-order lamellae - the basic building blocks in conch shells are essentially assembled with aragonite nanoparticles of the size ranging from 20 to 45 nm. The third-order lamellae exhibit not only elasticity but also plasticity with the strain up to 0.7% upon mechanical loading, due to the unique nanoparticle-biopolymer architecture in which the biopolymer mediates the rotation of aragonite nanoparticles in response to external loading. Our finding - metal like deformation behavior overturns the previous assumption that aragonite lamellae are brittle in nature. The three-order crossed-lamellar architecture interlocks cracks via crack deflection along the biopolymer interfaces in a three-dimensional manner. The interlocking mechanism and the plasticity of third-order lamellae jointly contribute to the remarkable mechanical prowess.

We report that conch shells display an unusual resilience against high strain rate predatory-attack vis-à-vis under quasi-static loading. Upon dynamic loading, conch shells trigger a new defense mechanism - intra-lamella fracture, involving nanoparticle rotation and formation of trapped dislocations, which differs from the inter-lamella fracture damage under quasi-static violation.

Another fascinating design principle with the curve-shaped third-order lamellae is uncovered in conch spines. Such architecture enhances the fracture strength up to 30 % compared with that of conch shell bodies with straight reinforcements, unveiling the roles of spines in protection from predators.

Moreover, the effects of electron beam irradiation and heat treatment on the structural and mechanical stability of conch shells were investigated. Both conditions can induce phase transformation from aragonite to calcite, to lime, altering the aforementioned properties.

TABLE OF CONTENTS

LIST OF TABLES

LIST OF FIGURES

LIST OF SYMBOLS

h^*	Critical length scale
a	Proportionality constant
γ	Surface energy
E	Elastic modulus
σ_{th}	Theoretical stress
σ_{cr}	Critical buckling stress
Φ_M	Mineral content
υ	Poisson ratio
E_P	Elastic modulus of biopolymer
K_{tot}	Stress intensity factor
K^P	Stress intensity factor of primary load
K^S	Stress intensity factor of residual stress
ε	Bending strain
r	Half thickness of lamella
R	Radius of bending curvature
I	Moment of inertia
b	Width of lamella
h	Height of lamella
F	Applied load
L	Suspended length of lamella

k_n	Spring constant of lamella
k_i	Slope of Force - Piezo Z position curve
T	Temperature increment
l_0	Thickness
k_0	Thermal conductivity
R_0	Radius of hole in supporting film
r_0	Radius of irradiated region
W	Total absorbed power
ε_0	Proportional absorbed energy
V	Acceleration voltage
ρ_0	Current intensity
E_{max}	Maximum transferred energy
E_0	Kinetic energy
A	Atomic mass
m	Strain rate sensitivity
σ	Applied stress
$\dot{\varepsilon}$	Applied strain
N	Total amount of fractured third-order lamellae
Q	Energy consumption under compression
q	Energy consumption under bending
G_{Inter}	Energy release rate of inter-lamella crack tip
G_{Intra}	Energy release rates of intra-lamella crack tip
Γ_L	Fracture toughness of third-order lamella

Γ_P	Fracture toughness of biopolymer
α	Dundurs' parameter
E_L	Elastic modulus of third-order lamella
v^*	Activation volume
k_c	Boltzmann constant
T_0	Absolute temperature
$\vec{b}$	Burgers vector
σ_s	Applied stress on the cross section
τ_0	Constant friction stress
τ_C	Coulomb friction stress
σ_P	Radial compressive stress
μ	Coulomb friction coefficient

List of Abbreviations

ACC ..... Amorphous Calcium Carbonate

SEM ..... Scanning Electron Microscope

TEM ..... Transmission Electron Microscope

HRTEM ..... High-Resolution Transmission Electron Microscope

AFM ..... Atomic Force Microscope

FESEM ..... Field Emission Scanning Electron Microscope

FFT ..... Fast Fourier Transformation

EBID ..... Electron Beam Induced Deposition

EELS ..... Electron Energy Loss Spectroscopy

SAED ..... Selected Area Electron Diffraction

SRS ..... Strain Rate Sensitivity

TGA ..... Thermogravimetric Analysis

DTA ..... Differential Thermal Analysis

XRD ..... X-Ray Diffraction

RT ..... Room Temperature

FTIR ..... Fourier Transform Infrared Spectroscopy

CHAPTER 1

INTRODUCTION

The past decades are filled with humans' efforts in developing structural materials with combination of remarkable mechanical reliability (including strength, toughness) and low weight for survival and social needs. Unfortunately, it is challenging to achieve simultaneously high strength and toughness in engineered materials because of the trade-off relation between the two properties.[1] For the metallic materials, the well-performed ductility and fracture toughness are at the expense of low level yield stress. Several strengthening methods have been identified, such as micro-/nano-particulate and/or fiber reinforcements incorporation, grain size refinement (nanomaterials), dislocation introduction (for example, stacking faults).[2] However, these modifications inevitably result in elevated brittleness. On the other hand, the inherently stiff ceramic materials are short of applicable ductility as well as toughness. Although the ductile second phase, phase transformation and predesigned crack arrangement, to some extent, soften the materials with higher fracture toughness,[3] the limited amelioration together with reduced strength cannot fulfill the specific requirements. Consequently, a challenging issue is surfaced: How people can overcome such conflicting issue and fabricate strong-and-tough materials?

Knowing the best in materials-by-design for functionality, Mother Nature, however, has already elegantly solved this problem. Living organisms have evolved over millions of years to a level of optimization not currently achieved in engineered system.[4] Among these, seashells, which are acknowledged the best natural body armors for protecting their soft bodies from predator attacks, possess salient mechanical strength and eminent toughness - several times increase in stength and some thousand fold enhancement in toughness with reference to their major components.[5-8] Two major constituents, regardless seashell species, aragonite (a mineral form of $CaCO_3$) and organic biopolymer, are known to be arranged hierarchically into multiscale architecture via bottom-up self-assembly. To be specific, via converting soluble ions in water into minerals,[9] characterized as biominerlization, living organisms combine brittle ceramics and macromolecules together to form such biomaterials.[10] Within the countless seashells found underwater, they are approximately contained in five phyla, i.e., mollusca, arthropoda, echinodermata, brachiopoda and annelida. Nowadays, bivalvia and gastropoda in mollusca are frequently investigated because of their exquisite structures and availability.[9] In addition, the identifying structural morphologies are classified as prismatic, nacreous, crossed-lamellar, foliated and homogeneous.[11,12] Crossed-lamellar structure, with its complex multiscale arrangement in frequently varied orientation, is widely spotted in seashells. Their achieved unparallel mechanical and physical properties compared with man-made materials inspire scientists to biomimic counterparts.

To deepen the understanding of relationship between structure and property in seashells, we select conch shell (*Busycon carica*) as an example. As shown in Figure 1.1, the conch profiles as the high spire and a siphonal canal with several spines evenly separated at the end of swirl. Microscopically, the bulk shell consists of three microlayers (outer, middle and inner) based on their diverse orientations of first-order lamellae (Figure 1.2a). Each microlayer is comprised by horizontally overlapping numerous plate-like first-order lamellae. A first-order lamella is formed by numerous second-order lamellae, and a second-order lamella consists of a bundle of third-order lamellae which have nanoscale cross section and micro-level length (Figure 1.2b). Within a microlayer, the orientation of third-order lamellae is changed in neighboring first-order lamellae by 90^0. In the bulk shell, the orientation of first-order lamellae in the outer, middle and inner layers is varied as $0^0/90^0/0^0$.

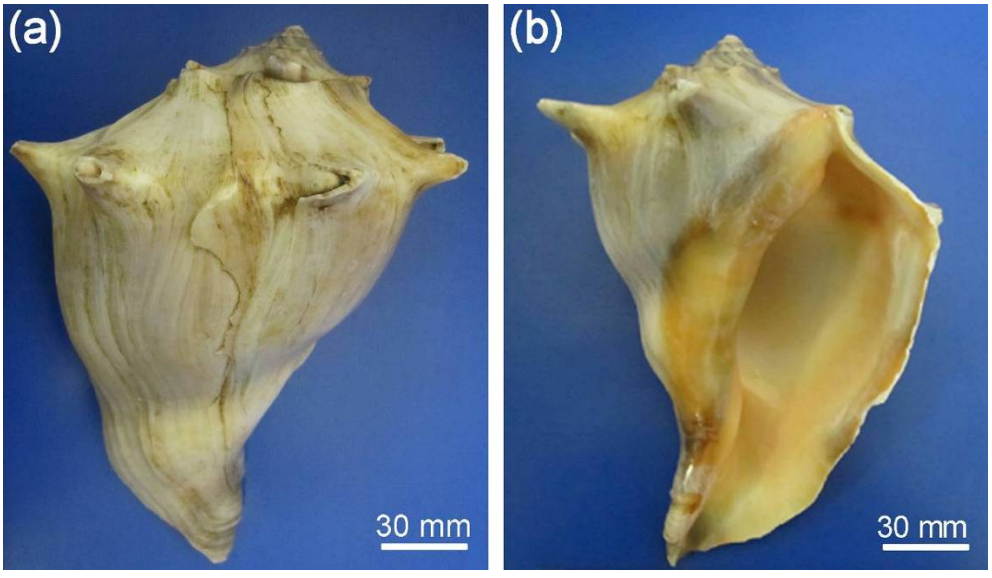

Figure 1.1. Conch shell (*Busycon Carica*) profiles. (a) and (b) are the back and front views, respectively.

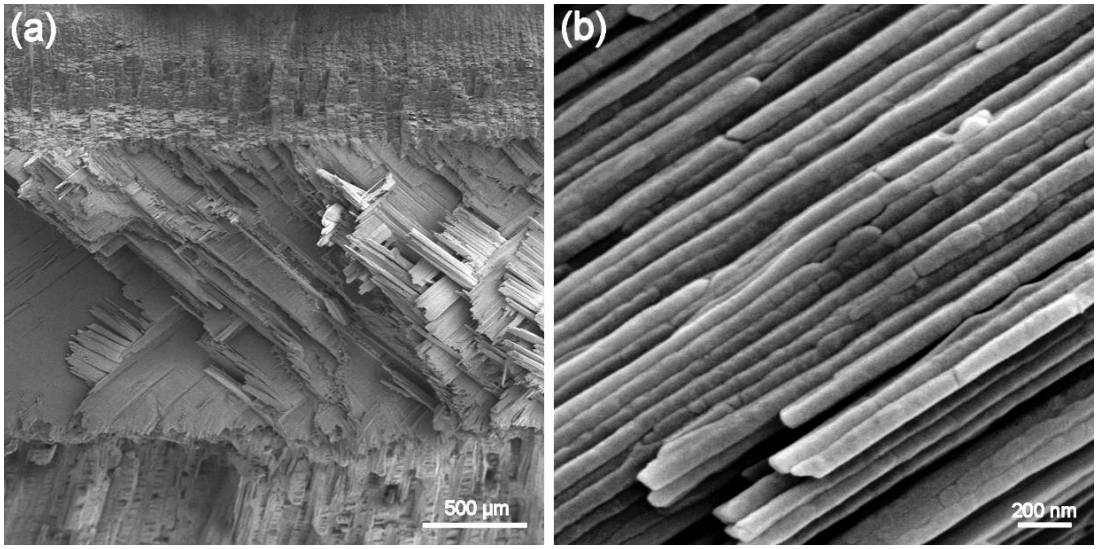

Figure 1.2. Crossed-lamellar structure of conch shell. (a) Overview of fracture surface. (b) A close-up view in showing nanoscale third-order lamellae.

1.1 ASSEMBLY STRATEGIES IN CROSSED-LAMELLAR STRUCTURE

How do the conch shells manage to achieve such compact multiscale hierarchical structure? We mainly list several growth mechanisms during biomineralization. Growth twins (Figure 1.3a) were reported in third-order lamellae within crossed-lamellar structure.[13-16] This formation with the (110) mirror plane is ascribed to aragonite crystallographic privilege, i.e. orthorhombic symmetry leads to pseudohexagonal arrangement.[17] Kitamura et al.[18] anticipated the faster growth effect of twins in crystal. The alignment of twin boundaries is in good agreement with lamellar length direction, indicating the growth path of third-order lamellae. In addition, growth twins were also found in other ceramics, for instance, calcite and vaterite.[16,18] Suzuki and Pokroy et al. observed a thin layer with crystalline particles deposited on the growing surface, demonstrating the epitaxial growth of shells.[19,20] Besides crystalline growth, the precursor

theories, including amorphous calcium carbonate (ACC) precursors and polymer-induced liquid precursors,[21-27] were proposed, respectively, to clarify the possible pathways of mineralization under ambient aqueous conditions. With the aid of precursors' mobility, it facilitates the complex construction with dissimilar orientations.

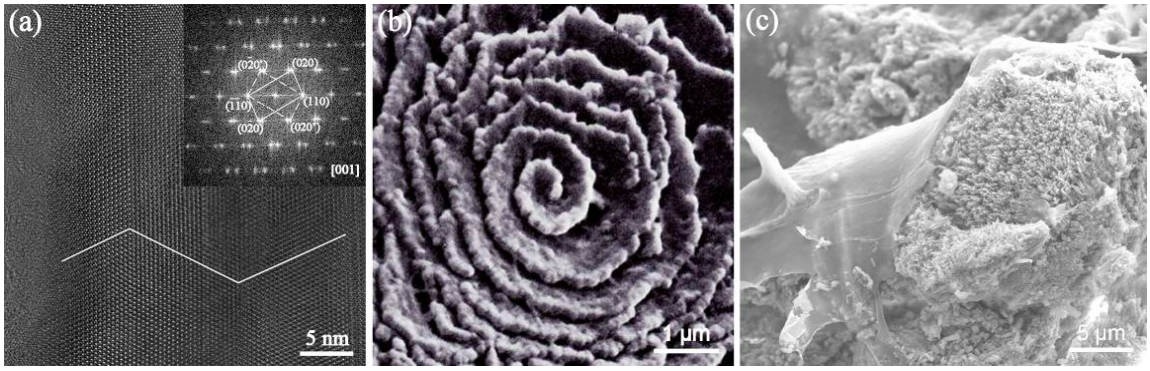

Figure 1.3. Growth theories of conch shells. (a) Growth twins inside a third-order lamella with boundaries aligned parallel to lamellar length orientation. (b) Spiral formation.[39] (c) New-born third-order lamellae in a bio-envelop.

Consisting of proteins with no more than 5% in mass, biopolymer (polymer, molecules and surfactants) exerts a tremendous influence on guiding and assisting crystal growth into the hierarchical structure, with the postulated functions as stabilizers, soft templates and additives.[19,22,28] Weiner et al. brought forth an organic-nucleation theory[29] to discuss that the protein-based matrix was inclined to bind ions at certain spots to create an appropriate plane, followed by the crystal nucleation as the local concentration is increased. Such pre-designed method creates well-ordered and desired structures. Tissue regeneration studies provided important information concerning the organic role.[30-38] Moreover, Wada and Prezant et al. found a spiral pattern (Figure 1.3b) in the edges of

growing surface.[39,40] It was proposed that the formation was affected by the higher concentration of organic matrices located along the growth frontline than the interspersed distribution of bio-protein within 'normal' lamellar pattern. Enveloped crystalline growth inside biopolymer shields was first reported by Nakahara et al.[41] A thin organic substance is first deposited on the inner surface of shell; accompanied by the mineralization, granular crystals are formed within various bio-envelopes in such organic matrix as shown in Figure 1.3c. When the thickness of layer is increased, the grown-up crystals result in the contact between adjacent envelopes and finally enclose growth lines. Oriented attachment method was first found in a hydrothermal process assembly by TiO_2 particles;[42] it has turned to a hot topic concerning biomineralization because its products' shape and nanoparticles-constructed single-crystal character are similar to biominerals. Through locking in high energy surfaces of two approaching particles, the crystallographic fusion eliminates energy to makes possible the further growth.[43,44] Thermodynamically, oriented attachment guarantees the defect free inside together with achievable intricate structure.

Most of the mechanisms listed challenge the classical crystal growth theory, known as 'Ostwald ripening process',[45] during which the crystalline nuclei first precipitate from the supersaturated liquid. After reaching as the size of 'critical crystal nuclei', the free enthalpy of the system becomes negative and therefore propels further growth at the cost of smaller ones. To date, all the studied growth models refer the individual third-order lamella as single-crystal mineral and basic building block because of the

single-crystal-characteristic electron diffraction pattern.[46-49] However, considering the listed biomineralization methods, the possibility of particles assembly strategy cannot be simply eliminated. In our work, we demonstrate direct evidence that the previously claimed single-crystal third-order lamellae in conch shells are essentially assembled with aragonite nanoparticles of the size ranging from 20 to 45 nm. To support the conclusion, we also resorted to mechanical deformation and heat treatment to reveal the nanoparticle formation. The new-finding assembly units will deepen our understanding in biomineralization.

1.2 STRENGTHENING MECHANISMS OF HIERARCHICAL STRUCTURE

The conch shells' remarkable effectiveness in combining superior strength and toughness with reference to brittle ceramics and weak organic materials attracts interests in the field of biomimicry. The following mechanisms are ascribed to the origins in strengthening bioceramics.

The wave-like third-order lamellae were found by Yang et al.;[50] such micro-scale interlocking by the advantage of curvature induces transverse dilation and interfacial hardening upon sliding, enhancing materials' strength as well as toughness. Likewise, the surface roughness of third-order lamellae owns the similar function but performs down to nanoscale. Caused by the mutual movement restriction with the help of nanoasperities, the elevated force for further slip alleviates stress concentration and initiates other deformation behaviors instead of simple fracture (Figures 1.4a and b).[51-54] Meyers et al.

reported the strengthening mechanism of mineral bridges (Figures 1.4c and d) through considering the bridge number and distribution status.[6]

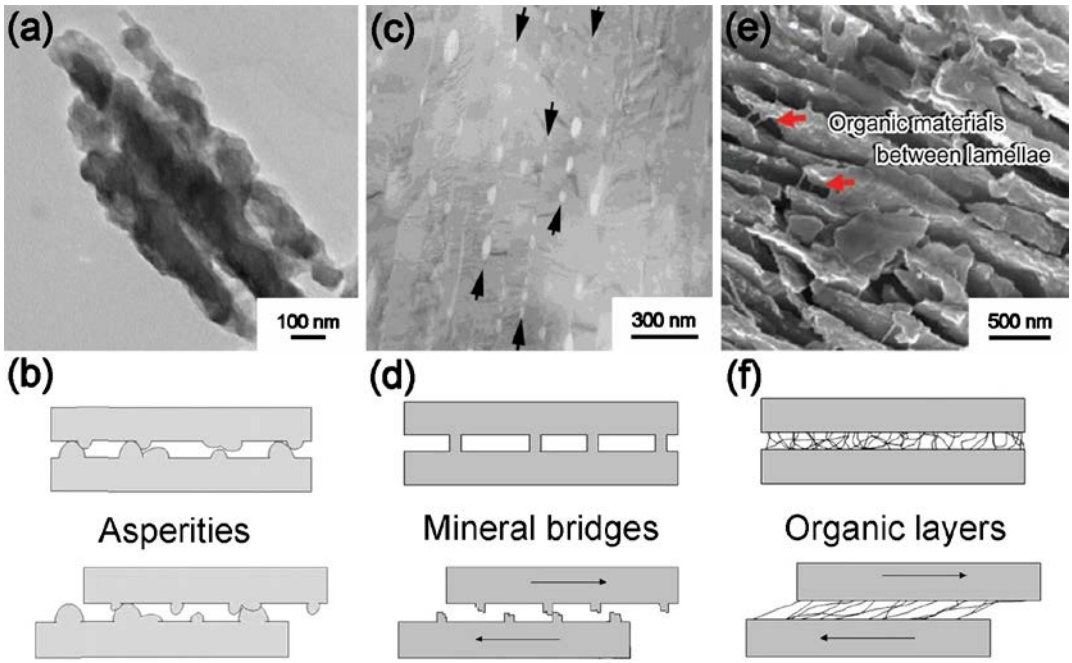

Figure 1.4. Conch shells strengthening origins. (a) and (b) Nanoasperities of third-order lamellae and corresponding deformation mechanism. (c) and (d) Mineral bridges and detailed fracture behavior, respectively. (e) and (f) Organic materials and deformation detail.[28,54]

The revealed nanoparticles in our studies exert the influence in strengthening as well. It is accepted that a defect-free material can reach its theoretical strength; however, the protein molecules between the ceramic particles are equivalent to crack flaws because of their comparably low stiffness. Gao et al.[53] investigated how biological materials achieved high strength with the preexist cracks. From the standpoint of fracture mechanics, the critical length scale (h^*) is shown as followed:[53]

$$h^* \approx a\frac{\gamma E}{\sigma_{th}^2} \quad 1.1$$

where a is a proportionality constant, γ is the surface energy, E and σ_{th} represent the elastic modulus and theoretical stress, respectively. It indicates that the fracture strength is sensitive to structural size, namely, stress concentration caused by flaws leads to failure above certain crack length. Yet the size drops down around tens of nanometers, the materials become insensitive to defects and maintain high strength.

Biopolymer is not only an irreplaceable factor during the biomineralization but also proved to possess critical roles in the point of mechanical performance despite its low content (Figures 1.4e and f). Zhao et al.[55,56] reported the declined magnitudes in both strength and ductility after heat treatment, which directly points out the importance of biopolymer. Xu et al.[57] found the strengthening phenomenon of biopolymer and proposed a coiled-spring model, both of them in turn explains the reason of weakened properties upon burning out biopolymer. Moreover, Ji et al.[58] proposed a one-dimensional model to illustrate the protein's task in transferring the load between lamellae via shear. Ji et al.[59] also proposed a multi-buckling model, differing from classical Euler buckling that stress degradation is caused by increased aspect ratio. They indicated that the buckling stress was independent of aspect ratio as long as the aspect ratio value reached high enough, especially for conch third-order lamellae with nanoscale cross section and microscale length. Equation 1.2 below provides a threshold stress value, below which the lamellae are not inclined to buckle disregarding how slender the lamellae will be.

$$\sigma_{cr} = \sqrt{\frac{2E_M E_P \Phi_M^3}{3(1-\upsilon^2)(1-\Phi_M)}} \qquad 1.2$$

Here, σ_{cr} indicates the critical buckling stress, Φ_M is the mineral content, υ is Poisson ratio, E_M and E_P are elastic moduli of mineral and biopolymer, respectively.

1.3 TOUGHENING MECHANISMS OF HIERARCHICAL STRUCTURE

Comparing with the strengthening mechanisms aforementioned, researchers own a more pressing need to investigate the achieved ultrahigh fracture toughness by assembling plain-performance constituents in conch shells. Crack deflection and bifurcation (Figure 1.5a) are widely observed and studied fracture behaviors in hierarchical structure.[4,47,49,54] The large discrepancy in stiffness between biopolymer and ceramic renders cracks find an easy way for propagation. Such delocalization of damage as well as crack branching decreases stress concentration and significantly impedes fracture process by confining in a small region. Kamat et al.[60] reported the large-scale crack bridging in crossed-lamellar structure and evaluated its contribution to the fracture toughness (Figure 1.5b). Bridged by intact elements in middle layer, the formation of delaminated cracks along the lamellar interface between outer and inner microlayers complicates the deformation behaviors in combination with Mode I loading (bending) and Mode II loading (tension). Therefore, such behavior is expected to be a softening factor (decreasing crack opening displacements) and consumes extra energy after mechanical failure. Kessler et al.[61] found the multi-cracking response after bending tests and calculated its outcome on toughening (Figure 1.5c). The cracks multiplication and

interaction bring about mutual shields and lower the stress intensity factor at the crack tip in comparison to single-crack condition. Such deformation behavior avoids catastrophic fracture and improves structural reliability.

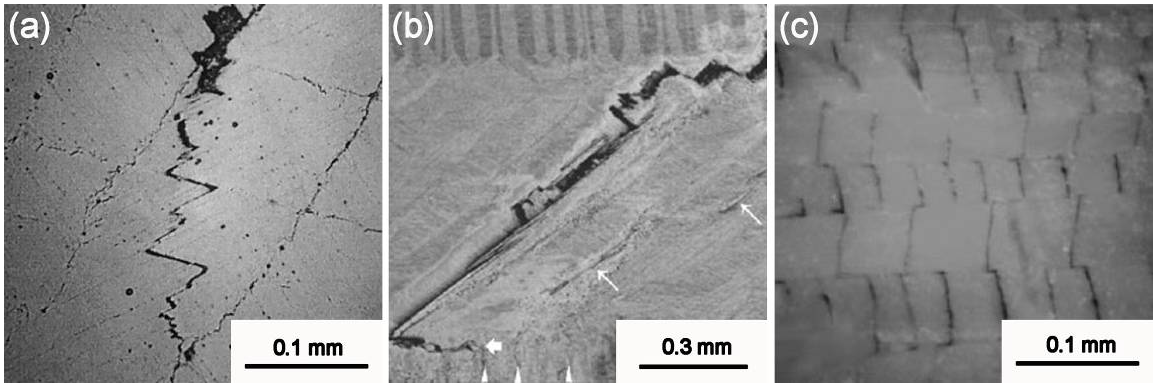

Figure 1.5. Conch shells toughening strategies. (a) Crack propagation in deflected and branched manners.[49] (b) Bridging a delamination between two microlayers.[60] (c) Multi-cracking along the lamellar interlayer.[48]

Lamellar sliding,[56] some other studies treat it as pull-out, is found in the deformed structure. It is proposed to enhance materials' performance by consuming energy under frictional sliding.[49] Besides breaking bonds of macromolecules, the sliding takes advantage of lamellae features (for example, curving lamellae, nanoasperities and mineral bridges in Figure 1.4) to increase fracture strain and materials' flaw tolerance. Cook et al.[62] studied the effect of adhesive soft bio-interface and proposed the corresponding models on the toughening mechanism. Zhao et al.[55,56] reported the absence of biopolymer not only resulted in the decreased strength but also fracture toughness. As a matter of fact, most of mentioned toughening mechanisms cannot leave the assistance of biopolymer, even the biopolymer's moisture condition affects materials' performance[63-65] by the

evidence of lessened strength and toughness upon dry condition. It is believed that the constraint macromolecules activity in transition from wet to dry condition might affect the outcome. Its viscoelastic-plastic characterization enriches the engineered synthesize field.

After listing several small-scale (including nano- and micro-scale) toughening factors, we turn our attention to the macro-size design principle - hierarchical arrangements, the original found and studied aspect. The mechanical properties of crossed-lamellar structure are mostly depended on all levels of organization's interaction. Through the frequently changed lamellar orientation, the increased crack path inhibits the thrust from propagating directly down through the entire bulk materials. Eichihorn et al.[66] reported the residual stress upon deformation inside a hierarchical structure through energy variable X-ray diffraction. Generally, such compressive residual stress functions in closing-up the existing flaws in the materials, and improve the toughness in fracture. It is known that the existence of a residual stress requires cracks to achieve increased energy to break through because an additional stress intensity factor[66] K_{tot} is introduced.

$$K_{tot} = K^P + K^S \qquad 1.3$$

In this equation, K^P and K^S represent the stress intensity factor of the primary load and corresponding formation of residual stress, respectively. The interface between different microlayers is assumed to carry out higher value of residual stress than the rest in bulk materials, since the lamellae orientation is drastically changed and/or this stress might have been already formed during the biomineralization. A greater cracking force is

accordingly acquired for further growth and propagation through the region with residual stress.

Until now, all the studied deformation mechanisms mainly focus on the interaction between stiff ceramic-lamellae and soft biopolymer, little attention is paid to the mechanical contribution of individual third-order lamellae. In this work, we display direct evidence that the ceramic based third-order lamellae exhibit not only elasticity but also plasticity upon mechanical loading. Our findings in metal like deformation behavior, for the first time, prove the role of lamellae as both deflecting cracks into interlayer and performing plasticity to shield cracks from breaking through directly, and overturn the previous assumption that aragonite lamellae are brittle in nature. The plasticity provides a new solution to account for the ultrahigh robustness of conch shells.

The reported mechanical performance is based on the traditional mechanical tests under quasi-static loading rates, such as bending,[4,46,48,56,60,61] compression,[49,50,67] indentation,[55,68,69] shear. Few efforts shed light on the encountered aggression of body armors in daily life - dynamic penetration impacts. In the study, we unveil that conch shells display an unusual resilience against predatory attacks by a series of uniaxial compression under diverse loading rates. In high-strain-rate compression (strain rate ~ 10^3 /s) shells highlight significantly high fracture strength vis-à-vis under quasi-static loading (strain rate $\leq 10^{-2}$ /s). The natural body armors ingeniously activate a new defense mechanism - intra-lamella fracture against high-speed attacks, which differs from the inter-lamella fracture damage upon quasi-static violation. This strain-rate-dependent

self-strengthening mechanism is inherently associated with the small localized activation volume for deformation.

Conch shell bodies have been repeatedly placed as the priority for investigation in structure and mechanics. As the primary tool against predatory attacks, no effort has been undertaken on the conch spines. Accordingly, we report one prominent design principle in spines with curve-shaped third-order lamellae. Such biocomposites' assembly strategy significantly enhances the fracture strength up to 30 % compared with that of conch bodies in straight reinforcements, proving the roles of spines in protection. The mechanical improvement is ascribed to the curvature effect in breaking reinforcements in lieu of sliding effect in conch bodies.

The original design of shells by Mother Nature is for the application under environmental temperature. Yet, considering the structural and mechanical stability upon high temperature, the heat treatments at 310 °C, 500 °C and 900 °C were performed. It is reported that low-content biopolymer, which can be easily burned out in the studied heating conditions (310 °C), exerts a significant role in maintaining high mechanical performance. The phase transformation (aragonite - calcite at 500 °C, calcite - lime at 900 °C) induces structural modification and deteriorates mechanical stability.

CHAPTER 2

ASSEMBLY STRATEGY AND MECHANICAL PROWESS IN CONCH SHELLS

Conch shells are renown for their unique three-order crossed-lamellar aragonite structure (99 vol.%) integrated with biopolymer (1 vol.%),[47,48,60,68] providing three dimensional crack deflection pathways upon mechanical loading.[46,49,56,61] To date, the mechanical prowess has not been completely clarified. Their structrual details and how they coordinate and jointly contribute to the mechanical robustness are still, to a large extent, unknown.[70-72] It has been long thought that the basic building blocks in conch shells are the third-order lamellae which are single crystal aragonite and brittle.[46-49] Recent studies on nacre, which consists of stacked aragonite platelets sandwiched with organic biopolymer, have revealed that the previously assumed basic building blocks - aragonite platelets - are actually composed of a large number of nanoparticles with an average particle size of 15-180 nm.[7,73,74] Several key questions are raised, but not answered: Are aragonite nanoparticles also the basic building blocks for conch shells in view of similar biomineralization among seashells? If so, how are the aragonite nanoparticles assembled into the three-order crossed-lamellar architecture? How do such multiscale hierarchical three-order lamellae coordinate to protect the soft body from foreign (mechanical) attacks? Can we learn from this to produce conch shell-like materials with multiscale hierarchical

architecture to achieve the same mechanical prowess? To address these critical questions, we need to probe the aragonite nanoparticles in conch shells to advance our understanding of the coordination mechanism among the three-order lamellae with reference to their roles in the shell's mechanical performance. In this context, we applied a combination of state-of-the-art methods including scanning electron microscopy (SEM), transmission electron microscopy (TEM), atomic force microscopy (AFM), and micro/nanoindentation to conch shells to reveal the multiscale hierarchical assembly strategy and mechanical prowess in conch shells with the goal of reproducing conch shell's performance in engineered materials.

In this paper, we report, for the first time, that the previously assumed single crystal third-order lamellae are essentially assembled with nanoparticles of the size ranging from 20 to 45 nm. The aragonite-nanoparticle-constructed third-order lamellae are not brittle, but ductile. The multiscale hierarchical architecture interlocks cracks via crack deflection along the interfaces in all three-order lamellae, thus confining the damage in a small region. The findings advance the understanding of the mystery of conch shell's mechanical robustness, provide additional design guidelines for developing bioinspired nanomaterials, and lay a constitutive foundation for modeling the deformation behavior of seashells.

2.1 EXPERIMENTAL

In this study, structural and mechanical characterization was performed on the specimens cut from conch shells (*Busycon carica*), which belong to a member of the

Melongenidae family. The shells were retrieved from the South Carolina coast along the Atlantic Ocean. After cleaning-up, all samples were kept in the wet condition for mechanical tests. Macroscopic bending tests were carried out with an aim to investigate shell's fractured surface and the resistance to deformation and fracture. In addition, the residual segments of interest were treated in 1% KOH solution for 2 h, followed by 2 min distilled water ultrasonication for the observation of nanoparticles inside individual third-order lamellae. The fracture surfaces were coated with a 10 nm thick gold-film before field emission scanning electron microscopy (FESEM) (Zeiss ultra plus thermal field emission scanning electron microscope) observation. The samples for high resolution transmission electron microscopy (HRTEM) observation were prepared by slicing the shell with microtome (Microm HM 325 Rotary Paraffin Microtome, Thermo Fisher Scientific Inc., Kalamazoo, MI) and then transferred onto the holey carbon-coated copper film for the observation in a JEOL JEM 2100F transmission electron microscope (JOEL Ltd., Peabody, MA) at an accelerating voltage of 200 kV.

The mechanically polished samples for indentation and AFM observation were first cut with a water-cooled, low-speed diamond saw, then ground and polished using abrasive papers and powders of 50 nm in size, and finally rinsed thoroughly with distilled water prior to testing. Nanoindentation tests were executed using a Triboscope nanomechanical testing system (Hysitron Inc.) in conjunction with the Veeco AFM system (Veeco Dimension 3100 AFM system, Veeco Metrology Group, Santa Barbara, CA). The Hysitron nanoindenter monitored and recorded the load and displacement of the

indenter, a diamond Berkovich three-sided pyramid with a force resolution of about 50 nN and displacement resolution of about 0.1 nm. Microhardness tests were conducted on the mechanically polished shell specimens using a four-sided, pyramid Vickers diamond indenter by holding the indenter tip at the peak indentation load of 2 N for 15 s. The polished surfaces and indentation impressions were examined by AFM.

2.2 RESULTS AND DISCUSSION

As schematically demonstrated in Figure 2.1b with reference to Figure 2.1a, the conch shell has the 'plywood'-like architecture constructed with three microlayers, termed as bottom, middle, and top microlayers. The third-order lamellae, reported to be the basic building blocks for the shell structure, have the dimension of 60-150 nm by 120-330 nm in cross section and hundreds of micrometers in length. The individual third-order lamellae are bundled up with biopolymer to form the larger structure - the second-order lamellae with 5-30 μm in thickness and 20-50 μm in width. Likewise, the second-order lamellae are stacked together to form the first-order lamellae of 10-70 μm in thickness and several micrometers in width. By horizontally overlapping the first-order lamellae, a microlayer is hereby constructed. From one microlayer to the next, the orientation of the first-order lamellae differs by 80^0~90^0. In addition, third-order lamellae, oriented at 35^0~45^0 to the bulk material's surface, are organized in about 90^0-difference orientation within the adjacent first-order units. Such multiscale hierarchical arrangements render the shell three-dimensional (3D) pathways for crack deflection and

energy dissipation. The following section will elaborate the correlation between the multiscale hierarchical assembly strategy and mechanical prowess in the conch shells.

Figure 2.1a presents an overview of the fracture surface of a conch shell. The close-up views of the fracture surface (Figures 2.1c-k) reveal that cracks were deflected along the lamellar interfaces, i.e., first-order (Figures 2.1c and d), second-order (Figures 2.1e and h) and third-order lamellar (Figures 2.1i and k) interfaces. These crack induced lamellar separations indicate that cracks were simultaneously deflected in a three dimensional manner at different hierarchical levels. Served as integrated shields with frequently-varied lamellar orientations, the three microlayers (top, middle and bottom layers) deflect and branch cracks between layers, preventing the plain intrusion from the top layer directly down to the bottom layer.

To simulate the predators' sharp-teeth attacks that a conch shell often encounters in deep sea, a Vickers indenter was used to intrude the shell and the resulting damages are presented in Figure 2.2. The top, middle, and bottom layers exhibit similar damage patterns (Figures 2.2a-c). Upon indentation, the indenter generated the stress concentrations around the corners of the indenter tip. Unlike polycrystalline metals and ceramics in which cracks initiate at each corner of the indenter and further propagate along the corners/diagonals, the conch shell exhibits feather-like feature with short major cracks (as shown in Figures 2.2a-c) scattering along the indenter margins. This cracking pattern differs from the single long major cracks at each corner of the indenter observed in geological aragonite.[75]

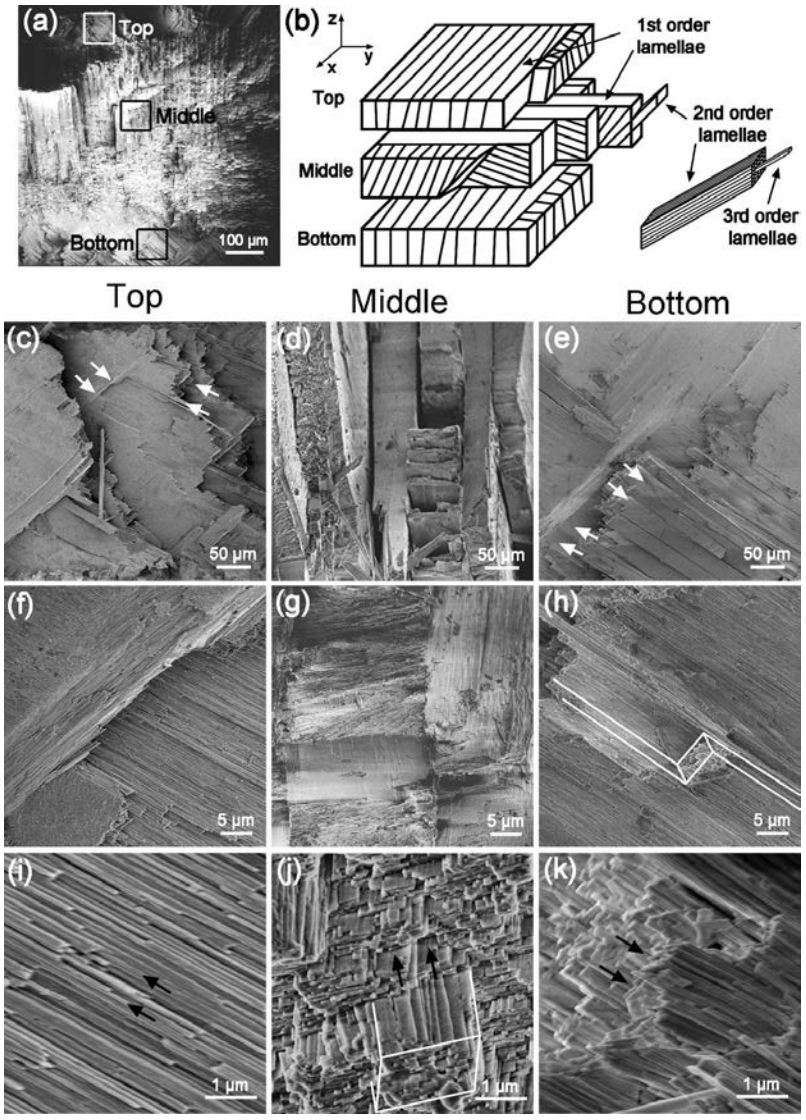

Figure 2.1. SEM images of fractured shell surface and schematic of crossed-lamellar architecture. (a) Low magnification image showing three microlayers. (b) Schematic of hierarchical structure with identification of each order lamella. (c), (f) and (i); (d), (g) and (j); (e), (h) and (k) are the images of fractured top, middle, and bottom layers, respectively, at different magnifications. Top (c) and bottom (e) layers have the same lamellar architecture orientation; and first-order lamellar interface is the preferential choice for crack propagation. The displayed edges of first-order lamellae illustrate the crack pathways along and perpendicular to second-order lamellar interfaces (indicated by white arrows).

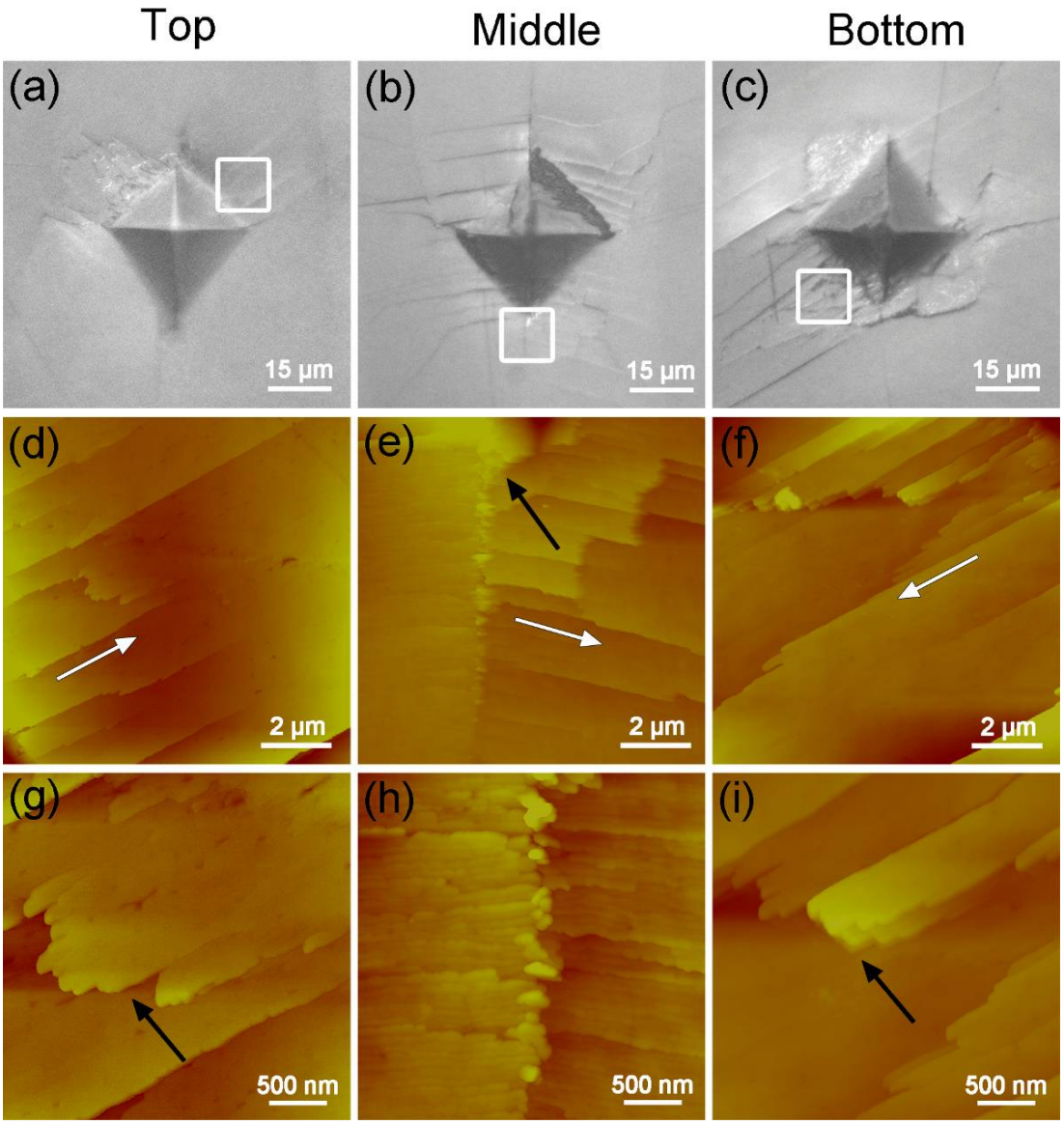

Figure 2.2. Optical and AFM images of the microindentation fractured conch surface. (a–c) Optical images of microindentation marks on the different layers of polished shell surface. (d–i) AFM images of the boxed areas in Figs. (a–c). (d–f) The white arrows show the orderly linear cracks along the second-order lamellar interfaces. (g) and (i) Cracks traverse lamellae as indicated by the black arrows.

In conch shells, the short major cracks formed primarily at the first-order lamellar interfaces if the indenter was positioned with the stress level high enough to initiate cracks, as indicated by the black arrow in Figure 2.2e. As deflected into first-order

lamellar interfaces, the cracks were further branched along second- and third-order boundaries, as indicated by the white arrow in Figure 2.2e. Some other major cracks propagated along the second-order lamellar interfaces, as indicated by the white arrows in Figures 2.2d and f. The close-up AFM images reveal that a few quite short cracks were also formed along the corners of the indenter (see the upper part of Figure 2.2f). Indicated by black arrows in Figures 2.2g and i, these short cracks were terminated by breaking through lamellae. Moreover, the formation of step-like surfaces (Figures 2.2g - i) from well-polished cross sections demonstrates the third-order lamellae were squeezed in and out upon deformation. Clearly, the three orders of lamellae jointly contribute to the mechanical prowess of the shell via buffering cracks in a three dimensional manner, confining the damage to a relatively small volume. The elongated crack paths in conch shells provide evidence for enhanced toughness.

It has been long thought that the third order lamellae are brittle single crystal aragonites. However, only few broken lamellae were observed on the fracture surface of the shell (Figure 2.1). This raises the question: Are the aragonite lamellae ductile? To answer this question, nanoindentation tests were performed on individual third-order lamellae. To eliminate the anisotropic effect studied by Bignardi et al.[76], the loading direction was arranged at the same angle (~ 45^{o}) to the orientation of third-order lamellae for all three microlayers. As a result, three microlayers (top, middle and bottom) have similar mechanical properties, as displayed in Table 2.1. The similarity in mechanical

properties indicates the assembly strategy and constituents are identically applied in all three microlayers.

Table 2.1. Young's moduli and hardness values from different microlayers of the conch shell.

	Young's modulus (GPa)	Hardness (GPa)
Top	89.1 ± 5.2	5.6 ± 0.3
Middle	89.0 ± 7.1	5.8 ± 0.4
Bottom	83.2 ± 7.3	5.7 ± 0.5

Mean values and standard deviations.

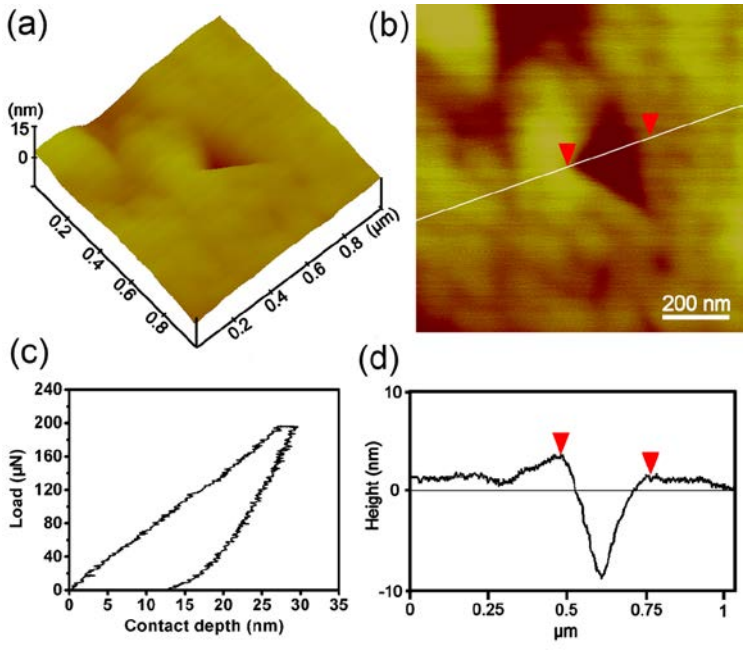

Figure 2.3. Nanoindentation characterization. (a) and (b) AFM images of a nanoindentation mark on the polished shell surface. No crack is found around the indentation area. (c) A representative load-displacement curve. (d) A cross-sectional surface height profile of the indent in (b), the pile-up formation indicates occurrence of ductile deformation.

Figure 2.3 displays a representative nanoindentation load-displacement curve, the corresponding indentation impression and cross-sectional surface height profile. Surprisingly, no cracks were found on inspection of the area around the indent (Figures 2.3a and b), moreover, the pile-up[77] was evident in the cross-sectional surface height profile (Figure 2.3d), pointing toward ductile deformation. Such observed behavior overturns the previously-assumed brittle characteristic for the conch shell aragonite. How do so-called brittle aragonite lamellae exhibit ductility? Below we elucidate the structural origin that renders ductility of the third-order lamellae.

Figure 2.4 shows the AFM and SEM images of the third-order lamellae. The AFM and SEM images jointly uncover nanoparticles with a diameter ranging from 20 to 45 nm in individual third-order lamellae. These nanoparticles are assembled to form individual third-order lamellae. The cross-sectional view of the third-order lamellae (Figures 2.4b, d and f) unveils that a single third-order lamella is not just a string of nanoparticles, but composed of a few bundles of nanoparticle strings. The AFM phase images (Figures 2.4c and d) further reveal that the nanoparticles are glued up into the third-order lamellae by the biopolymer. Our previous study[74] showed that KOH solution could etch off the biopolymer phase in seashells, but preserved the aragonite phase. Accordingly, the SEM images of the conch shell after 1% KOH solution treatment (Figures 2.4e and f) further validate the findings observed in AFM.

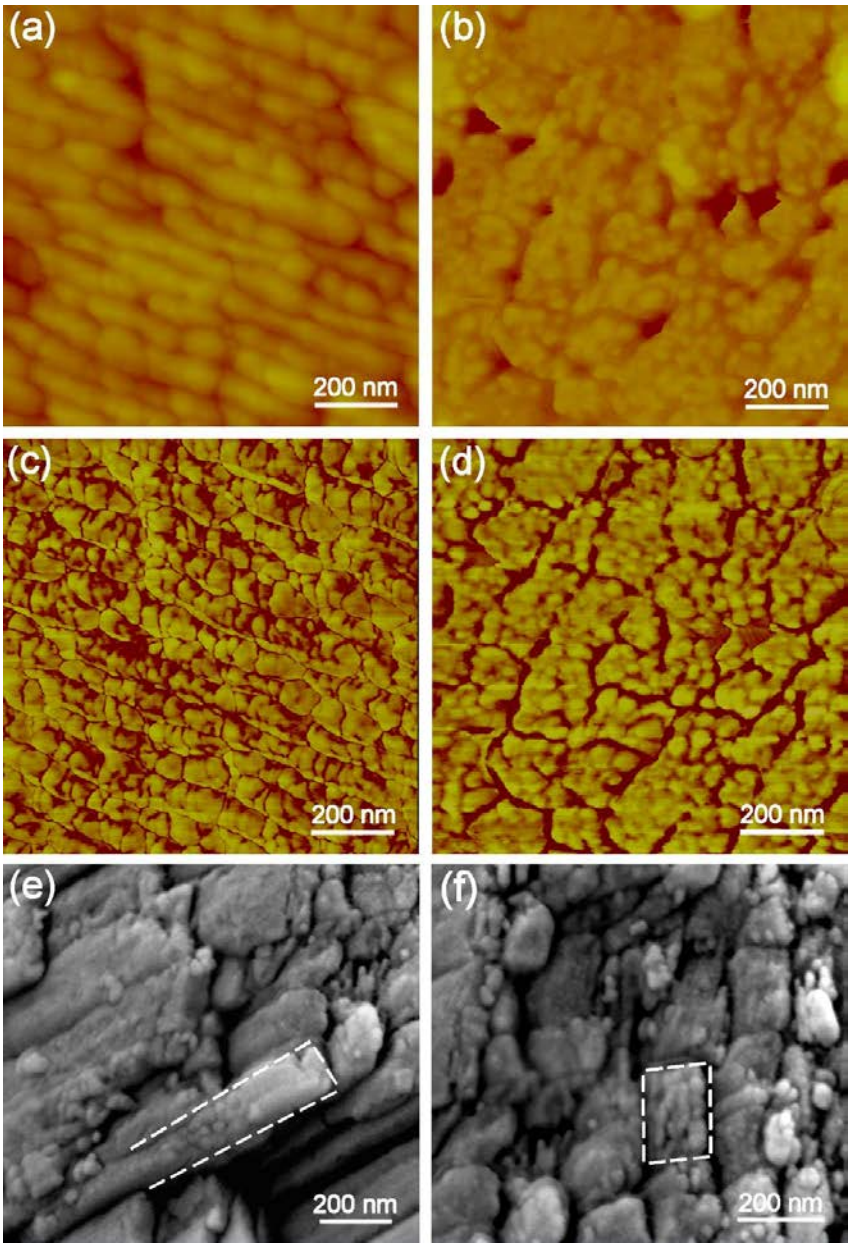

Figure 2.4. Nanostructure details of the conch shell. (a) and (b) AFM height images of cross and longitudinal sections. (c) and (d) Corresponding AFM phase images from (a) and (b), unveiling nanoparticles within individual third order lamellae. (e) and (f) SEM images in both directions after KOH resolution treatment.

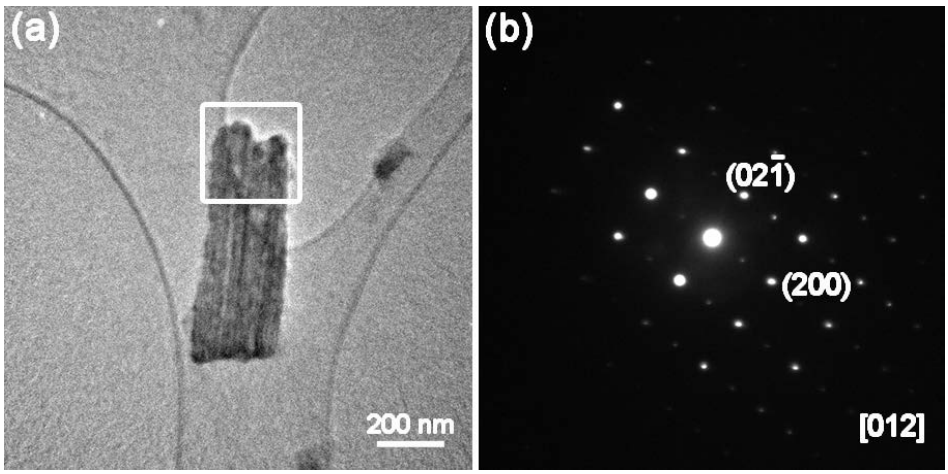

Figure 2.5. Structural characterization of the third-order lamellae. (a) TEM image of a bundle of third-order lamellae. (b) Electron diffraction pattern from the boxed area of (a), displaying the single-crystal diffraction characteristic.

Previous studies have shown that the third-order lamellae diffract as single-crystal in transmission electron microscopy.[48,60,61] Likewise, we obtained the single-crystal diffraction pattern (a series of regular spots) from a bundle of third-order lamellae in Figure 2.5, which is apparently in contradiction to our AFM and SEM discoveries (Figure 2.4) that individual third-order lamellae are polycrystalline materials. To puzzle out the nanoparticle assembly mechanism, HRTEM was resorted to probe the atomistic structure of third-order lamellae.

Figure 2.6 shows the HRTEM images and respective fast Fourier transformation (FFT) patterns of a part of third-order lamella. The electron diffraction pattern of the single third-order lamella exhibits polycrystalline characteristics (as indicated by the irregular pattern in Figure 2.6a'), indicating that individual third-order lamellae consist of

nanoparticles. This is in good agreement with the AFM and SEM observations (Figure 2.4). The FFT analysis reveals that these nanoparticles are aragonite (Figure 2.6a'). Close-up views of lattice images and corresponding FFT patterns of the four boxed areas b, c, d and e in Figure 2.6 reveal that areas b, c, and d have different crystal orientations, indexed as [101], [212] and $[\bar{1}2\bar{3}]$ zones, respectively. When the three diffraction patterns are superposed (Figures 2.6 b"+c"+d"), they form a polycrystalline diffraction pattern (Figure 2.6a"). The finding of aragonite nanoparticles inside individual third-order lamellae overturns the conventional single-crystal concept.

The next question is how these aragonite nanoparticles are assembled into individual third-order lamellae? We found amorphous phase (biopolymer) in the interstitial sites among nanoparticles, as shown in boxed area e in Figure 2.6e. This suggests that amorphous aggregation is an assembly mechanism during biomineralization process. The amorphous layer between nanoparticles holds the surrounding nanoparticles together to form robust individual nanowire-like third-order lamellae. Upon mechanical loading, the viscoelastic-plastic biopolymer between nanoparticles acts as “rubber-bands” and thus facilitates the particle rotation,[78-81] contributing to the deformability of individual third-order lamellae. This also can explain why only few broken lamellae were observed on the shell’s fracture surface and the pile-up was seen around the nanoindentation impression (Figure 2.3d). The pile-up might result from the rotation of nanoparticles and the deformation of the biopolymer between the nanoparticles.[80]

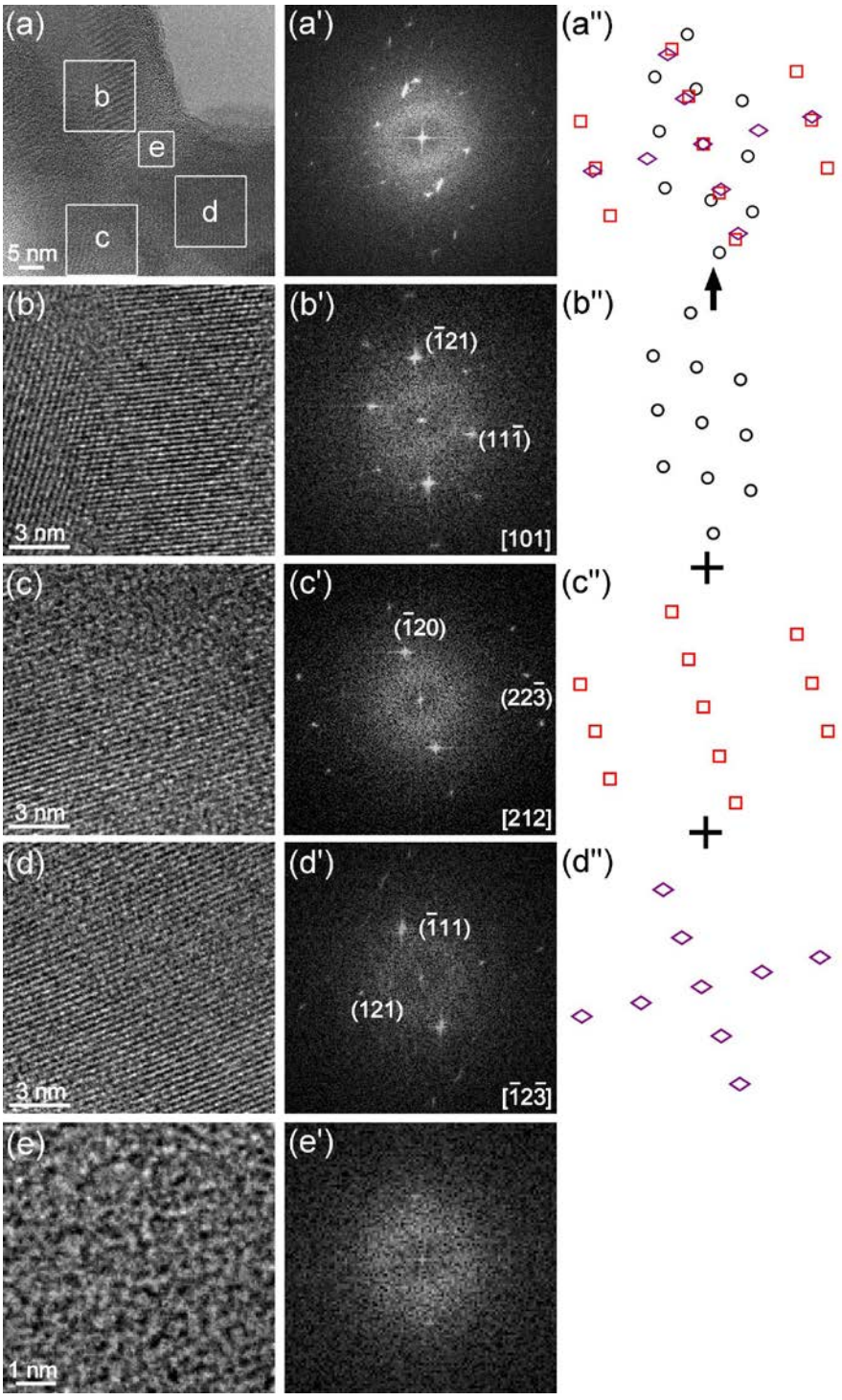

Figure 2.6. Polycrystalline diffraction characteristic of a third-order lamella. (a) HRTEM image of a third-order lamella. (b–e) Close-up views of the boxed areas b, c, d and e in (a). (a'–e') Corresponding FFT patterns of (a–e). (a''–d'') Schematic diagrams of the FFT patterns from corresponding images showing (b'') + (c'') + (d'') = (a'').

2.3 SUMMARY

In summary, the conch shell is a highly organized composite with a unique three-order crossed-lamellar architecture specially designed to protect the soft body from foreign (mechanical) attacks. The basic building blocks in the conch shell are aragonite nanoparticles that are used to construct the third order lamellae. Such nanoparticle-constructed third-order lamellae are not brittle, but ductile. The three orders of lamellae jointly contribute to the mechanical prowess of the shell by buffering cracks in a three-dimensional manner, confining the damage to a relatively small volume. The three microlayers (top, middle and bottom layers) serve as integrated shields with different lamellar orientations with the purpose of deflecting and branching cracks between layers, thus preventing the crack intrusion from the top layer directly down to the bottom layer. The findings advance the understanding of the mystery of conch shell's ultra-high mechanical robustness, provide additional design guidelines for developing bioinspired nanomaterials, and lay a constitutive foundation for modeling the deformation behavior of seashells.

CHAPTER 3

METAL-LIKE DEFORMATION IN CONCH SHELLS

It has long been assumed that the basic building blocks of conch shells are aragonite third-order lamellae characterized as single crystal and brittle. However, we revealed the nanoparticles-constructed third-order lamellae in the recent studies.[82] Relative studies on conch shells' remarkable toughness persist on the three-dimensional crack propagation along the weak biopolymer bio-interlayer because of the large discrepancy in mechanical stiffness between aragonite and biopolymer.[68] Few efforts have been undertaken towards the mechanical roles of individual third-order lamellae. Extensive work on nacre, which consists of stacked nanoparticles-assembled aragonite platelets sandwiched with organic biopolymer, has shown that the toughening strategy is not simply derived from the zigzag breakage along the biopolymer interlayer between staggered arrangements of aragonite platelets. The revealed nanoparticles inside platelets also blunt cracks from invading straightforward via an intergranular manner.[83] Accordingly, several critical questions are raised, yet not addressed in conch shells: What is the deformation behavior of a single third-order lamella? In lieu of the identified toughening mechanisms in conch shells, is there any unexplored factor? Could the new-finding nanoparticle-assembly strategy

contribute to the conch shells' eminent toughness? Can we learn from this to biomimic counterparts?

In this paper, via conducting tensile and three-point bending tests on bulk shells as well as nanoscale three-point bending on individual third-order lamellae, we display direct evidence for the first time that ceramic-based third-order lamellae, surprisingly, exhibit not purely elastic but also plastic deformation like metals upon external loading. Mediation of nanoparticles assisted by surrounded biopolymer is anticipated to the origin of such plasticity. This metallic performance renders cracks stumble in propagating straightforward through lamellae, leading to the amelioration in fracture strength and toughness. Moreover, the plasticity of third-order lamella is further improved with the aid of electron-beam induced phase transformation from aragonite to calcite and lime. The findings could open up new avenues for designing bio-inspired materials and electron-irradiation sensors.

3.1 EXPREIMENTAL

Bulk specimens for three-point bending were cut by water-cooled, low-speed diamond saw into the desired dimension (1.8 mm × 1.8 mm × 11 mm). Likewise, the testing segment of standard-shape tensile samples was machined in the dimension of 3 mm by 3.5 mm in cross section and 8.5 mm in length. To minimize man-made defects during preparation, samples were mechanically ground, polished and finally rinsed thoroughly with distilled water prior to testing. The fractured specimens were coated with

a 10 nm thick gold-film before the fractography observation with field emission scanning electron microscope.

Nanoscale three-point bending tests were carried out on individual third-order lamellae. Specimens were first detached into water via ultrasonication, and dropped onto silicon trench with 1.5 μm in width and 0.2 μm in depth afterwards. We utilized electron beam induced deposition (EBID) to clamp both bridging channel ends in scanning electron microscope (FEI Quanta 200),[81,84] as the mounted carbonaceous materials (paraffin) can avoid sliding during bending tests. A Veeco AFM system performed the bending by indenting directly onto the individual suspended lamellae which stretched across channels.

Transmission electron microscope (JEOL 2010) and high-resolution scanning transmission electron microscope (STEM, JEOL 2010F) with both operating voltages at 200 kV were combined to perform *in situ* bending tests of third-order lamellae. Dispersed lamellae were randomly distributed onto the TEM grid with a pre-cracked colloidal/carbon thin film for easy tangle and fixation. Under irradiation/heating by electron beam, the shrunken thin film caused by polymerization initiated the bending. Here, the beam current density used for illumination was in the range of 1.5×10^{-4} and 1×10^{-2} A cm^{-2}, depending on the value of magnification. To study the irradiation effect on the content of elements, we employed electron energy loss spectroscopy (EELS) for analysis. The EELS spectra were obtained via Gatan Digitalgraph and Digiscan system with a Digiscan camera.

3.2 RESULTS AND DISCUSSION

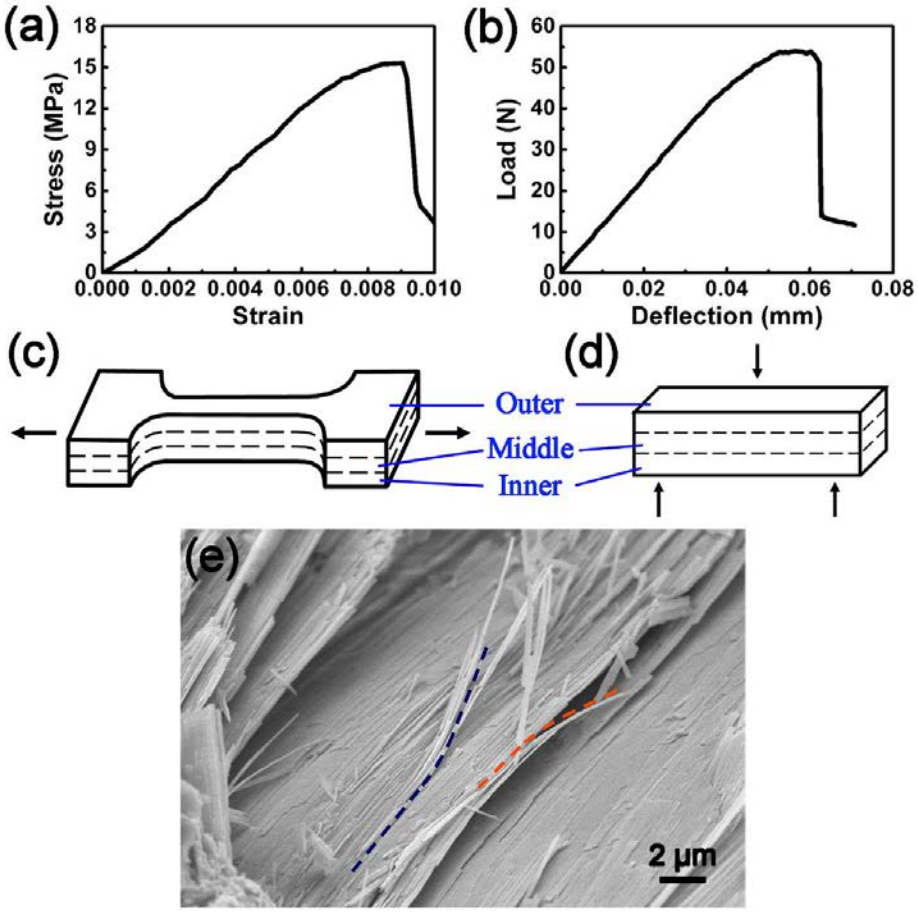

Figure 3.1. Inelastic deformation of conch shells. (a) A representative stress-strain curve upon tension with the loading direction showed in (c). (b) A load-deflection curve of three-point bending with the oriented loading displayed in (d). (c) Fracture morphology of the bended sample. The curved third-order lamellae clearly indicate the occurrence of plastic deformation.

Displayed in Figures 3.1a and b, conch shells yielded after the preliminary elastic response upon both tensile and bending conditions. The occurrence of bulk inelasticity redistributes stress and realizes the high fracture toughness of bioceramics. It is generally accepted that such strain hardening originates from the sliding resistance against pull-out

of lamellae in virtue of the interlayer features, i.e., lamellar nano-asperities, biopolymer bond.[51,52,85] Surprisingly, we found curved third-order lamellae (Figure 1c) with bending strain up to ~ 0.7 % (calculated in Equation 3.1[86]) in the fractured specimen:

$$\varepsilon = (r/r + R) \times 100\% \quad 3.1$$

where r and R are the half thickness of lamella and radius of bending curvature, respectively. This nonreversible curvature suggests the plastic deformation of ceramic-based third-order lamellae, which has never been reported before. Therefore, lamellae not only deflect cracks into 'easy' interlayer but also perform plasticity to shield cracks from breaking through directly, contributing greatly to the exhibited inelasticity as well as robustness. Our new findings overturn the inherent cognition of brittleness in bioceramics. To validate the observation, nanoscale three-point bending tests were carried out on individual third-order lamellae.

On basis of the nanoscale three-point bending (Figure 3.2a), elastic modulus (E) of lamella with two ends fixed can be calculated as:[87,88]

$$E = FL^3/192d_nI = k_nL^3/192I \quad 3.2$$

where I is the moment of inertia, determined as $I = bh^3/12$ for the rectangular cross section, b and h represent width and height of tested lamella, respectively. F is the applied load; the suspended length of lamella is denoted as L. Spring constant of lamella (k_n) is obtained as followed:[87,88]

$$k_n = k_1k_2/k_1 - k_2 \quad 3.3$$

where the quantities k_1 and k_2 are determined by slopes of Force - Piezo Z position curves upon indenting lamellae non-suspended and suspended over the trench, separately. Based on the experimental results in this work, elastic modulus (E = 96 ± 8 GPa) of third-order lamellae is hereby obtained for the first time.

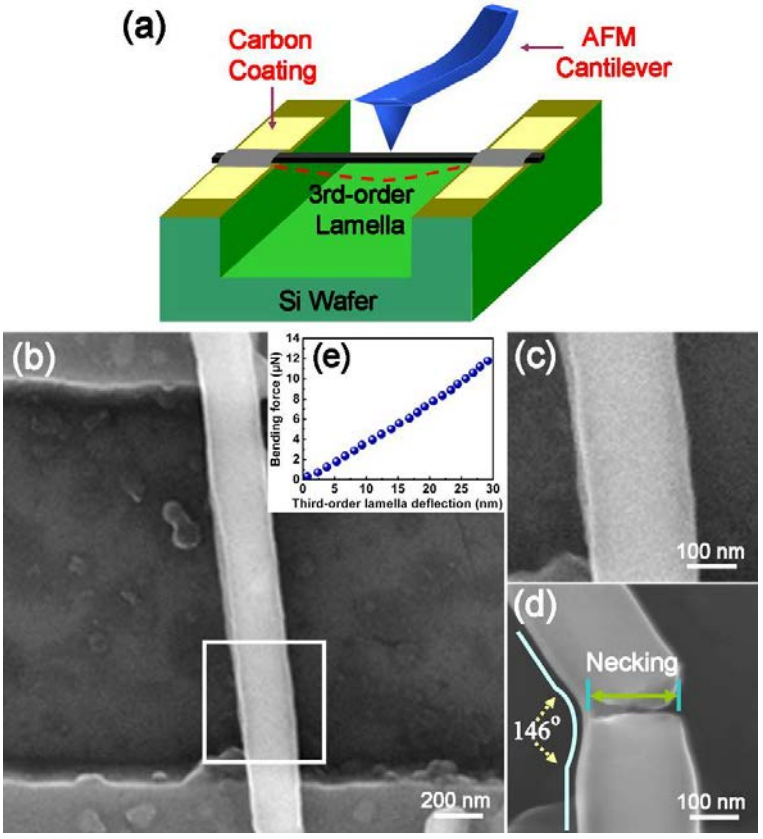

Figure 3.2. AFM three-point bending on a single third-order lamella. (a) Sketch of the bending setup. (b) An SEM image shows a fixed lamella over the trench. (c) and (d) Close-up views of lamellar pre- and post-deformed profiles within the boxed area in (b). Formation of necking and kink in (d) confirms the plastic deformation in studied material. (e) Corresponding force-deflection curve.

In comparison with well-rounded third-order lamella before bending (Figures 3.2b and c), the appealing phenomena of necking and high-angle kink at 34^0 demonstrate the metal-like plastic deformation of lamella upon external loading. The calculated ~ 0.7% bending strain[86] from Figure 3.2e is consistent well with the finding in Figure 3.1c. In view of strain-rate-dependence performance of bulk shells and other reported nanomaterials,[49,89] our bending strain rate at 10^0 /s (based on the AFM tip approaching speed and sample dimension) triggers us to investigate: What is the metallic performance under much lower strain rate?

As illustrated in Figures 3.3a - f, an *in situ* bending test was carried out under TEM observation. Generated via shrinking the supporting film upon electron beam irradiation,[90] the studied lamella was steadily forced to bend at a lower strain rate (~ 10^{-3} /s) compared to that of AFM bending. The achieved bending strain at 9.1 % stands in stark contrast to the aforementioned value (0.7 %) under AFM mode. Despite the existence of strain-rate performance, such large plastic discrepancy between two loading conditions seems implausible to be simply compensated by adjusting rates. Considering the bending condition under electron beam irradiation, the striking electrons might affect the increment. After closer examination (Figure 3.3g) of the blue boxed area in Figure 3.3e, the angle between (200) planes of two referenced particles (A and B) was veered from 12.2^0 to 7.9^0 (Figure 3.3h) upon elongated 20 s illumination, indicating the role of electron beam irradiation in bioceramic structural modification. To validate this observation, *in situ* irradiation analysis was subsequently carried out.

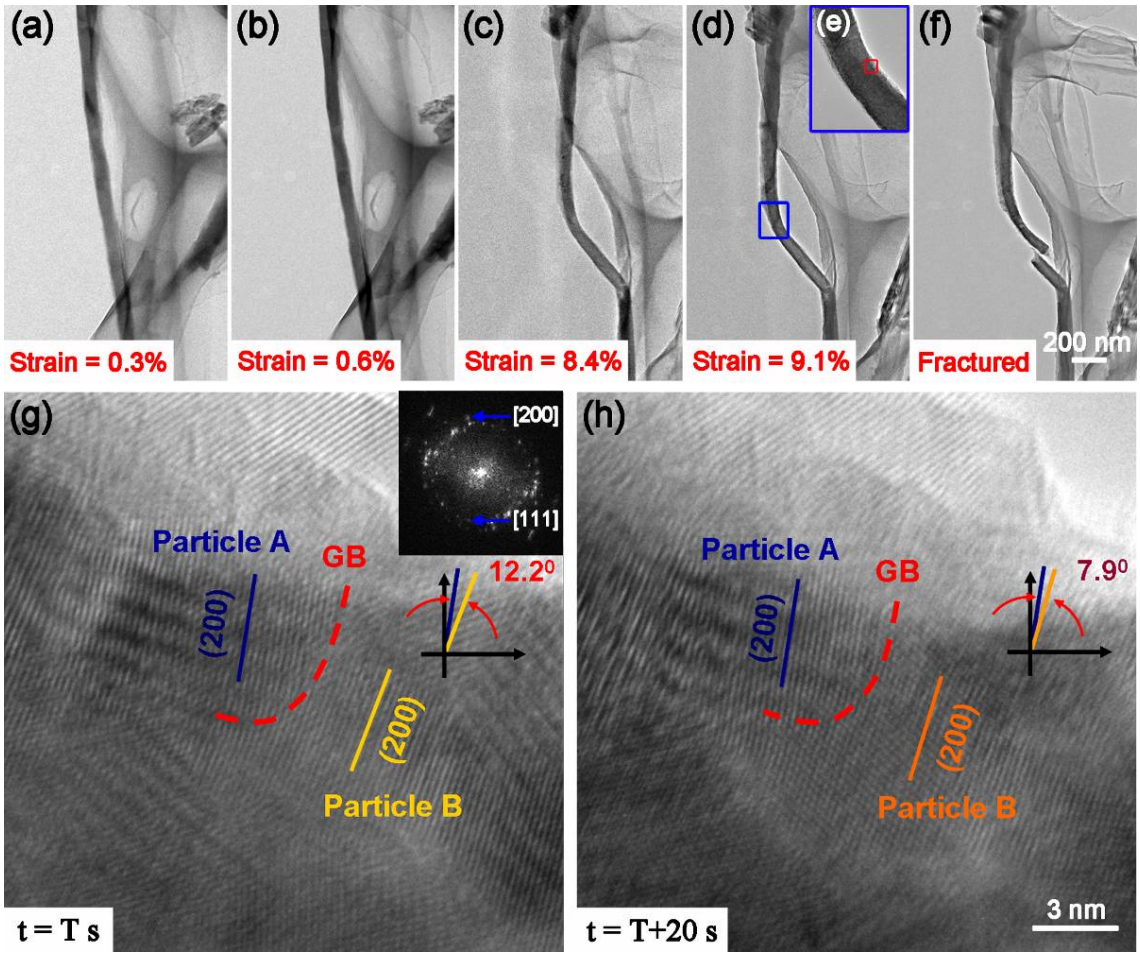

Figure 3.3. *In situ* TEM observation of a third-order lamella upon bending. (a - f) Time-lapsed images captured at the bending strain of 0.3%, 0.6%, 8.4%, 9.1% and fracture in order to show the plastic bending process. (g) HRTEM image of the selected area in (e) with a spotty-like diffraction pattern inserted. (h) With extra 20 s irradiation on the same region, the orientation of nanoparticles is altered, suggesting the effect of radiation on modifying the atomic structure.

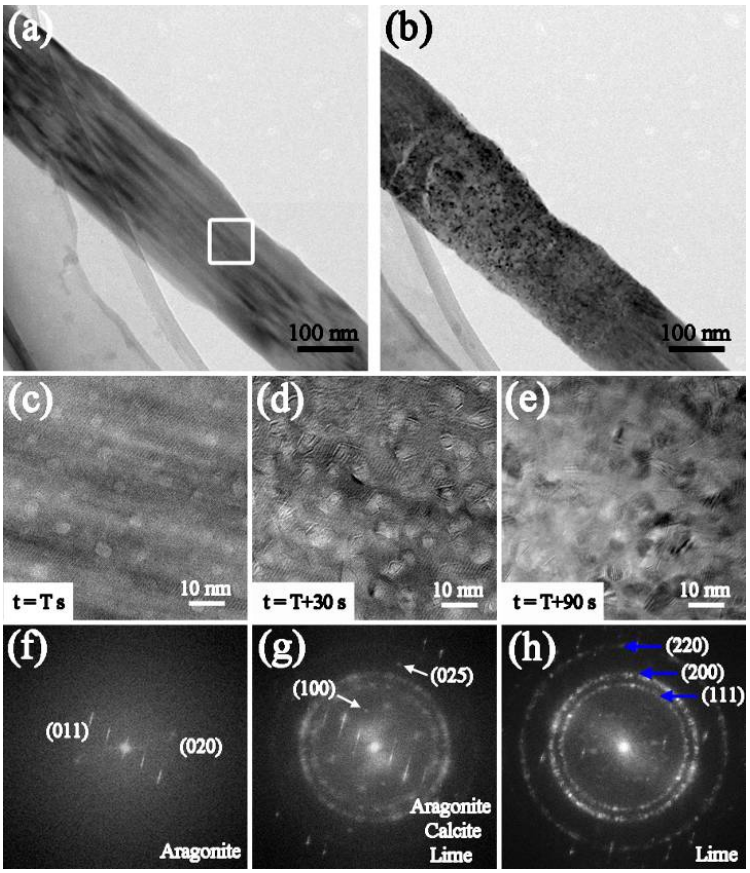

Figure 3.4. Phase transformation under *in situ* irradiation. (a) and (b) TEM images of an individual third-order lamella pre- and post-radiation, respectively. (c - e) Sequential HRTEM images from boxed area of (a) retrieved at the time of T s, T+30 s and T+90 s. Here, T < 60 s for the original focus. (f - h) Corresponding diffraction patterns of (c - e), starting from single crystal characteristic pattern to spotty and continuous Debye rings. Phase transition from aragonite to calcite and finally to lime is, accordingly, derived.

Figures 3.4a and b display the structural evolution of a third-order lamella from smooth profile to mottled surface under e-beam irradiation. Within 90 s radiation interval, nanoparticles were steadily driven to rotate (Figures 3.4c - e). Although nanoparticles have been verified as the basic building units for lamellae, analysis upon series of

diffraction patterns (Figures 3.4f - h) from corresponding Figures 3.4c - e suggests otherwise. Initially, the single-crystal diffraction pattern identified as aragonite is displayed in Figure 3.4f. Under additional 30 s illumination (Figure 3.4g), the formation of calcite (another variety of calcium carbonate confirmed by white arrows) and lime (CaO, which is characterized as polycrystalline rings) indicate the phase transformation under e-beam radiation. Finally, both kinds of $CaCO_3$ were decomposed into lime due to the remaining continuous polycrystalline rings (Figure 3.4h). As a result, the irradiation-induced phase transformation (aragonite - calcite - lime) is proposed. Herein, EELS was employed to quantitatively evaluate the variation of elements content under radiation.

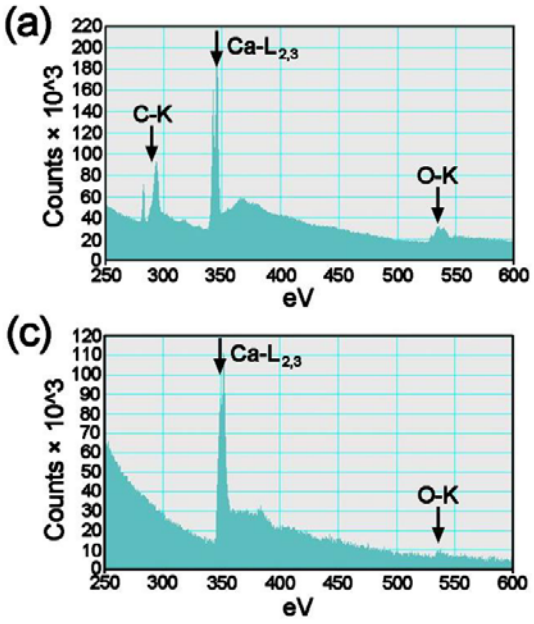

(b)

Element	Atomic ratio(/O)	Percent content
C	0.35	20.51
Ca	0.35	20.63
O	1.00	58.86

(d)

Element	Atomic ratio(/Ca)	Percent content
C	0.04	2.45
Ca	1.00	55.41
O	0.76	42.15

Figure 3.5. EELS analyses on the effect of irradiation. (a) Pre-irradiation EELS spectrum. (b) Calculated atomic ratios and their percent contents from (a). (c) and (d) EELS spectrum and calculated contents after radiation, respectively. The comparison between above tables demonstrates the phase decomposition from calcium carbonate to calcium oxide.

Figures 3.5a and b display the EELS analyses with the spectrum and calculated element contents of a single third-order lamella, respectively. The listed values are consistent with the composition of $CaCO_3$. It should first point out that the existence of carbon film might influence the analyzed results. However, judging by the trend of changed magnitudes upon irradiation (Figures 3.5c and d), $CaCO_3$ was obviously decomposed into CaO when subjected to e-beam illumination. Coupling the observation from Figure 3.4, the suggested phase transformation (aragonite - calcite - lime) induced by irradiation is verified. Therefore, the improved plasticity in TEM bending (Figure 3.3) is not only the credit of aragonite, but the contribution from the other two kinds of ceramics.

How does phase transition happen? Thermal effect is generally related to the issue. Temperatures for aragonite - calcite and calcite - lime transformations are at around 400 °C and 800 °C, respectively.[91,92] Can e-beam illumination heat materials to these fever levels? Quantitative calculation for evaluating highest temperature by electron beam heating is listed in the following equation:[93,94]

$$T = \frac{W}{4\pi l_0 k_0}(1 + 2\ln\frac{R_0}{r_0}) \qquad 3.4$$

where l_0 is the thickness of sample (here, 100 nm), k_0 is the thermal conductivity (here, 5 W/(m K)), R_0 represents the radius of hole in supporting film (here, 10^{-3} m), and radius of irradiated region is signified by r_0 (here, 100 nm). W is the total absorbed power, and can be calculated as:

$$W = \varepsilon_0 V \rho_0 \pi r_0^2 \quad 3.5$$

here, ε_0 represents proportional absorbed energy (here, 0.01), V is acceleration voltage (here, 200 keV), ρ_0 denotes the current intensity (here, 13.5 A/cm^2). Based on the experimental results of this work, the calculated maximum temperature elevation, 26 K, within focused area nullifies the heat effect prospection. Associated with high-thermal-conductivity supporting film, such heating factor is further proved to be incompetent in guiding phase transformation. Alternatively, we consider the impact effect of electron particles.

Depending on the transferred energy from striking charged particles to the target materials, two primary mechanisms of irradiation damage can be triggered by the electron beam.[95,96] Under the sufficient energy, initiation of knock-on damage produces direct displacement of atoms from the crystal lattice. Otherwise, lattice rearrangement caused by chemical bonds' breakage, known as radiolysis, is ascribed to the lower transferred value. Here, the maximum transferred energy (E_{max}) from incident electrons with a certain kinetic energy (E_0) to the targeted atom (atomic mass as A) is calculated with the following equation:[97]

$$E_{\max} = E_0\left(1.02 + \frac{E_o}{10^6}\right) \Big/ (465.7 \times A) \quad 3.6$$

Accordingly, the peak transferred values from electron beam to the atoms Ca, C and O are calculated as 13 eV, 44 eV and 32 eV, respectively, under the condition of 200 kV. Despite the absence of direct research on atomic displacement energy threshold of

calcium carbonates, relative studies[98-100] reveal that radiolysis is quite possible to be the dominant factor for phase transformation because of the obtained low energies. Nevertheless, we do not completely exclude the probability of knock-on damage. In CaO, the much higher displacement energies for Ca and O atoms (~ 50 eV) render knock-on damage and radiolysis impossible, forming the final stable phase. Then, another question pumps out: How is the phase transformation crystallographically achieved? Here, the short-range diffusion induced phase transformation by electron beam is reported, which consumes the least energy and is regarded as the major mechanism.

Classified as ceramics, aragonite, calcite and lime are characterized as different crystal structures in orthorhombic, trigonal and face-centered cubic systems, separately. Due to the identical composition between aragonite and calcite, the phase transition can be essentially achieved in reshuffling calcium and carbonate ions based on original aragonite lattice arrangement. Figure 3.6a displays the tracks of ions movement in aragonite, to be specific, anion groups in neighboring layers are separately rotated at 30^0 (observed from $[00\bar{1}]$ direction) clockwise and anticlockwise with occupying the positions half way between two calcium ions from adjacent layers. Meantime, calcium ions are shifted within a very short distance in the direction of $[010]$ (and $[0\bar{1}0]$).[32] Via small distortive deformation afterwards for lattice accommodation because of the lattice dissimilarities between two calcium carbonates, the transformation process from aragonite to calcite is finally accomplished (Figure 3.6b).

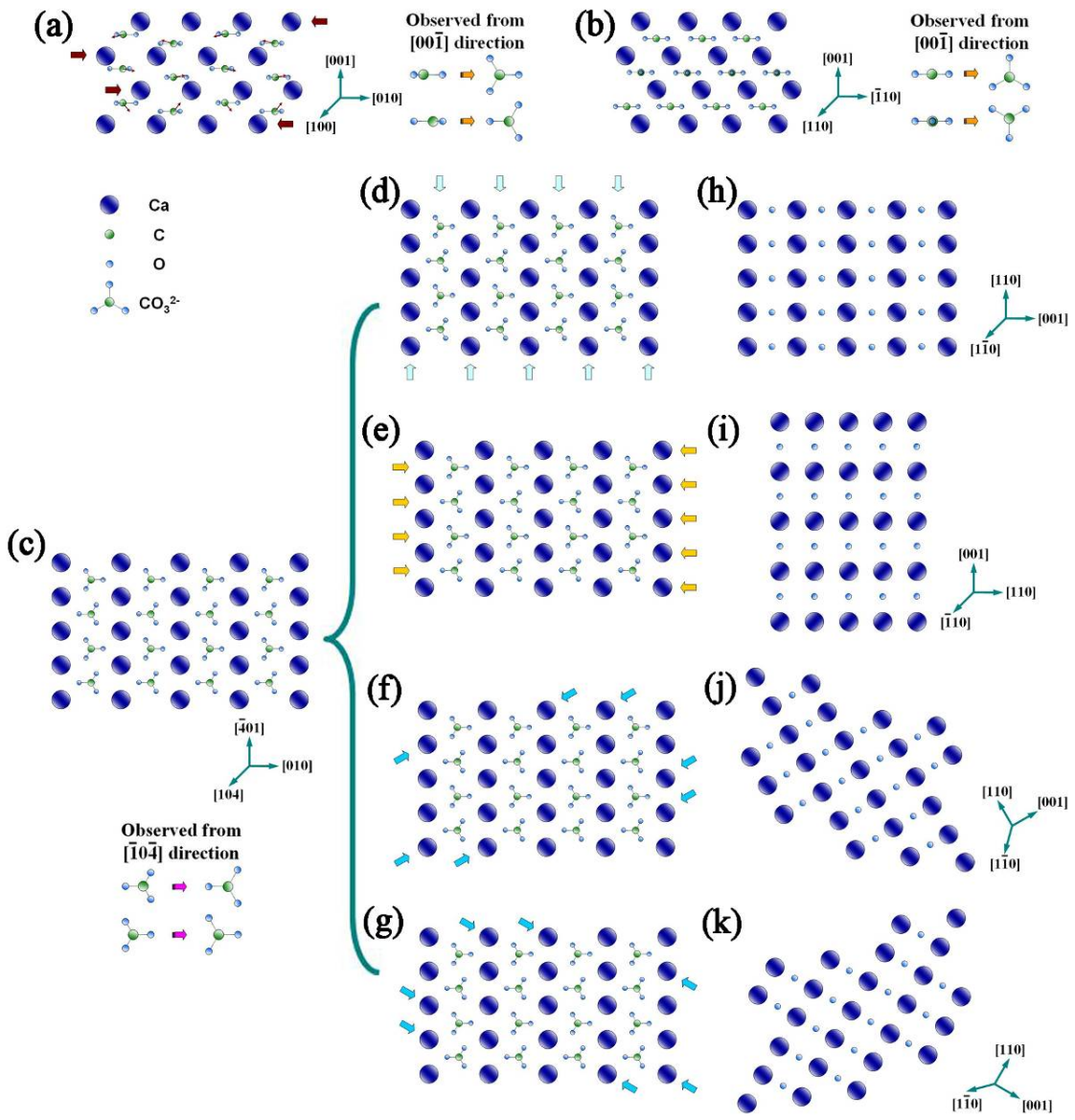

Figure 3.6. Sketches of lattice evolution during phase transformation. (a) Aragonite lattice observing from [100] direction. (b) Lattice arrangement of calcite from [110] direction. (c) Calcite crystal lattice in [104] inspection. (d - g) Four sorts of orientations and ionic adjustments in calcite that lead to the formation of lime. (h - k) Corresponding stable structures of lime evolving from (d - g).

Similarly, the short-range movement upon transformation (calcite - lime) depends on the lattice arrangement of calcite but resorts to several solutions.[91,92] As illustrated in

Figure 3.6c, the trigonal structure (aligned in $(10\bar{4})$ plane) of calcite is altered to face-centered cubic organization (lime) by slightly moving ions in the direction of $[\bar{4}01]$ (and $[40\bar{1}]$), substituting planes of O^{2-} for CO_3^{2-} upon CO_2 escaping, as well as the occurrence of small lattice-distortive deformation to adjust the new-formed lattice variation (Figures 3.6d and h). Additionally, such decomposition can be realized in the parallel approach via shuffling along $[010]$ (and $[0\bar{1}0]$), $[\bar{4}41]$ (and $[4\bar{4}\bar{1}]$) and $[48\bar{1}]$ (and $[\bar{4}\bar{8}1]$), respectively (Figures 3.6e - g, i - k).

However, this critical question in e-beam promoting the plasticity of bioceramics remains unsettled. It should first point out that the lower-rate TEM deformation contributes to such improvement. More importantly, the cleavage of chemical bonds (radiolysis) and resulting creation of vacancies induced by electron beam irradiation increase ions migration and rotation, facilitating the bond-switching process which repairs the new triggered voids upon deformation. Such self-promoted accommodation to stress flow accompanied by the assistance of biopolymer's viscosity and nascent nanoparticle refinement realize the metal-like performance upon e-beam radiation.

3.3 SUMMARY

In summary, we demonstrate direct evidence that the ceramic-based third-order lamellae, which are the building blocks in conch shells, exhibit not only elasticity but also plasticity, overturning the general assumption of brittleness. The nanoparticle-biopolymer construction of third-order lamellae contributes to this metal-like behavior with the mediation of biopolymer in assisting nanoparticle rotation. In addition, the plasticity of

bioceramics is improved by the electron-beam induced phase transformation (aragonite - calcite - lime). These findings deepen our understanding of the toughening strategy of conch shells and may open up new avenues for developing bioinspired materials and sensors.

CHAPTER 4

DYNAMICAL SELF-STIFFENING PROTECTION IN CONCH SHELLS

Creatures have been incubating countless skills for survival (i.e., predation and self-protection). Conch shells, as called as nature's armors, protect the soft bodies from predatory attacks (such as turtles, crabs, fish, and seabirds).[101,102] Harassed by daily ballistic attacks, what roles does multiscale organization play in the shielding of soft bodies? Could such shells initiate alternative mechanisms as a response in comparison with those executed upon quasi-static conditions? Can we blend their fracture behaviors into man-made bio-inspired[103] composites? Addressing these questions needs our in-depth investigation in bridging relationship between materials' structure and performance under different strain rate situations.

Accordingly, a series of uniaxial compression tests under quasi-static and dynamical loading rates were designated for the aforementioned scenarios. We utilized the universal testing machine to perform quasi-static compression (10^{-4} ~ 10^{-2} /s), and Split Hopkinson Pressure Bar System to realize high strain loading rates (~ 10^{3} /s). The elevated fracture strength and damage tolerance under dynamic loading stands in stark contrast to the quasi-static counterparts. A new-finding deformation behavior,

intra-lamella fracture (involving nanoparticle rotation as well as formation of trapped dislocations), is ascribed to create the high-strain-rate eminence. Occurrence of such fracture is associated with the small activation volumes for plastic deformation of shells. Favored as the source of inspirations, Mother Nature's pre-design in structural arrangement provides guidelines for biomimetic engineered materials.

4.1 EXPREIMENTAL

Specimens for compression tests were first sectioned by water-cooled, low-speed diamond saw, then ground and polished, and finally rinsed with distilled water thoroughly prior to testing. Quasi-static and dynamic loading uniaixal compression tests were realized by Instron 5566 Universal Testing Machine and Kolsky (Split Hopkinson) Pressure Bar System, respectively. Post-mortem fragments were gold-coated with a 10 nm thick gold-film before the fractography observation with field emission scanning electron microscope.

High resolution transmission electron microscopy (HRTEM) (H-9500 TEM, Hitachi Inc., Dallas, TX) was employed on gathered post-mortem powders, which were first ultrasonically dispersed in distilled water for 10 min and transferred onto the holey carbon-coated copper film, at an accelerating voltage of 300 kV.

4.2 RESULTS AND DISCUSSION

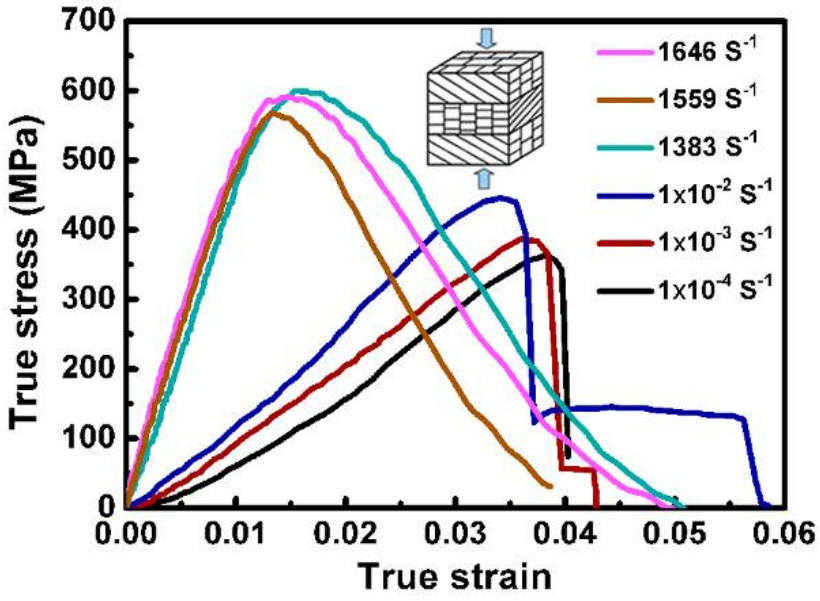

Figure 4.1. Compressive true stress-strain curves in quasi-static and dynamic loading conditions. The fracture stress gradually increases from ~ 360 MPa (10^{-4} /s) to ~ 450 MPa (10^{-2} /s) in quasi-static loading range, and jumps to ~ 600 MPa under dynamic loading rates (~ 10^{3} /s), with true strain displaying the opposite trend.

From true stress-strain curves (Figure 4.1), the fracture stress crescendos from ~ 360 MPa to ~ 450 MPa accompanied by the increment of quasi-static strain rate (10^{-4} /s - 10^{-2} /s). Surprisingly, the achieved dynamic fracture strength (600 MPa at the rate of ~ 10^{3} /s) forms a sharp contrast with former performance. Such striking augment evidently suggests the strain-rate dependence of conch armors' mechanical feedback. Therefore, 'dynamical self-strengthening' behavior is proposed to mirror shells' output under dynamic impacts. To characterize and quantitatively evaluate this self-improved property, strain rate sensitivity (SRS) is introduced and calculated as followed:[104,105]

$$m = \frac{\partial \ln \sigma}{\partial \ln \dot{\varepsilon}} \tag{4.1}$$

where m is SRS, σ and $\dot{\varepsilon}$ are applied stress and strain, respectively. By integrating Equation 4.1, the SRS is also treated as[104]

$$\sigma = K\dot{\varepsilon}^{m} \tag{4.2}$$

Consequently,

$$\ln \sigma = \ln K + m \ln \dot{\varepsilon} \tag{4.3}$$

Upon two dissimilar loading rates, the acquiring sets of data $(\sigma_1, \dot{\varepsilon}_1)$ and $(\sigma_2, \dot{\varepsilon}_2)$ will be represented on the basis of Equation 4.3:

$$\ln \sigma_1 = \ln K + m \ln \dot{\varepsilon}_1 \tag{4.4}$$

$$\ln \sigma_2 = \ln K + m \ln \dot{\varepsilon}_2 \tag{4.5}$$

Accordingly, the SRS is obtained by derivation of Equations 4.4 and 4.5,

$$m = \ln \frac{\sigma_1}{\sigma_2} \Big/ \ln \frac{\dot{\varepsilon}_1}{\dot{\varepsilon}_2} \tag{4.6}$$

Through compression results in Figure 4.1, we are able to calculate the range of m. The finding minimum value corresponds to the condition:

$$\sigma_1 = 567MPa, \quad \dot{\varepsilon}_1 = 1559s^{-1};$$

$$\sigma_2 = 446MPa, \quad \dot{\varepsilon}_2 = 0.01s^{-1}$$

Therefore,

$$m_{\min} = \ln \frac{567}{446} \Big/ \ln \frac{1559}{0.01} = 0.0201$$

To find the maximum, the values are used under such conditions:

$$\sigma_1 = 600MPa\,,\quad \dot{\varepsilon}_1 = 1383s^{-1};$$

$$\sigma_2 = 387MPa\,,\quad \dot{\varepsilon}_2 = 0.001s^{-1}$$

Thus,

$$m_{\min} = \ln\frac{600}{387} \Big/ \ln\frac{1383}{0.001} = 0.0307$$

To sum up, SRS is in the range of 0.020 ~ 0.031.

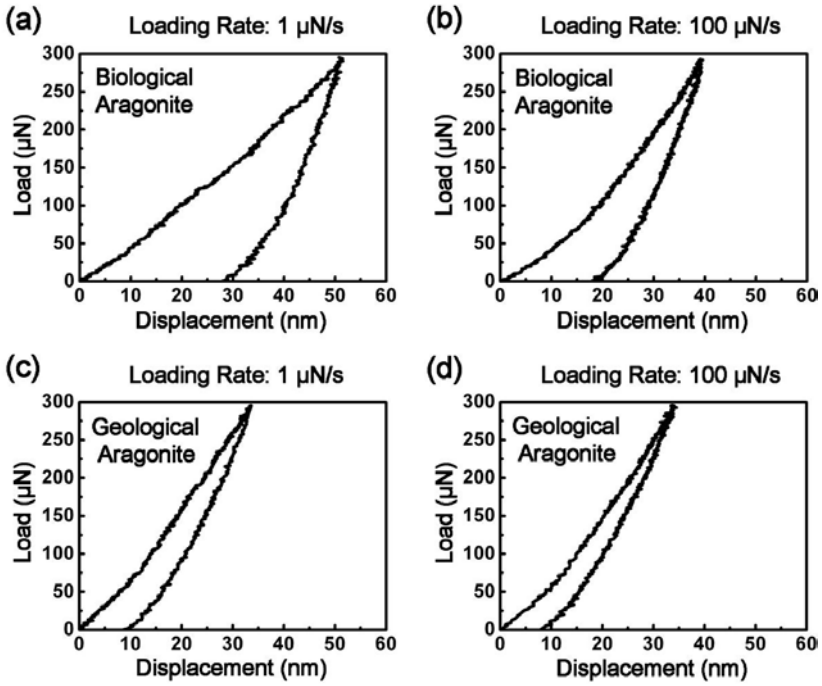

Figure 4.2. Comparison in rate-dependence property between biological aragonite (conch shell) and geological aragonite. Nanoindentation load-displacement curves of the conch shell (a, b) and pure aragonite (c, d) under two different loading violations, indicating the rate insensitivity of geological aragonite.

The derived value is surprisingly close to that in metals (nano-Al[106] and nano-Cu[107]) with the same grain size. Instead of the findings of rate insensitivity (Figure

4.2) or negative SRS value in ceramic materials, our rate-dependence bioceramics require thorough elaboration. Hereby, a couple of questions need to answer: What are the deformation mechanisms upon different strain rates? What are the origins of so-called dynamical self-strengthening in conch shells?

Figure 4.3 displays a cracked conch sample with meandering strips in between after quasi-static compression. Its fracture details are schematically described in Figures 4.3b-d from micro- down to nanoscale, correspondingly. Impeded at the microlayer junction (as discerned by difference of third-order lamellae orientation in Figure 4.3h), the rupture activities were confined within middle layer without penetrating into others. The exhibited curved first-order lamellae (Figures 4.3a and b) are indeed misguided by copious separated second-order lamellae (as indicated with red box in Figure 4.3f). In addition, the cracks were bidirectional-cleaved in a zigzag manner along third-order interfaces inside second- and first-order units (as indicated by black and red arrows in Figure 4.3j). These aforementioned activities multiply the crack propagation and play a critical role in retarding failure, greatly contributing to the high toughness of bioceramics.

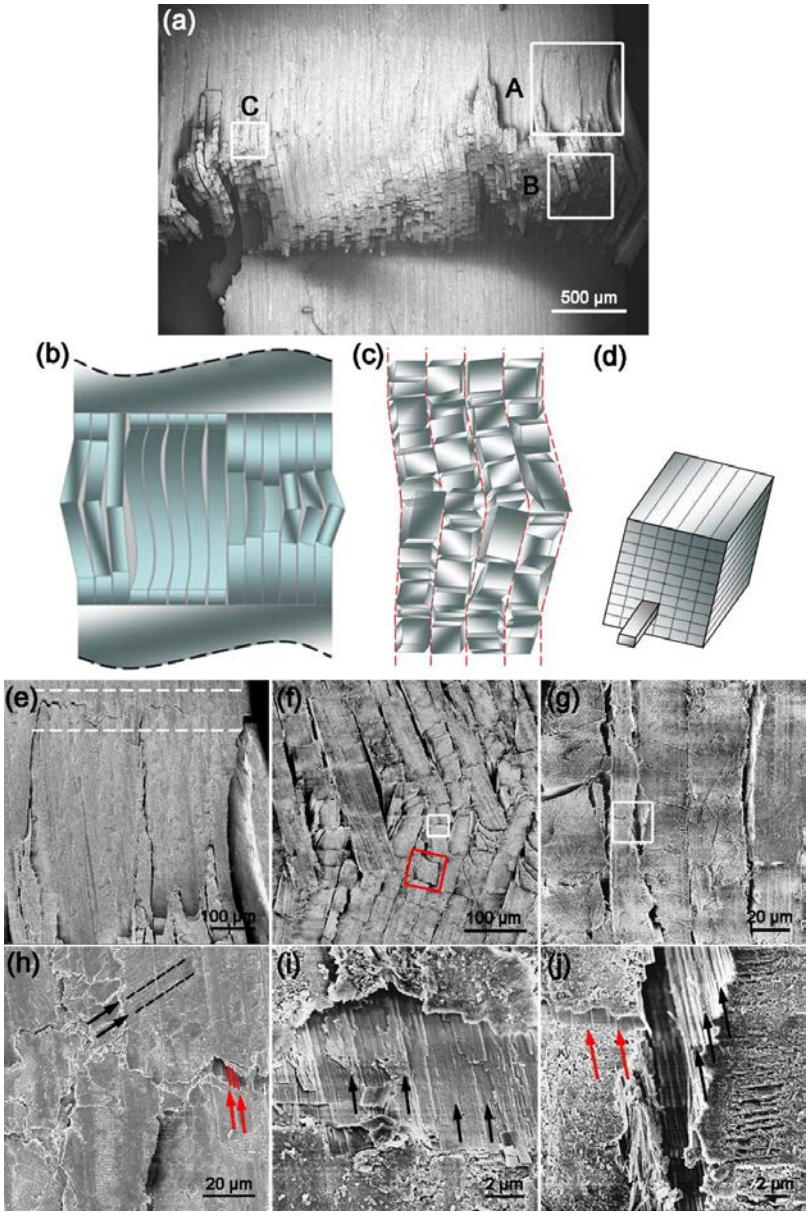

Figure 4.3. Fractured morphology of a specimen after quasi-static compression. (a) Overview of the sample. (b - d) Sketches of breakage details from first-order downscale to third-order lamellae, respectively. The curved first-order lamellae are comprised of detached second-order lamellae. (e - g) SEM images of boxed areas A, B and C in (a), separately. Lamellar interfaces of the first-, second- and third-order are primarily adoptable paths for cracks. (h - j) Corresponding closer-up views of selective areas in (e - g). Confined in the middle layer (h), the cracks are terminated at the microlayer boundary.

One question is, accordingly, raised: How can body armors realize this innovative solution? Due to the large discrepancy in mechanical stiffness between aragonite lamellae and biopolymer interfaces, the soft binder primarily offers weak positions to be broken through. Consequently, detaching and cleaving along lamellar bio-interfaces release stress concentration, resulting in visual illusion of plastic deformation of first-order lamellae. The instability of first-order lamellae by their exceeded height in comparison with the other layers contributes to fracture in the middle layer. The sophisticatedly altered lamellar orientation, additionally, restricts these cracking behaviors in one layer. With practical significance, such deformed strategy inhibits the mollusks from being pierced by fissured inner layer, and attacked by predators when spotting outer layer crevices.

After examination of the dynamically compressed specimen (Figure 4.4a), the presented a large preponderance of nanorod-shape third-order lamellae in lieu of quasi-static intactness (Figure 4.4b) insinuates the disparate responses at variable strain rates. The interface-dominate fracture (Figure 4.3) is obviously no longer the only deformation behavior in dynamic situations; lamellae breakage is triggered as well. As displayed in Figure 4.4c, the statistical distribution shows that the lengthy third-order lamellae with original hundreds of micrometers were pulverized into rods in the range of 0.4 μm and 2.5 μm. Herein, we propose a catastrophically dynamic fracture model.

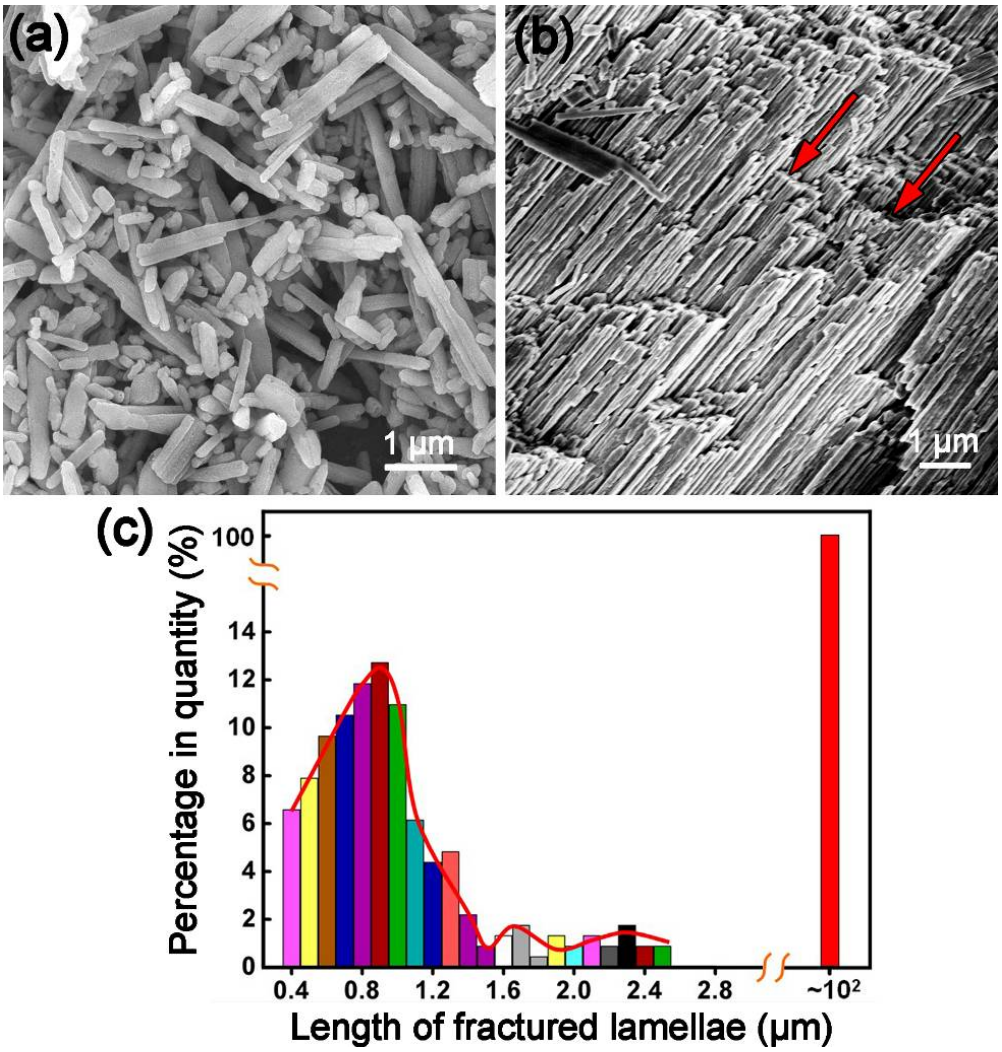

Figure 4.4. Comparison in completeness of third-order lamellae after dynamic and quasi-static loading compression. (a) Multi-fragmented third-order lamellae upon impact. (b) Fractured surface with intact third-order lamellae under quasi-static condition. (c) Length distribution of third-order lamellae in above two cases. The left bunch of columns (dynamic) differs from single red bar (quasi-static) on right side, implying dissimilar fracture behaviors.

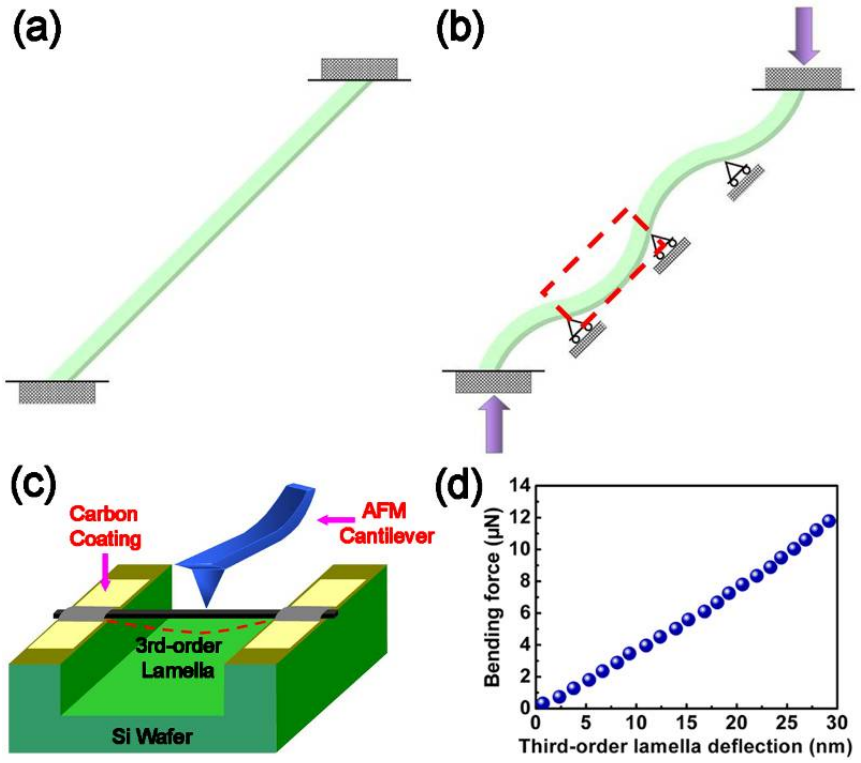

Figure 4.5. Fracture model of a third-order lamella under dynamic loading and mechanical characterization of one fractured part. (a) Sketch of a third-order lamella simulating its position inside shell before deformation. (b) Dynamic multi-fracture model. The direction of external force is identical to the real condition of compression tests. Formation of supports originates from the surface roughness of lamellae and biopolymer's non-uniform thickness. (c) Schematic diagram of three-point bending on a single third-order lamella to characterize the bended behavior of each segment in (b). (d) A representative force-deflection curve from bending.

The original condition of a third-order lamella inside shell, as oriented at ~ 45^0 to the surface, is displayed in Figure 4.5a. As the ballistic force approaches vertically, numerous fulcrums are formed because of the nanoasperity of lamellae, uneven biopolymer thickness together with inhomogeneous stress distribution. Followed by

bending and detaching from each other (Figure 4.5b), such multi-fragment fracture is achieved by the high aspect ratio of third-order lamellae as well as weak biopolymer interfaces. Concerning the mechanical performance of each partitioned segment (boxed area in Figure 4.5b), we introduced three-point bending, which is schematically illustrated in Figure 4.5c, as a reference. Next, the proposed model is verified from the standpoint of energy consumption.

It should first point out that some unexpected but trivial factors might be activated under low strain rates because of shells' complex hierarchical structure; herein, the lamellar interface splitting is simplified as the only governing mechanism. Alternatively, dynamic fracture behaviors consist of both lamellar separation and breakage. We selected two specimens deformed at strain rates of 1×10^{-4} /s and 1383 /s (Figure 4.1) for study, their corresponding energy consumptions in compression are 0.262 J and 0.754 J. This derived energy gap is attributed to lamellae self-breakage. Associated with referenced fracture energy (1.6×10^{-13} J) of a third-order lamella (Figures 4.5c and d), the total fracture times of lamellae in crushed bulk sample can be easily calculated:

$$N = Q/q = 0.754 - 0.262/1.6\times10^{-13} = 0.492/1.6\times10^{-13} \approx 3\times10^{12} \qquad 4.7$$

Considering the original dimension of third-order lamellae (treated as 100 nm × 150 nm × 0.40 mm), there are 6×10^{9} units contained in the pre-deformed bulk. Accordingly, each third-order lamella ends up being snapped into around 500 nanorods with the length of 800 nm ($0.4mm/500 = 800nm$), which is statistically consistent with length distribution in Figure 4.4c. Consequently, our proposed dynamic multi-fracture model elucidates how

bulk materials are shattered to powders in the extremely short time along with their energy utilization.

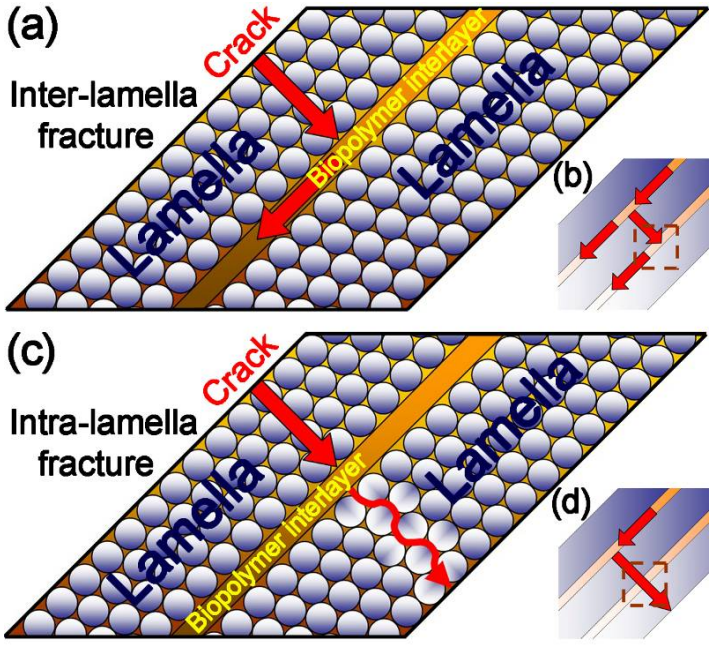

Figure 4.6. Sketches of lamella fracture modes. (a) Inter-lamella fracture, with cracks nucleating and propagating along the biopolymer interlayer. (b) Fracture overview of (a). (c) Cracking through lamellae as called as intra-lamella fracture. (d) Fracture overview from (c), indicating the fissuring propensity.

From the above analysis, the quasi-static failure is principally governed by inter-lamella fracture (Figures 4.6a and b), while coupled inter- and intra-lamella fractures direct the dynamic crack trajectory (Figures 4.6c and d). Given these, why there exists a crossover between inter- and intra-lamella fractures? As a matter of fact, the dominant behavior relies on the critical condition of energy release rate as the expression listed:[108,109]

$$G_{Inter} \diagup G_{Intra} = \Gamma_P \diagup \Gamma_L \qquad 4.8$$

where G_{Inter}, G_{Intra} are energy release rates of the inter-lamella crack tip and intra-lamella crack tip, respectively; Γ_L, Γ_P denote the fracture toughness of third-order lamella and biopolymer. Although to our knowledge the required toughness values remain unexplored, we can relate Dundurs' parameter to this ratio:[110]

$$\alpha = (E_L - E_P) \diagup (E_L + E_P) \qquad 4.9$$

where E_L, E_P represent the elastic moduli of third-order lamella and biopolymer, correspondingly. Here, E_L (= 96 GPa) is obtained in our three-point bending (Figures 4.4c and d), and biopolymer property[111] is treated as E_P = 4 GPa; therefore, the critical ratio (G_{Inter}/G_{Intra}) [110] under quasi-static rates is measured as ~ 1.50 on the basis of α (0.92) from previous study. Meanwhile, upon dynamic parameters, we suggest the amplified toughness of lamella as 150% (based on the rate-sensitive performance in Figure 4.1), and biopolymer[112] in 20%. The changed ratio G_{Inter}/G_{Intra} (0.72) apparently indicates the transition of dominant behavior from inter-lamella to intra-lamella damage as the increment of strain rate. As a result, the dynamically activated inter- and intra-lamella fractures improve the mechanical performance of conch shells in comparison with that of low-rate scenarios which are characterized as the sole effective factor (inter-lamella fracture).

Yet another question may follow: Is there any nanoscale structural modification triggered by deformation? Direct HRTEM investigation was applied to shed light on the atomic level of post-mortem samples.

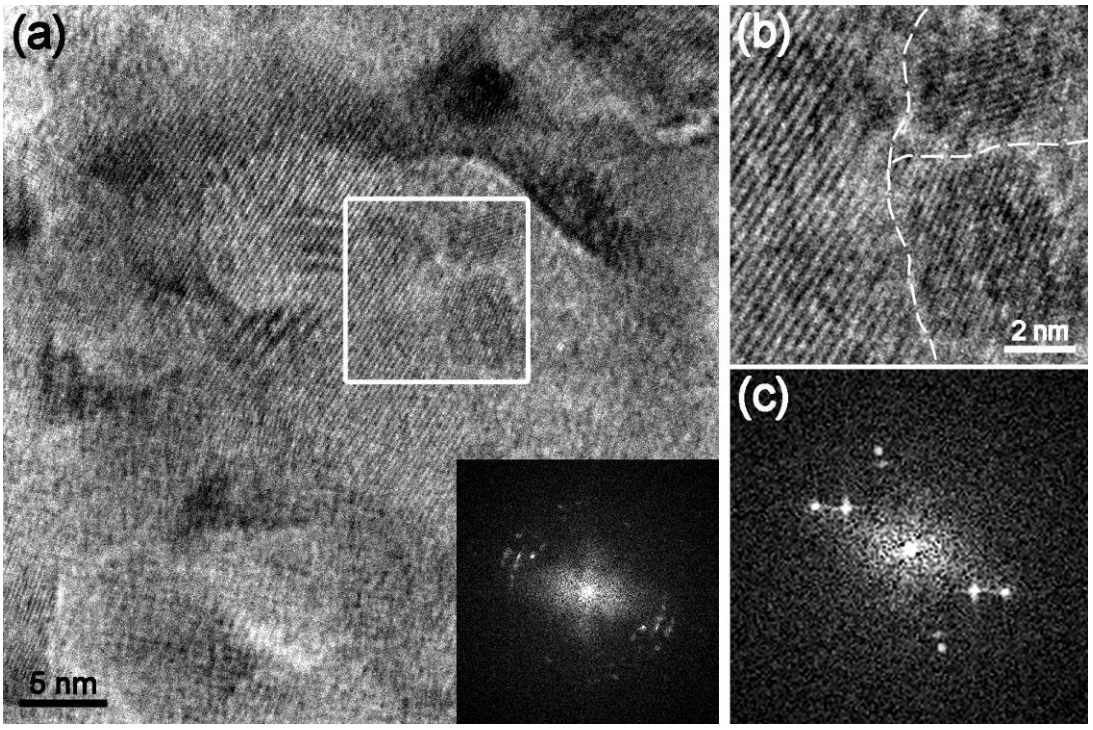

Figure 4.7. Disordered orientations of nanoparticles inside a dynamically compressed third-order lamella. (a) Disorganized nanoparticles with polycrystalline electron diffraction pattern inserted at the bottom. (b) Enlargement of boxed area from (a) displays three nanoparticles with dissimilar orientations, which are delineated by lines. (c) Electron diffraction pattern of (b).

Opposing to the invariable atomic structure of lamellae after quasi-static compression, HRTEM image in Figure 4.7a displays nanoparticles with random crystallographic arrangement under dynamic loading. The close-up view of boxed area (Figure 4.7b) exhibits three particles (delineated by white lines) with size of several nanometers. Non-preferential orientations are provoked amid these nanoparticles, as further supported by diffraction pattern (Figure 4.7c). Such observation indicates that nanoparticles rotation was initiated during dynamic compression. This grain-boundary accommodation may effectively obstacle dislocation activities and thus plays an

important role in increasing fracture strength. Similar deformation mechanisms have been extensively studied in nanocrystalline materials studies.[113,114]

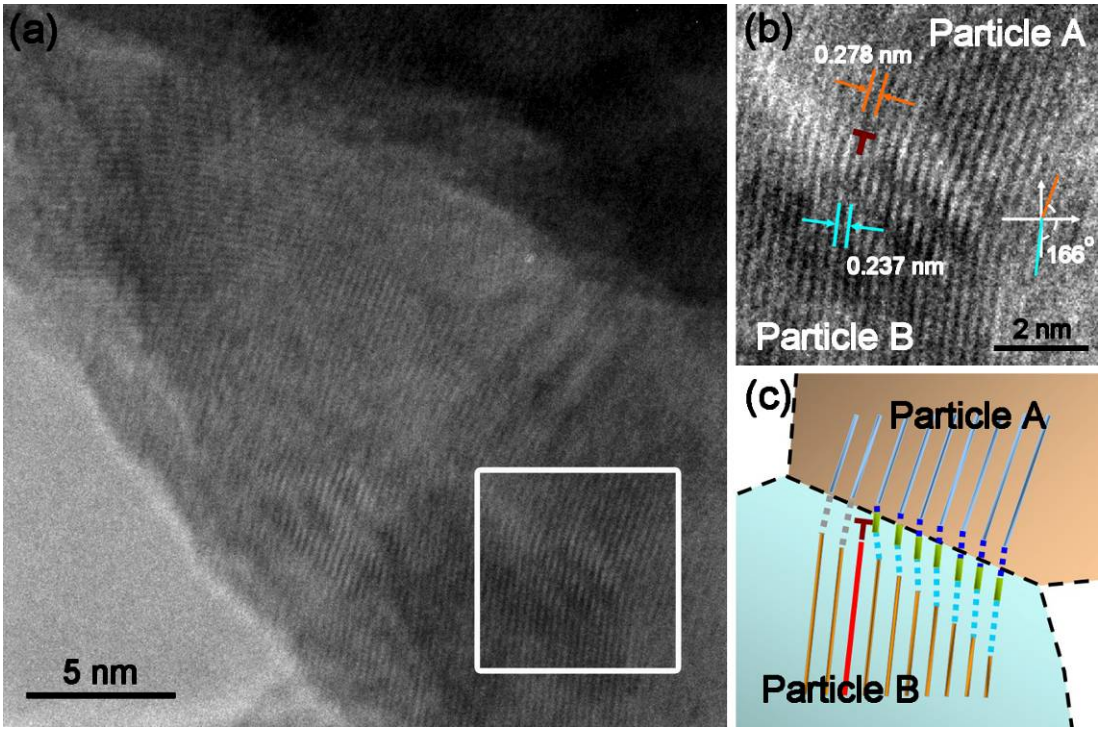

Figure 4.8. Analysis of an edge dislocation in the dynamically deformed third-order lamella. (a) The bending lattice arrangement in boxed area evidences the mutual movement between particles. (b) Detailed lattice distortion with the tilt angle at 14^0 between two particles. An edge dislocation is found to be trapped inside of a particle, leading to slight change of interplanar spacing. (c) Sketch of the lattice arrangement in clarifying the edge dislocation.

Besides the findings aforementioned, an edge dislocation is spotted via scrutinizing the lattice arrangement (Figure 4.8a). Instead of anticipation as located at the grain boundary (because of high-ratio atoms[115,116] around boundary), a close-up inspection on dislocation sequences surprisingly reveals the lattice irregularities within the nanoparticle (Figure 4.8b). Moreover, interplanar spacing inconsistencies (0.237 nm

and 0.278 nm), as the consequence of dislocation activity, are identified after line-by-line measurement. Depicted in Figure 4.8c, we schematically illustrate how the trapped dislocation is clarified in judging lattice orientation as well as interplanar spacing magnitude. Initiated by mutually rotated Particles A and B at an angle of 14^0, the edge dislocation is terminated inside B rather than traditionally emitted from one grain boundary and sunk at the other side. Our observation proves the intra-granular deformation is activated upon dynamic loading as well.

How does the dislocation "kick in"? In this regard, the activation volume (v*) in quantitatively describing plastic domain is connected with strain rate sensitivity for elucidation:[105]

$$v^* = \frac{\sqrt{3}k_c T_0}{\sigma \cdot m} \tag{4.10}$$

where Boltzmann constant (1.38×10^{-23} m^2kg/s^2k) is denoted by k_c, T_0 is absolute temperature, σ and m are effective stress and strain rate sensitivity, respectively. From the experimental results in this work, the calculated activation volume is:

$$v^* = \sqrt{3}\times1.38\times10^{-23}\times293 \Big/ 600\times0.03 \approx 0.39nm^3 \approx 20b^3$$

here, | b | = 0.278 nm is identified from Figure 4.8b.

The derived value in the scope of a few b^3 is much smaller than the nanoparticle size, leading to the localized mediation of such interior dislocation. Consequently, upon dynamic loading, the 'tough' mechanism (trapped dislocation) is instigated by local intense stress with small activation volume, while grain boundary accommodation

functions in the easy-going regions. Through inhomogeneous stress distribution, the activated intragranular and intergranular mechanisms[117,118] collaborate to exert significant effects on shells' strengthening under high strain rate aggression.

4.3 SUMMARY

For the first time, a new defense mechanism - intra-lamella fracture, involving nanoparticle rotation and formation of trapped dislocations, is found to activate against high-strain-rate compression in conch shells, which remarkably elevates fracture strength comparing with quasi-static performance. Conch shells' self-promoted fidelity optimizes the protection from dynamic predatory attacks. The origin of mechanical response advances our knowledge in Mother Nature's wisdom and enriches the field in mimicking engineered materials.

CHAPTER 5

MECHANICS GUIDED GEOMETRY IN CONCH SPINES

Over the past decades, seashells, identified as the best natural body armors against predator attacks, have been serving as the inspirations for optimizing man-made composites. Relative studies in mechanical properties of conch shells have been focused on the shell bodies. Few efforts shed light on the conch spines which are evenly distributed at the tail of armor in peculiar appearance and generally accepted as the essential tools[119-123] upon encountering predators. Accordingly, several key questions are raised and need to be answered: What is the microstructure of spines? Is there any difference between body parts and spines? Are spines specialized in protection upon mechanical aggression?

In this letter, three-point bending was performed on the spine for investigating its hierarchical structure as well as fracture behaviors. Surprisingly, the finding curve-shaped reinforcements (third-order lamellae) differ from the straight lamellae in conch bodies. Moreover, via a series of uniaxial compression tests on conch bodies and spines, for the first time, we find that the fracture strength of spines increases up to 30 % in comparison with conch bodies' magnitude, uncovering the protective roles of spines against foreign (mechanical) attacks. Surpassing the 'easy' way adopted by conch shell bodies in sliding

through weak interlayer, spines are characterized as reinforcement's breakage in virtue of curvature. The findings provide detailed information concerning tubercle-like spines, and may open up new avenues[8,124-128] in manufacturing novel high-performance composites with curving reinforcements.

5.1 EXPREIMENTAL

Conch spines were first sectioned by water-cooled, low-speed diamond saw, with clean-up treatment in distilled water afterwards. Bending tests of spines were performed to observe the fractographic features as well as comprehend their deformation behaviors. Single-layer specimens of the conch spines and bodies for compression tests were isolated by diamond saw to the desired dimension, respectively, then ground and polished, and finally rinsed with distilled water thoroughly prior to testing. Quasi-static loading uniaixal compression tests were realized by 810 Material Test System (MTS system Corporation). Post-mortem fragments were collected instantly for further examination. The fractured specimens were gold-coated with a 10 nm thick gold-film before the fractography observation with field emission scanning electron microscope.

Friction tests were carried out on well-polished conch specimens using Micro-Tribometer (UMT-2, Center for Tribology, Inc.) with the tungsten carbide ball at sliding speed of 1.6 mm/s. The friction coefficient can be directly obtained by the tribometer software.

5.2 RESULTS AND DISCUSSION

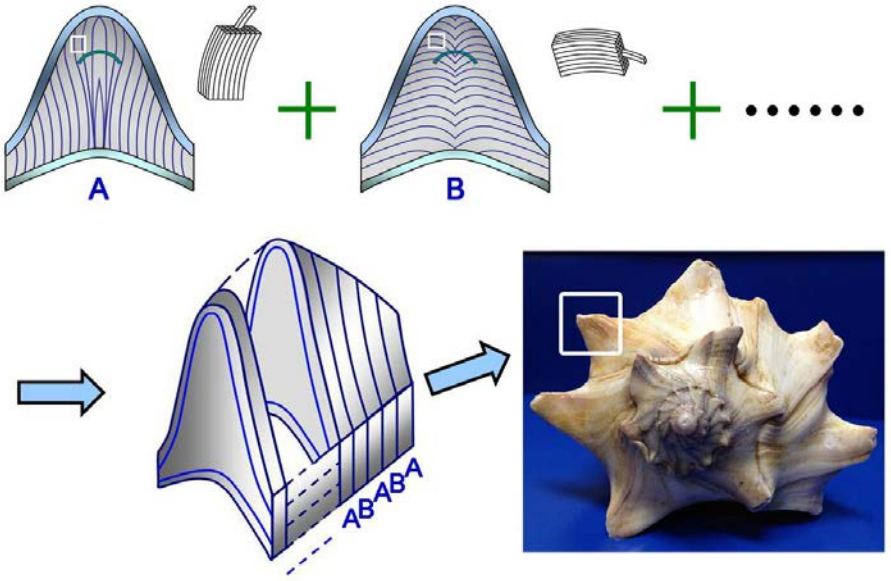

Figure 5.1. Sketches of the hierarchical structure in a spine. Alternating combination of Plates A and B form such protrusion.

Prior to systematically depicting the hierarchical organization of conch spines, we simplify the structure as shown in Figure 5.1. Similar to the body parts, spines are divided into three (outer, middle, inner) layers. Due to the first-order lamellae orientation as $0^0/90^0/0^0$, each plate, classified as Plates A and B, contains a portion of first-order lamellae from outer and inner layers, and the entire first-order lamella of the middle layer. The difference between two sorts of plates is the orientation of third-order lamellae at 90^0 in the middle layer. By overlapping numerous Plates A and B (ABABAB…) horizontally, the spines construction is identified for the first time to our knowledge. Detailed information is listed as followed to characterize its hierarchical structure and fracture behaviors.

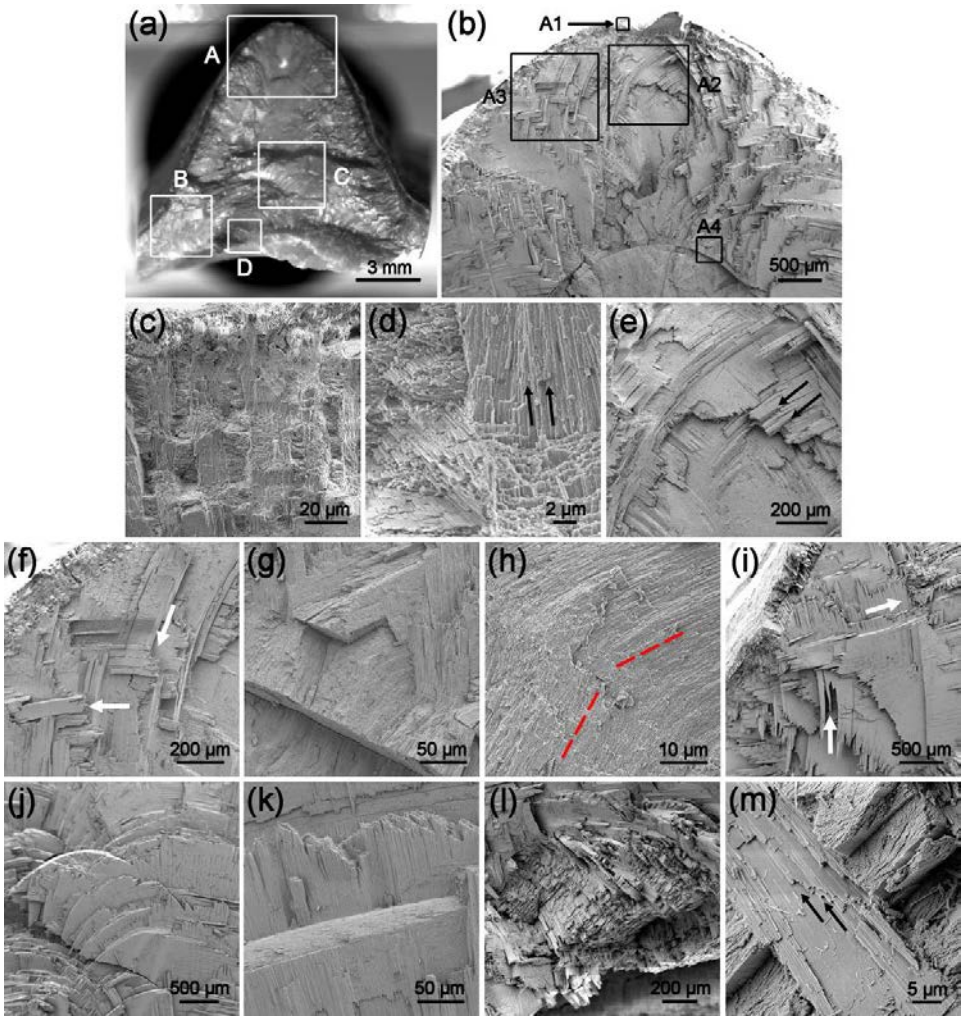

Figure 5.2. SEM images of fractured spine surface. (a) Overview of fractography showing three layers with the middle layer occupying the most volume. (b) Enlarged view of boxed area A from (a). Close-up views of the marked sections A1, A2, A3 and A4 are displayed in (c, d), (e), (f) and (g, h), respectively. Magnification of boxed areas B, C and D of (a) are correspondingly shown in (i), (j, k) and (l, m). Among these, (c) and (d); (e - k); (l) and (m) are images of fractured outer, middle, and inner layers, respectively, at different magnifications. Outer (c) and inner (l) layers have similar lamellar architecture orientation. The curve-shaped third-order lamellae and their orientation diversity at 90^0 between adjacent first-order lamellae are displayed in (b - m). Formation of smooth surfaces (f and i) and step-arranged first-order lamellae (j) shows the preferential choice for crack propagation. In addition, from the edges of first-order lamellae, crack pathways are along and perpendicular to second-order lamellar interfaces (as indicated by white arrows in (f) and (i)).

As shown in Figure 5.2, the spine has the 'plywood' architecture with three layers, termed as outer (Figures 5.2c and d), middle (Figures 5.2e - k) and inner (Figures 5.2l and m) layers, on basis of varied first-order lamellar orientation. Third-order lamellae with nanoscale cross section and micrometer-level length (as indicated by black arrows in Figures 5.2d and m) are bundled to form the strip-shape second-order lamella, as indicated by white arrows in Figure 5.2f. Likewise, stacking of second-order units build up a plate-like first-order lamella (Figure 5.2j). One layer is hereby constructed via overlapping first-order blocks horizontally. The orientation of first-order lamellae in outer (Figure 5.2d) and inner (Figure 5.2m) layers is similar, forming at 90^0 to the arrangement in middle layer (Figure 5.2e). Moreover, third-order lamellar orientation is varied as 90^0 between adjacent first-order lamellae (Figure 5.2k). Generally, the aforementioned hierarchical structure is similar to the conch body; nevertheless, the surprisingly uncovered curving second- and third-order lamellae in spines form a sharp contrast to the linear-shape units in body parts, as well as the outnumbered thickness of middle layer. In Figure 5.2b, a first-order lamella is delicately comprised by two sets of symmetrical curving third-order lamellae, identical to the sketches of Plates A and B (Figure 5.1). The new findings remind us the profile of arch bridge. Famous as the excellent stability by the advantage of intriguing arch layout, such bridges are recorded with over 1400-year history. Unexpectedly, this is the used patent of Mother Nature up to a million years ago.

In Figure 5.2g (Section A4 in Figure 5.2b), we found another interesting phenomenon with a transition layer outlines as a dome. Close-up view (Figure 5.2h)

reveals that the orientation of third-order lamellae is modified by such layer (as indicated by red lines) within the same first-order lamella. Judging by its shape and position inside spine, we propose this transition layer was once the growth tip for young spines. Accompanied by the growth of conch shells, such growth tip could no longer serve as the frontier; therefore, the newborn lamellae overlapped it as a template for further thickness increment. Several theories are dedicated to spine growth,[120,121] and our new finding needs further investigation.

The close-up views of fractured surface (Figures 5.2b - m) reveal that cracks were not only deflected along the lamellar interfaces but also propagated through all three-order lamellae, i.e., first-order (smooth lamellar surfaces in Figures 5.2f, i and step-like first-order lamellar surfaces in Figure 5.2j), second-order (as indicated by white arrows in Figures 5.2f and i), third-order (as indicated by the black arrows in Figures 5.2d, e and m) lamellae separation and breakage.[129,130] Served as integrated shields with frequently-varied lamellar orientations, the three layers (outer, middle, inner) deflect and branch cracks between layers, preventing the plain intrusion from the outer layer directly down to the bottom layer.

The exclusive usage of curving lamellae in spines triggers our curiosity: Why spines struggle to own such hierarchical structure with novelty? Do spines perform better than the straight-component body parts in response to foreign attacks? The compression tests on both materials were, accordingly, carried out.

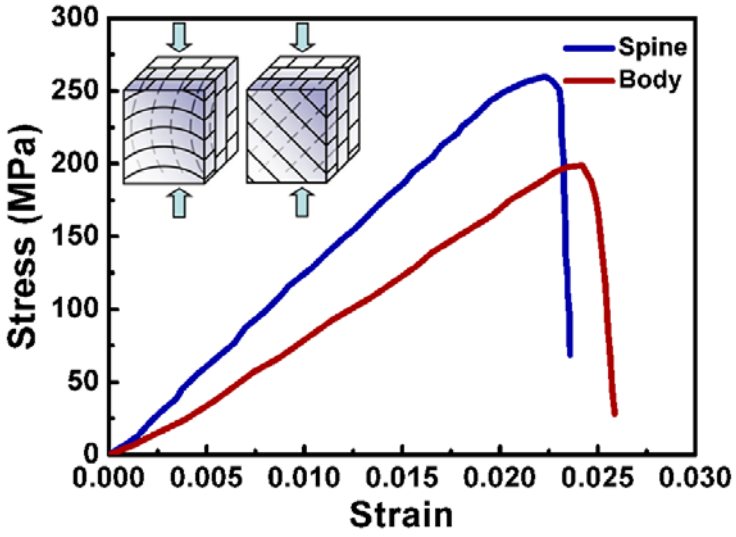

Figure 5.3. Compressive stress-stain curves for the middle layer of spines and conch bodies. The plot displays that the fracture stress increases from ~200 MPa (bodies) to ~260 MPa (spines).

To merely focus on the mechanical diversity between curving third-order lamellae (treated as reinforcements) in spines and straight-shape reinforcements in conch bodies, the middle layers were herein isolated from both materials for evaluation. Based on the listed stress-stain curves (Figure 5.3), it is clearly to conclude the better performance of spines than body parts upon foreign aggression. The improvement by 30% in compressive stress prompts us to unravel why the curving reinforcements surpass straight units.

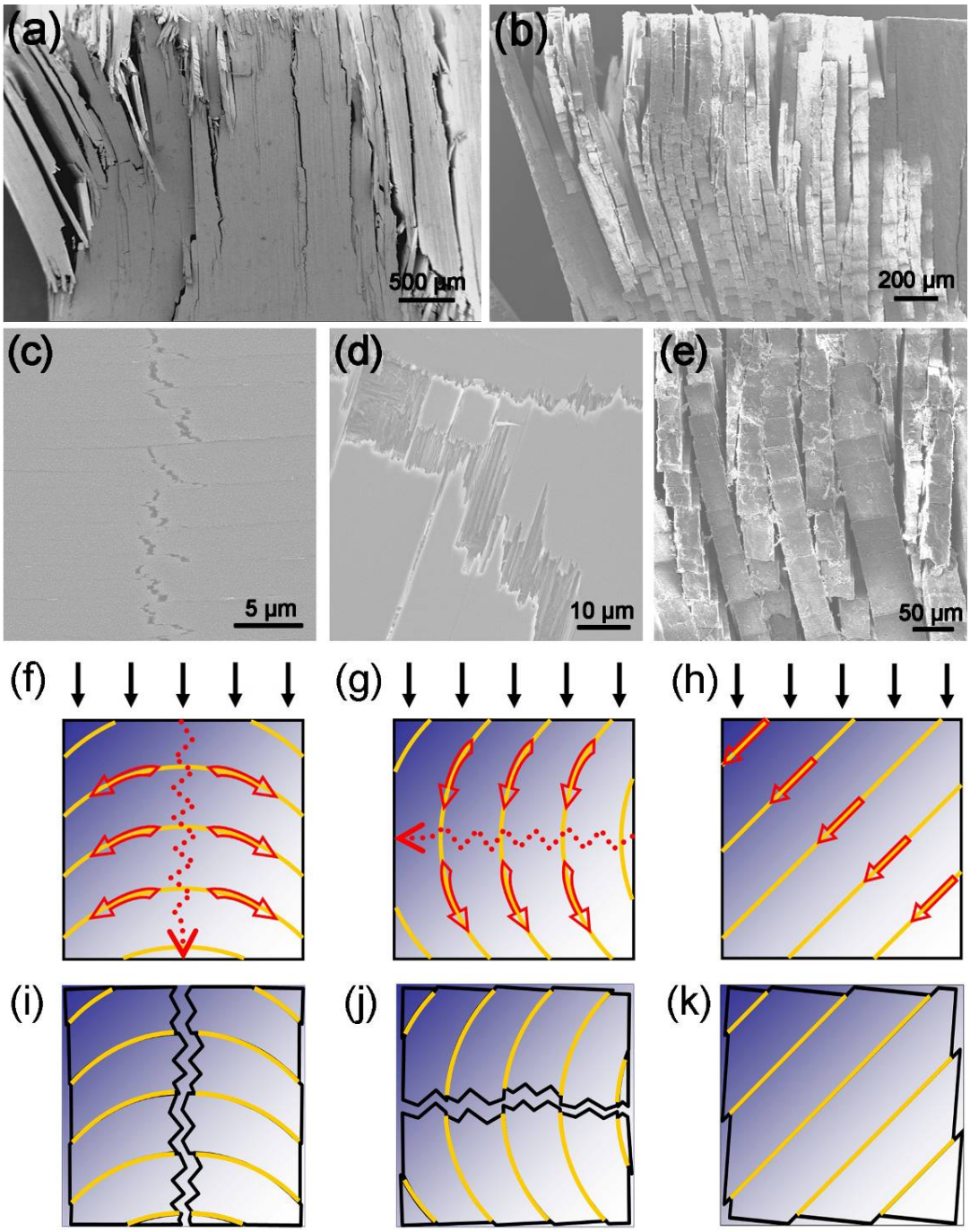

Figure 5.4. Fracture mechanisms of conch spine and shell body. (a) and (b) Fracture surfaces of the spine and body part, respectively, showing the cleavage is mainly along first-order lamellar interfaces. (c) and (d) Detailed information of the lamellae breakage in spine. (e) Close-up view of (b) displays that numerous detached second-order lamellae form the step-like surface. (f) and (i), (g) and (j) are sketches of fracture behaviors for different first-order lamellae in spine, separately. (h) and (k) display the lamellae sliding model in conch body.

The fractographic features upon compression for spine and body samples are correspondingly exhibited in Figures 5.4a and b. Crack induced first-order lamellar separations dominated in both sorts of specimens. Nevertheless, close-up views (Figures 5.4c - e) reveal that fracture behaviors in these two counterparts were varied within first-order lamellae. In the spine, the cracking routes depended on the orientation of curving lamellae. Under the arch-bridge arrangement in Figure 5.4c, despite assembled into compact condition, the top section of each arch is still characterized as higher possibility of intense stress concentration than the rest part due to soft interfaces.[86] Consequently, cracks were inclined to propagate vertically by breaking second- and third-order lamellae; during which, the finding deflected cracks along the second-order lamellar interfaces contribute to the fracture toughness of biocomposite (Figures 5.4f and i). In view of the other first-order construction (Figures 5.4d, g and j) differing as 90^0-diversity in third-order lamellae orientation, fracture behaviors are comparable to the aforementioned but with the horizontal direction in main cracking. In contrast, the step-like surface of conch body that consists of detached second-order lamellae (Figure 5.4e) indicates that the sliding along second-order interfaces (Figures 5.4h and k) instead of lamellar breakage becomes the dominant mode in conch body. We are curious to know: Why do not spines adopt the similar fracture strategy of conch bodies? The underlined aspect in sliding effect is, consequently, analyzed from the standpoint of stress equilibrium.

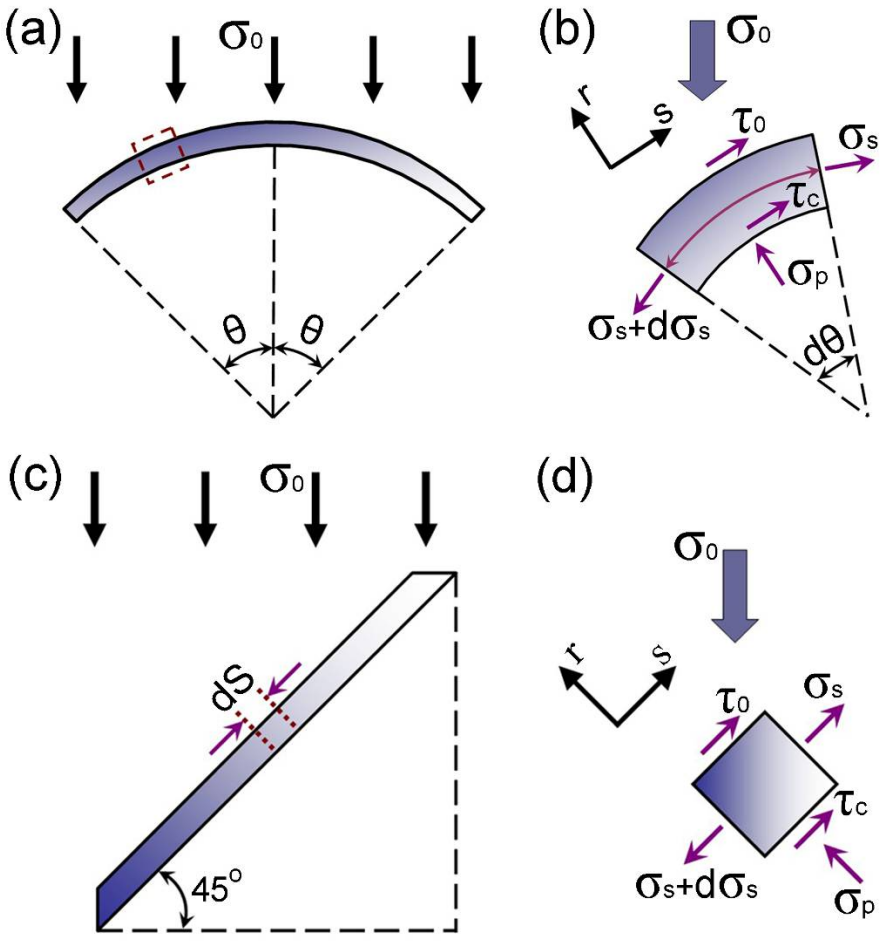

Figure 5.5. Models of curving and straight second-order lamellae and their stress equilibrium analysis. (a) Sketch of a single curving second-order lamella subjected to compression. (b) Stress equilibrium analysis of a segment from (a). (c) and (d) A straight second-order lamella upon compression and its stress equilibrium analysis, respectively.

Judging by the fracture pathways in Figure 5.4, we treat the second-order lamella as the object of interest. In conch spine (Figure 5.5a), the effect of curvature during sliding is analyzed by shear lag model[131,132] in assuming two friction origins, i.e., constant friction (originating from biopolymer bonding) and Coulomb friction[58,133] (from the lamellar asperities and surface normal stress). The stress equilibrium is based on the setup

coordinate system (Figure 5.5b) with axes ′s′ and ′r′ representing the tangential and perpendicular directions along the analyzed unit, respectively. In this context, we assume the upper and lower surfaces are subjected to friction force instead of four sides because the first-order lamellar separation occurs ahead of sliding. Accordingly, the equilibrium in s-direction is listed as below,

$$\begin{aligned}&\sigma_S \cdot b^2 \cdot \cos\frac{d\theta}{2} + \tau_0 \cdot b \cdot [Rd\theta + (R+b)d\theta] + \tau_C \cdot Rd\theta \cdot b \\ &= (\sigma_S + d\sigma_S) \cdot b^2 \cdot \cos\frac{d\theta}{2} + \sigma_0 \cdot b \cdot (R+b)d\theta \cdot \sin\theta\end{aligned} \quad 5.1$$

where σ_S is the stress on the cross section; σ_0 denotes the applied stress; b represents the width of second-order lamella (cross section is simplified as square). The lamellar geometry is characterized as angle θ plus fiber curvature R; τ_0 and τ_C are constant and Coulomb friction stress, respectively.

On the other hand, Equations 5.2 and 5.3 in the following express the r-direction mechanical equilibrium,

$$\sigma_P \cdot b \cdot Rd\theta = [\sigma_S \cdot \sin\frac{d\theta}{2} + (\sigma_S + d\sigma_S)\sin\frac{d\theta}{2}] \cdot b^2 + \sigma_0 \cdot b \cdot (R+b)d\theta \cdot \cos\theta \quad 5.2$$

$$\tau_C = \mu\sigma_P \quad 5.3$$

where σ_P is the radial compressive stress, and Coulomb friction coefficient is signified by μ. Substituting Equations 5.2 and 5.3 into Equation 5.1, we obtain the solution for σ_S:

$$\sigma_S = \frac{\sigma_0 \cdot R}{b} \cdot \frac{2\mu \cdot \sin\theta + (1-\mu^2) \cdot \cos\theta}{1+\mu^2} + C \cdot e^{\mu\theta} - \frac{2R\tau_0}{b\mu} \quad 5.4$$

here, the free ends lead to the condition of $\sigma_S = 0$ if $\theta = -\pi/4, 0, \pi/4$. Therefore,

$$\sigma_0 = \frac{2\tau_0 \cdot (e^{\pi\mu/4} - 1) \cdot (1 + \mu^2)}{\mu \cdot [(1 - \mu^2)e^{\mu\pi/4} + (\frac{\sqrt{2}}{2}\mu^2 - \sqrt{2}\mu - \frac{\sqrt{2}}{2})]} \quad 5.5$$

Concerning the straight lamella (conch body) in s and r directions, equilibrium states are evaluated in the following, respectively.

$$\sigma_S \cdot b^2 + \tau_0 \cdot 2b \cdot ds + \tau_C \cdot b \cdot ds = (\sigma_S + d\sigma_S) \cdot b^2 + \sigma_0^{'} \cdot b \cdot ds \cdot \sin 45^0 \quad 5.6$$

$$\sigma_P \cdot b \cdot ds = \sigma_0^{'} \cdot b \cdot ds \cdot \cos 45^0 \quad 5.7$$

$$\tau_C = \mu\sigma_P \quad 5.3$$

After substituting Equations 5.7 and 5.3 into Equation 5.6, the solution for σ_S is

$$\sigma_S = (\frac{2\tau_0}{b} + \frac{\sqrt{2}}{2b}\mu\sigma_0^{'} - \frac{\sqrt{2}}{2b}\sigma_0^{'})S \quad 5.8$$

where σ_0' is the applied stress for the straight part. After considering the boundary condition, σ_0' is calculated as followed:

$$\sigma_0^{'} = \frac{2\sqrt{2}}{1 - \mu}\tau_0 \quad 5.9$$

The applied stresses, σ_0 and σ_0', are therefore related to the constant friction stress and Coulomb friction coefficient. Since the Coulomb friction coefficient (μ) is determined as 0.13 in the friction test (Figure 5.6), σ_0 and σ_0' are presented in terms of constant friction stress (τ_0). Accordingly, the calculated values ($\sigma_0 = 8.01\tau_0$, $\sigma_0' = 3.25\tau_0$) obviously mirror the stress initiated by sliding for the curving lamellae is much higher than that of straight-shape assembly entity, resulting in an easy but still tough fracture manner in spines - second-order lamellar breakage. Over the past decades of manufacturing composites, the reinforcements (fibers, plates, rods, etc.) with curvature

lack enough considerations. Our finding suggests that if curving reinforcements are arranged properly, the mechanical performance can be significantly enhanced.

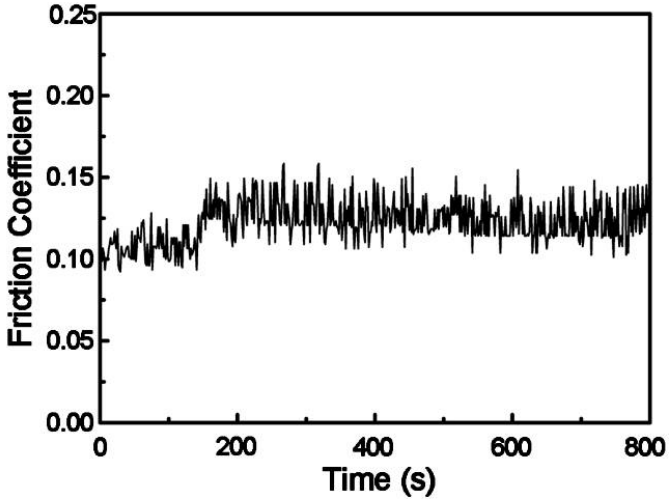

Figure 5.6 Friction coefficient of conch shells.

5.3 SUMMARY

In summary, we have reported the curve-shaped reinforcements' assembly strategy in conch-spine biocomposites for the first time. The fracture strength of such design principle is increased up to 30 % in comparison with conch bodies in straight-shape reinforcements. This performance discrepancy derives from the higher initiated stress for lamellae breakage than conch bodies' lamellae sliding resistance. In association with our finding exquisite Mother Nature's design and machinery, it might open up new avenues for scientists to produce parallel materials.

CHAPTER 6

THERMAL INVESTIGATIONS ON STRUCTURAL AND MECHANICAL EVOLUTION OF CONCH SHELLS

Studies are mainly centered on the natural shells and little is known about their thermal stability. Herein, several questions need to answer: How does heat treatment affect conch shells' hierarchical structure and mechanical robustness? Is it applicable to elevate working temperature? At what range of temperature can shells maintain the remarkable mechanical properties? Can we learn from the biocomposites upon thermal treatment? In this letter, the temperatures of biopolymer removal and phase transformation were identified by TGA (thermogravimetric analysis) and DTA (differential thermal analysis). We applied a combination of state-of-art methods including X-ray diffraction, scanning electron microscopy, transmission electron microscopy, atomic force microscopy and nanoindentation to conch shells to unveil the variation of multiscale structure and resulted mechanical properties under different heating violations. It is reported that both induced biopolymer degradation and phase transformation (aragonite - calcite - lime) by heat treatment significantly decrease the mechanical response of conch shells. Our thermal investigation advances the understanding of thermal behaviors in conch shells and provides design guidelines for bioinspired materials and sensors.

6.1 EXPREIMENTAL

Thermogravimetric analysis and differential thermal analysis were first performed on conch specimen in using the Thermal Analysis Instruments SDT2960 Thermogravimetric Analyzer at the heating rate 20 °C/min in air. On basis of the results from aforementioned experiments, samples were air heated in a furnace at 310 °C, 500 °C, 900 °C for 1 h, respectively, and all of them were cooled down to room temperature afterwards. The phases of pristine (without heat treatment) and heat treated shells were characterized in XRD (Rigaku D/Max-2100 powder X-ray diffractometer with Bragg-Brentano geometry and CuK_{α} radiation), with FESEM and TEM (Hitachi H-8000) identifying the corresponding structures. Biopolymer of conch shells was isolated by hydrochloric acid (0.1 mol/L); processed for drying treatment, it was pressed into bulk material. Nanoindentation tests were executed on the investigated samples, including non-heated and heated samples, as well as bulk biopolymer, with coupled Triboscope nanomechanical testing system and Veeco AFM system. The values for hardness and elastic modulus were calculated from the recorded load-displacement curves. Indentation impressions were then imaged in Veeco AFM.

6.2 RESULTS AND DISCUSSION

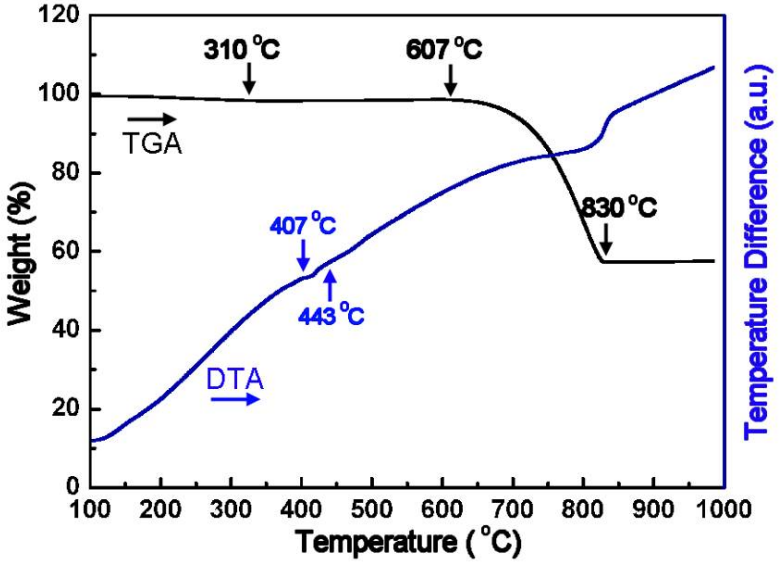

Figure 6.1. TGA and DTA curves of the conch specimen upon heat treatment to 1000 °C in air.

As shown in Figure 6.1, TGA curve reveals a weight loss of about 1.7 % at 310 °C, which was caused by the degradation[134-137] of organic matrix. In the range of 607 °C - 830 °C, another mass loss of 42 % occurred at the expense of decomposition from calcite (one kind of $CaCO_3$) to lime (CaO), in good agreement with the generally accepted endothermic reaction temperature and theoretical value[92] for the CO_2 loss (44 wt%), respectively. In addition, an endothermic transformation from aragonite to calcite is found in the temperature range of 407 °C - 443 °C from the DTA curve. Consequently, the temperatures for heat treatment are settled with the reference to the aforementioned experimental results.

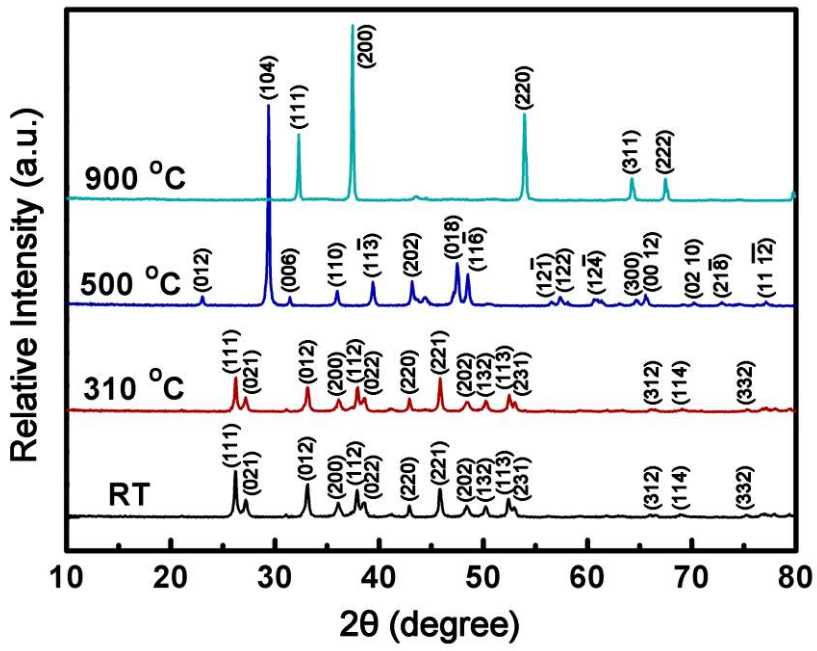

Figure 6.2. XRD patterns of conch samples heat treated with diverse temperatures.

Figure 6.2 displays the XRD patterns of conch samples treated with different heating parameters. After phase identification, all listed peaks from the pristine (RT) conch shells indicate the composition as aragonite - one metastable polymorph of calcium carbonate. The treatment under 310 °C burned out the biopolymer but preserved the aragonite as proved by the listed spectrum. After heated at 500 °C, the triggered phase transformation from aragonite to calcite (a more stable polymorph of calcium carbonate than aragonite) is demonstrated. Further heating up to 900 °C, the final substance (CaO) is hereby obtained, resulting from the calcium carbonate decomposition. The results from Figure 6.2 are consistent well with those in TGA and DTA curves.

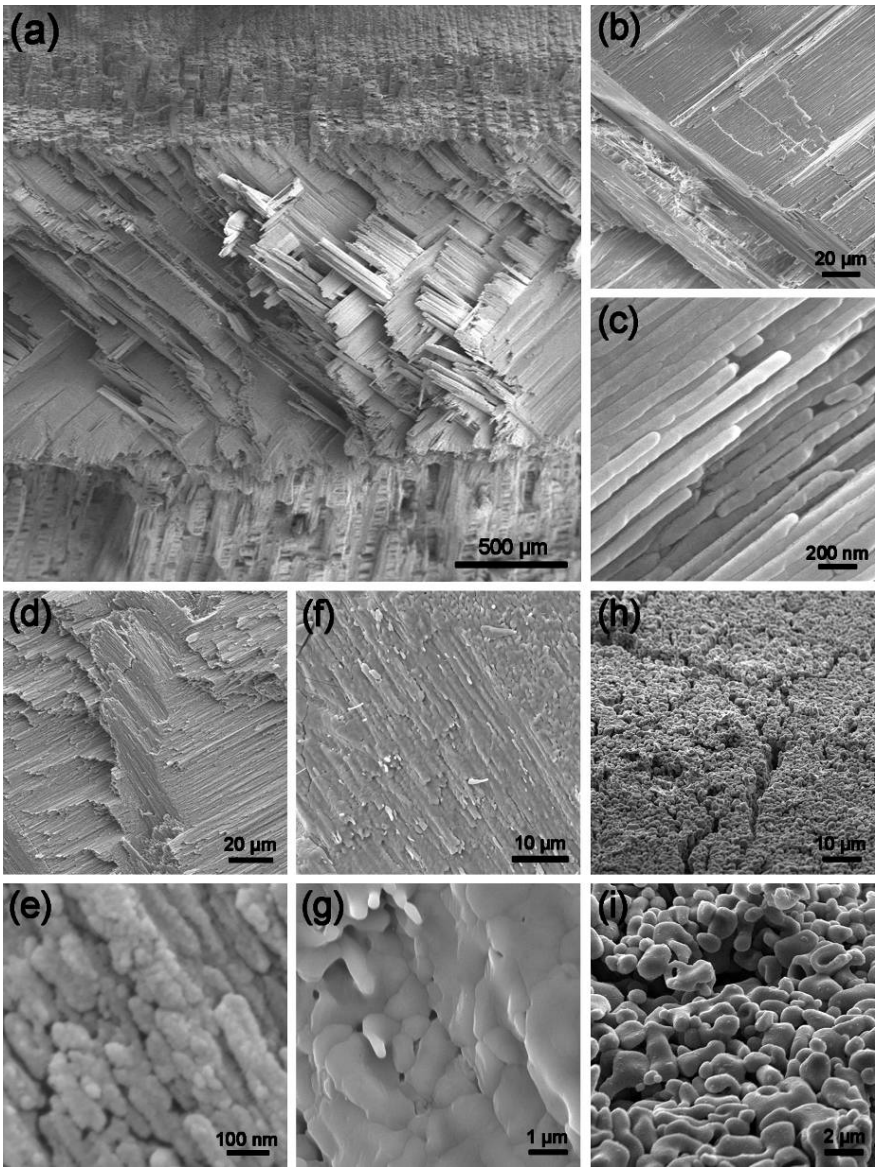

Figure 6.3. SEM images of pristine and heat treated conch shells. (a) Overview of the fresh shell's fracture surface with a hierarchical structure. (b) and (c) Detailed morphology of conch shell from (a), clearly showing the crossed-lamellar structure and nanowire-like third-order lamellae, respectively. (d) Cross section of the sample upon 310 °C treatment. (e) Close-up view of (d) shows the existence of nanoparticles in third-order lamellae after biopolymer burning out. (f) Fracture surface of a 500 °C-heated sample. (g) Magnification of (f) displays the calcite particles and nanoscale holes in between. (h) Image of the fractured shell after 900 °C heat treatment, indicating a porous architecture without crossed-lamellar characteristic. (i) Close-up view of (h) displays the formation of blood-cell-shape CaO particles.

Figure 6.3 shows the fracture morphology of pristine and heat treated bulk shells. Overview of pristine shell's fracture surface is presented in Figure 6.3a. Conch shell exhibits a crossed-lamellar structure with three layers (outer, middle and inner) based on diverse orientation of first-order lamellae as $0^0/90^0/0^0$. In Figures 6.3b and c, these close-up views display the nanowire-like third-order lamellae and their compact connection. Upon 310 °C heat treatment, the surfaced nanoparticles[138,139] inside third-order lamellae due to the loss of biopolymer demonstrate our previous conclusion[82] of nanoparticle assembly strategy. In the 500 °C-heated sample, the crossed-lamellar structure (Figure 6.3f) is still maintained despite the phase transformation from aragonite to calcite (Figure 6.1). Nevertheless, detailed examination of third-order lamellae displays grain coarsening and nanoscale holes amid calcite particles (Figure 6.3g). Here, the formation of nano-holes results from the burning-out stuffing (biopolymer) and lattice rearrangement during phase transformation.[91,140,141] The decomposition of calcium carbonate to calcium oxide at 900 °C rendered crossed-lamellar architecture 'disappear' (Figure 6.3h), replacing by a porous structure with blood-cell-shape CaO in microsize (Figure 6.3i) owing to the outgassing of CO_2 in mass and volume by 44 % and 55 %, respectively.[142]

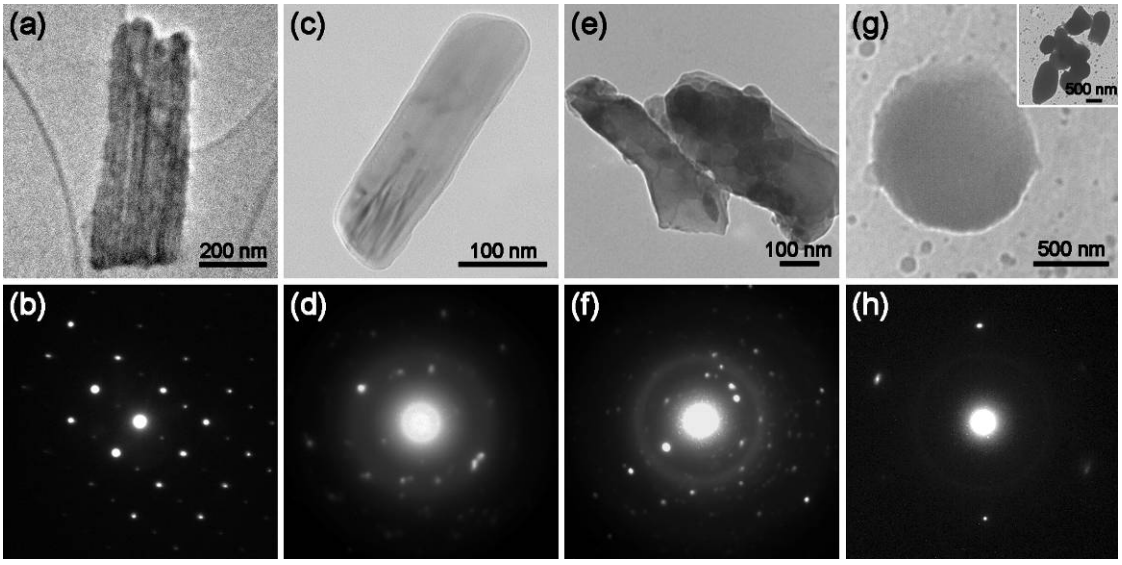

Figure 6.4. TEM analysis of heat treated samples. (a) and (b) TEM image of pristine shell and its electron diffraction pattern, respectively. (c), (e) and (g) TEM images of shells upon 310 °C, 500 °C and 900 °C heat treatments, respectively, with their corresponding electron diffraction patterns displayed in (d), (f) and (h).

In Figure 6.4a, the pristine shell with well-rounded third-order lamellae diffracts as single-crystal characteristic pattern (Figure 6.4b). In comparison, the polycrystalline-characteristic diffraction pattern in 310 °C-heated shell (Figures 6.4c and d) demonstrate the initiation of nanoparticles rotation after losing the connection from bonding biopolymer. Under 500 °C treatment (Figure 6.4e), the lamellar structure is still preserved in conch shell (in consistent with the observation in Figure 6.3f) but with a messy electron diffraction pattern (Figure 6.4f). It is believed that the phase transformation from aragonite to calcite, triggered by the high temperature, reshuffles ions arrangement and thus disorders the diffraction pattern.[140] Under the decomposition of calcite under 900 °C heating, third-order lamellae were collapsed into a pile of

microscale CaO particles, as shown in Figure 6.4g. Therefore, aragonite nanoparticles in pristine shell were finally transformed to microparticles of lime via the particle growth and/or agglomeration as well as decomposition under high temperature.

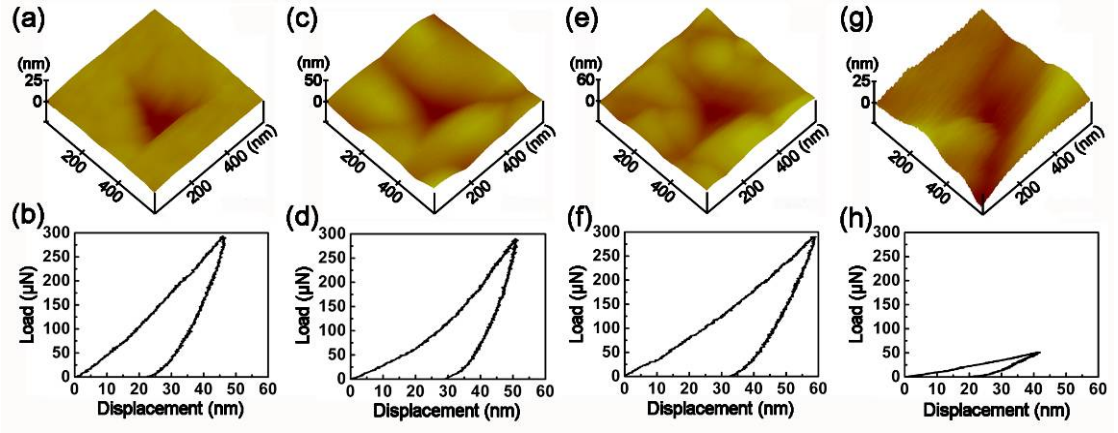

Figure 6.5. Nanoindentation impressions and corresponding load-displacement curves of shells upon heat treated at room temperature (a and b), 310 °C (c and d), 500 °C (e and f) and 900 °C (g and h).

To eliminate the anisotropic properties of hierarchical structure, nanoindentation tests were loaded at the same angle to the third-order lamellae in all experimental samples. Figure 6.5 shows the representative AFM images of nanoindentation impressions and corresponding load-displacement curves. In Figures 6.5a - f, within the same loading, the gradually enlarged indentation marks and increased displacements accompanied by the increment of heating temperature (from room temperature to 500 °C) indicate the trend of elevated temperature in lessening mechanical properties of shells. In 900 °C heat treated conch sample, the finding porous structure (Figure 6.3i) is incapable of undertaking any mechanical aggression, resulting in the weak response (Figures 6.5g and h).

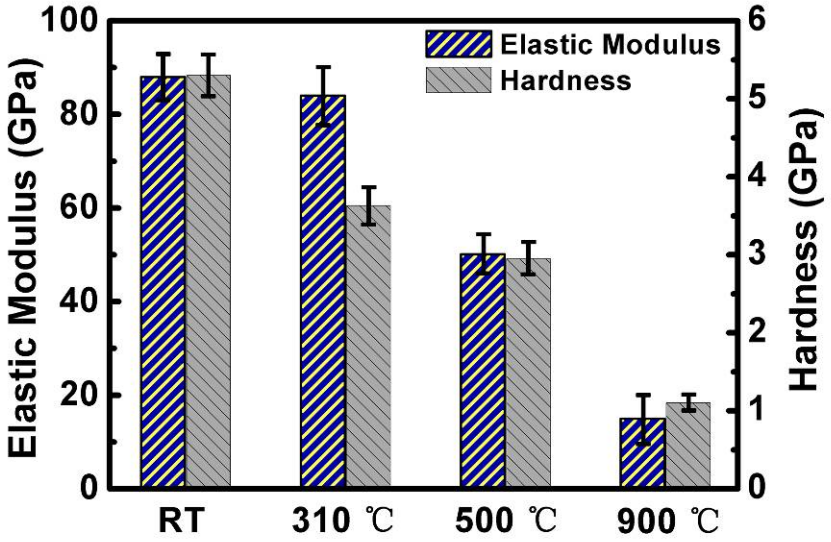

Figure 6.6. Values in hardness and elastic modulus of shells heat treated at different temperatures.

Determined by the nanoindentation load-displacement curves in Figure 6.5, the derived hardness and elastic modulus values of conch shells under different heat treated conditions are listed in Figure 6.6. The gradually weakened mechanical performance by the increased-temperature treatment is consistent well with the observation in Figures 6.5. Comparing with pristine shell, the dropped-off properties upon 310 °C is developed from biopolymer removal, with which holds up the aragonite nanoparticles tightly. The induced formation of holes because of phase transformation (aragonite to calcite) and loss of biopolymer contribute to mechanical instability after 500 °C treatment, while the sharp loss in hardness and elastic modulus (under 900 °C heat treatment) is mainly caused by the weak porous structure upon phase transformation (aragonite - calcite - lime). Next, we will address the mechanical role of biopolymer.

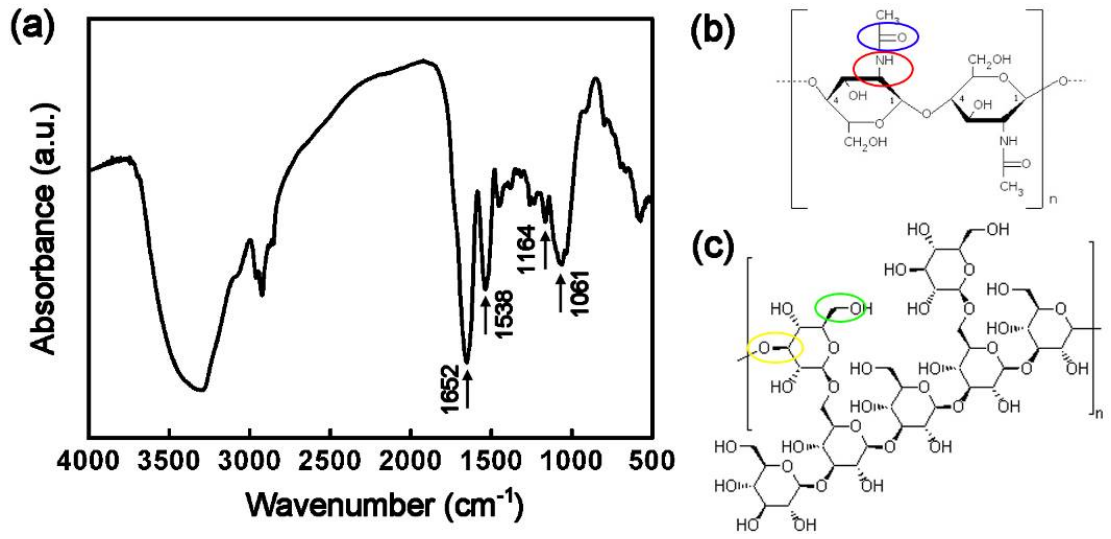

Figure 6.7. Biopolymer identification. (a) FTIR spectra of biopolymer. (b) and (c) Molecular structures of polysaccharide and chitin, respectively.

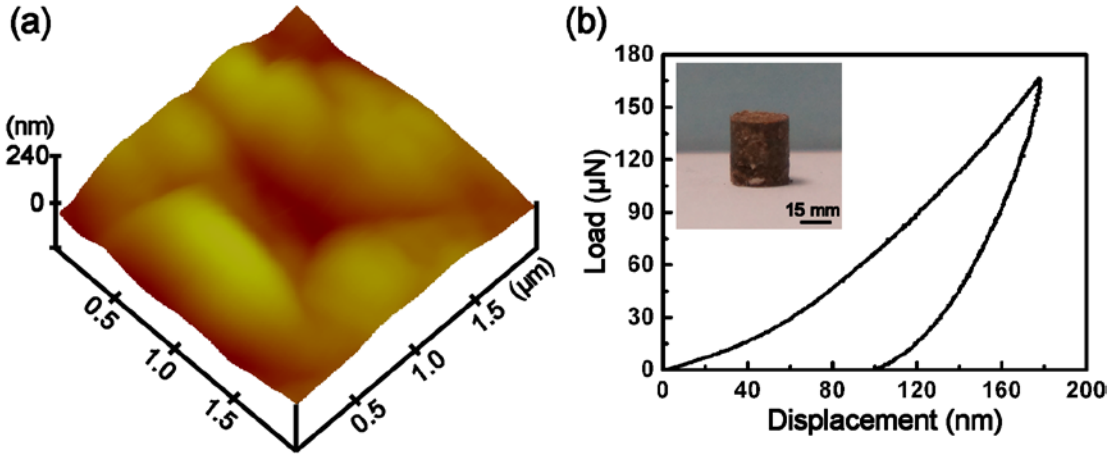

Figure 6.8. Mechanical characterization of biopolymer. (a) Representative nanoindentation impression of biopolymer and its load-displacement curve (b).

Biopolymer, as the organic constituent of conch shells, is renowned as the significant role in achieving and maintaining biomaterials' high mechanical performance. Isolated by diluted hydrochloric acid, we identified the existence of polysaccharide and chitin in studied biopolymer (Figure 6.7) by FTIR (fourier transform infrared

spectroscopy) analysis, both of them are reported as the main constituents during conch shells biomineralization.[143] Moreover, after compressed into bulk material, nanoindentation tests were carried out to investigate its mechanical properties. Figure 6.8 shows the nanoidentation impression and corresponding load-displacement curve; the derived elastic modulus (~ 4.5 GPa) and hardness (~ 0.4 GPa) form a sharp contrast to the stiff pristine aragonite (Figure 6.6). Being soft, though, the biopolymer essentially improves the mechanical reliability (Figures 6.5 and 6.6) via its rubber-band effect in coordinating deformation and increasing slip resistance of adjacent lamellae, and thus prevents early cracking. This improvement is further proved by the higher compressive strength in pristine shell than that of heat treated sample (310 °C) without biopolymer (Figure 6.9).

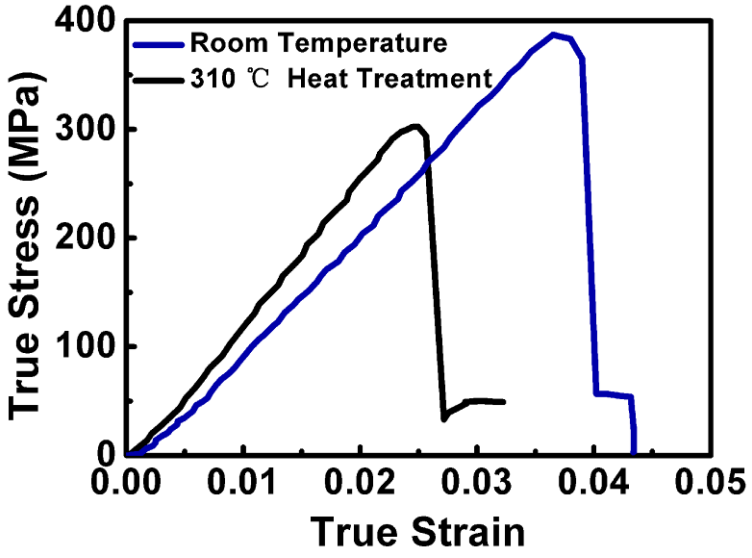

Figure 6.9. Compressive true stress-strain curves of fresh and 310 °C heat treated conch shells.

6.3 SUMMARY

The reported biopolymer removal and phase transformation demonstrate the instability of aragonite-biopolymer constructed conch shells upon heating. The easy-to-burn biopolymer, despite low content, essentially plays a vital role in sustaining the mechanical reliability of conch shells. The crossed-lamellar structure is still maintained in 500 °C heat treated shells but characterized as calcite particles and interspersed nanoscale holes mainly due to phase transformation. Heat treated shells upon 900 °C exhibit porous structure with microsized lime particles in lieu of the crossed-lamellar architecture because of calcite decomposition. Degraded biopolymer and phase transformation (aragonite - calcite - lime) render the sharp loss in mechanical properties accompanied by intensifying heating conditions.

CHAPTER 7

SUMMARY AND FUTURE SUGGESTIONS

7.1 SUMMARY OF MAIN RESULTS

The individual building blocks, third-order lamellae, in conch shells are structurally composed of aragonite nanoparticles, via AFM, SEM and HRTEM observation. The ceramic-based third-order lamellae exhibit not only elasticity but also plasticity, overturning the general assumption of brittleness. Such metal-like deformation behavior is ascribed to the unique nanoparticle-biopolymer architecture of the third-order lamellae, in which the biopolymer mediates the rotation of aragonite nanoparticles in response to external loading. The finding alleviates the stress concentration and inhibits direct lamellae breakage. Together with conch shells' crossed-lamellar architecture, cracks are interlocked and deflected along interfaces in a three-dimensional manner, thus confining the damage region and realizing coupled ultra-high strength and toughness.

Conch shells exhibit elevated fracture strength upon high-strain-rate compression vis-à-vis that under quasi-static loading. The activated defense mechanism - intra-lamella fracture, involving nanoparticle rotation as well as formation of trapped dislocation, against high-speed predatory attacks is triggered by the small localized plastic activation

volume, forming a contrast to the inter-lamella fracture damage upon quasi-static violation.

As the main tools for self-defense, conch spines overmatch the conch bodies with the advantage of curve-shaped third-order lamellae. The mechanical improvement is attributed to the curvature effect in breaking lamellae instead of lamellae sliding in conch bodies. The hierarchically arranged reinforcements with curvature provide innovative design guidelines for developing composites.

The superior mechanical performance and delicate hierarchical structure of conch shells are gradually deteriorated because of the sequentially induced biopolymer removal and phase transformation (aragonite - calcite - lime) by increasing the temperature of heat treatment.

7.2 SUGGESTIONS FOR FUTURE RESEARCH

Conch shells' multiscale crossed-lamellar structure, till now, has not been completely reproduced. Although some relative studies reported the fabrication, their mechanical performance cannot compete with such bioceramics due to the lack of understanding in nanoscale structure details. The new finding in nanoparticle-biopolymer assembly strategy, hopefully, can provide a template for the manufacture of engineered composites. Moreover, inspired by the weakened mechanical performance of conch shells after soft biopolymer removal, it would be promising to elevate the mechanical response of composites via injecting soft materials with good fluidity and adhesion into porous reinforcements. Additionally, considering the availability of seashells, is it possible to

utilize the existed nanoparticle-biopolymer construction to produce composites with better performance? Predictably, this environment-friendly method will become a trend in future.

Besides the studied crossed-lamellar construction in this dissertation, there have several other identified hierarchical arrangements, for example, nacreous, prismatic, and foliated structures, all of which have been systematically investigated. The common impressive acknowledgement of these bioceramics' is outstanding mechanical performance that man-made materials can never achieve. However, comprehensive comparison among these structures is seldom reported. A couple of questions are raised, but not answered: Which hierarchical structure owns the best mechanical performance? Which is the easiest assembly strategy to mimic? Studying these issues is expected to contribute to the field of fabricating bioinspired materials.

REFERENCES

[1] R. O. Ritchie. The conflicts between strength and toughness. *Nature Materials* 10 (2011) 817-822.

[2] M. E. Launey, and R. O. Ritchie. On the fracture toughness of advanced materials. *Advanced Materials* 21 (2009) 2103-2110.

[3] S. Kumar, and W. A. Curtin. Crack interaction with microstructure. *Materials Today* 10 (2007) 34-44.

[4] A. Y. M. Lin, M. A. Meyers, and K. S. Vecchio. Mechanical properties and structure of *Strombus gigas*, *Tridacna gigas*, and *Haliotis rufescens* sea shells: a comparative study. *Materials Science and Engineering C* 26 (2006) 1380-1389.

[5] H. D. Espinosa, J. E. Rim, F. Barthelat, and M. J. Buehler. Merger of structure and material in nacre and bone - perspectives on *de novo* biomimetic materials. *Progress in Materials Science* 54 (2009) 1059-1100.

[6] M. A. Meyers, P. Y. Chen, A. Y. Lin, and Y. Seki. Biological materials: structure and mechanical properties. *Progress in Materials Science* 53 (2008) 1-206.

[7] X. D. Li, W. C. Chang, Y. J. Chao, R. Z. Wang, and M. Chang. Nanoscale structural and mechanical characterization of a natural nanocomposite material: the shell of red abalone. *Nano Letters* 4 (2004) 613-617.

[8] E. Munch, M. E. Launey, D. H. Alsem, E. Saiz, A. P. Tomsia, and R. O. Ritchie. Tough, bio-inspired hybrid materials. *Science* 322 (2008) 1516-1520.

[9] K. Simkiss, and K. M. Wilbur. *Biomineralization*. Academic Press, San Diego, 1989.

[10] C. Ortiz, and M. C. Boyce. Bioinspired structural materials. *Science* 319 (2008) 1053-1054.

[11] J. D. Currey. Hierarchies in biomineral structures. *Science* 309 (2005) 253-254.

[12] J. D. Currey, and J. D. Taylor. The mechanical behaviour of some molluscan hard tissues. *Journal of Zoology* 173 (1974) 395-406.

[13] M. Suzuki, J. Kameda, T. Sasaki, K. Saruwatari, H. Nagasawa, and T. Kogure. Characterization of the multilayered shell of a limpet, *Lottia kogamogai* (Mollusca: Patellogastropoda), using SEM-EBSD and FIB-TEM techniques. *Journal of Structural Biology* 171 (2010) 223-230.

[14] A. Hayashi, N. Yokoo, T. Nakamura, T. Watanabe, H. Nagasawa, and T. Kogure. Crystallographic characterization of the crossed lamellar structure in the bivalve *Meretrix lamarckii* using electron beam techniques. *Journal of Structural Biology* 176 (2011) 91-96.

[15] A. B. Rodriguez-Navarro, A. Checa, M. G. Willinger, R. Bolmaro, and J. Bonarski. Crystallographic relationships in the crossed lamellar microstructure of the shell of the gastropod *Conus marmoreus*. *Acta Biomaterialia* 8 (2012) 830-835.

[16] N. V. Wilmot, D. J. Barber, J. D. Taylor, and A. L. Graham. Electron microscopy of molluscan crossed-lamellar microstructure. *Philosophical Transactions: Biological Sciences* 337 (1992) 21-35.

[17] W. L. Bragg. The structure of aragonite. *Proceedings of the Royal Society of London* 105 (1924) 16-39.

[18] L. Qiao, and Q. L. Feng. Study on twin stacking faults in vaterite tablets of freshwater lacklustre pearls. *Journal of Crystal Growth* 304 (2007) 253-256.

[19] M. Suzuki, T. Kogure, S. Weiner, and L. Addadi. Formation of aragonite crystals in the crossed lamellar microstructure of limpet shells. *Crystal Growth & Design* 11 (2011) 4850-4859.

[20] B. Pokroy, and E. Zolotoyabko. Microstructure of natural plywood-like ceramics: a study by high-resolution electron microscopy and energy-variable X-ray diffraction. *Journal of Materials Chemistry* 13 (2003) 682-688.

[21] I. M. Weiss, N. Tuross, L. Addadi, and S. Weiner. Mollusc larval shell formation: amorphous calcium carbonate is a precursor phase for aragonite. *Journal of Experimental Zoology* 293 (2002) 478-491.

[22] A. W. Xu, Y. R. Ma, and H. Cölfen. Biomimetic mineralization. *Journal of Materials Chemistry* 17 (2007) 415-449.

[23] N. Koga, Y. Z. Nakagoe, and H. Tanaka. Crystallization of amorphous calcium carbonate. *Thermochimica Acta* 318 (1998) 239-244.

[24] L. A. Gower, and D. A. Tirrell. Calcium carbonate films and helices grown in solutions of poly(aspartate). *Journal of Crystal Growth* 191 (1998) 153-160.

[25] L. Addadi, and S. Weiner. Control and sesign principles in biological mineralization. *Angewandte Chemie-International Edition in English* 31 (1992) 153-169.

[26] Y. Politi, T. Arad, E. Klein, S. Weiner, and L. Addadi. Sea urchin spine calcite forms via a transient amorphous calcium carbonate phase. *Science* 306 (2004) 1161-1164.

[27] J. Seto, Y. Ma, S. A. Davis, F. Meldrum, A. Gourrier, Y. Y. Kim, U. Schilde, M. Sztucki, M. Burghammer, S. Maltsev, C. Jager, and H. Cölfen. Sturcture-property relationships of a biological mesocrystal in the adult sea urchin spine. *Proceedings of the National Academy of Science of the United States of America* 109 **(**2012) 3699-3704.

[28] H. Cölfen. Bio-inspired mineralization using hydrophilic polymers. *Topics in Current Chemistry* 271 (2007) 1-77.

[29] S. Weiner, W. Traub, and S. B. Parker. Macromolecules in mollusc shell and their functions in biomineralization. *Philosophical Transactions of the Royal Society of London* 304 (1984) 425-434.

[30] X. W. Su, D. M. Zhang, and A. H. Heuer. Tissue regeneration in the shell of the giant queen conch, *Strombus gigas*. *Chemistry of Materials* 16 (2004) 581-593.

[31] V. R. Meenakshi, P. L. Blackwelder, and K. M. Wilbur. An ultrastructural study of shell regeneration in *Mytilus edulis* (Mollusca: Bivalvia). *Journal of Zoology* 171 (1973) 475-484.

[32] V. R. Meenakshi, A. W. Martin, and K. M. Wilbur. Shell repair in Nautilus macromphalus. *Marine Biology* 27 (1974) 27-35.

[33] V. R. Meenakshi, G. Donnay, P. L. Blackwelder, and K. M. Wilbur. The influence of substrata on calcification patterns in molluscan shell. *Calcified Tissue Research* 15 (1974) 31-44.

[34] V. R. Meenakshi, P. L. Blackwelder, P. E. Hare, K. M. Wilbur, and N. Watabe. Studies on shell regeneration - I. matrix and mineral composition of the normal and

regenerated shell of *Pomacea paludosa*. *Comparative Biochemistry and Physiology* 50 (1975) 347-351.

[35] C. Reed-Miller. Scanning electron microscopy of the regenerated shell of the marine archaeogastropod, *Tegula*. *Biological Bulletin* 165 (1983) 723-732.

[36] L. S. Eyster. Shell inorganic composition and onset of shell mineralization during bivalve and gastropod embryogenesis. *Biological Bulletin* 170 (1986) 211-231.

[37] C. Fleury, F. Marin, B. Marie, G. Luquet, J. Thomas, C. Josse, A. Serpentini, and J. M. Lebel. Shell repair process in the green ormer Haliotis tuberculata: a histological and microstructural study. *Tissue and cell* 40 (2008) 207-218.

[38] M. Kijima, Y. Oaki, and H. Imai. In vitro repair of a biomineral with a mesocrystal structure. *Chemistry - A European Journal* 17 (2011) 2828-2832.

[39] K. Wada. Spiral growth of calcitostracum. *Nature* 219 (1968) 62.

[40] R. S. Prezant, and A. T. Tiu. Spiral crossed-lamellar shell growth in *Corbicula* (Mollusca: Bivalvia). *Transactions of the American Microscopical Society* 105 (1986) 338-347.

[41] H. Nakahara, M. Kakei, and G. Bevelander. Studies on the formation of the crossed lamellar structure in the shell of *Strombus gigas*. *Veliger* 23 (1981) 207-211.

[42] R. L. Penn, and J. F. Banfield. Morphology development and crystal growth in nanocrystalline aggregates under hydrothermal conditions: insights from titania. *Geochimica et Cosmochimica Acta* 63 (1999) 1549-1557.

[43] J. F. Banfield, S. A. Welch, H. Z. Zhang, T. T. Ebert, and R. L. Penn. Aggregation-based crystal growth and microstructure development in natural iron oxyhydroxide biomineralization products. *Science* 289 (2000) 751-754.

[44] L. B. Yang, Y. H. Shen, A. J. Xie, and J. J. Liang. Oriented attachment growth of three-dimensionally packed trigonal selenium microspheres into large-area wire networks. *European Journal of Inorganic Chemistry* 28 (2007) 4438-4444.

[45] T. Sugimoto. Preparation of monodispersed colloidal particles. *Advances in Colloid and Interface Science* 28 (1987) 65-108.

[46] L. T. Kuhn-Spearing, H. Kessler, E. Chateau, R. Ballarini, A. H. Heuer, and S. M. Spearing. Fracture mechanisms of the *Strombus gigas* conch shell: implications for the design of brittle laminates. *Journal of Materials Science* 31 (1996) 6583-6594.

[47] D. F. Hou, G. S. Zhou, and M. Zheng. Conch shell structure and its effect on mechanical behaviors. *Biomaterials* 25 (2004) 751-756.

[48] S. Kamat, X. Su, R. Ballarini, and A. H. Heuer. Structural basis for the fracture toughness of the shell of the conch *Strombus gigas*. *Nature* 405 (2000) 1036-1040.

[49] R. Menig, M. H. Meyers, M. A. Meyers, and K. S. Vecchio. Quasi-static and dynamic mechanical response of *Strombus gigas* (conch) shells. *Materials Science and Engineering A* 297 (2001) 203-211.

[50] W. Yang, G. P. Zhang, X. F. Zhu, X. W. Li, and M. A. Meyers. Structure and mechanical properties of *Saxidomus purpuratus* biological shells. *Journal of the Mechanical Behavior of Biomedical Materials* 4 (2011) 1514-1530.

[51] R. Z. Wang, Z. Suo, A. G. Evans, N. Yao, and I. A. Aksay. Deformation mechanisms in nacre. *Journal of Materials Research* 16 (2001) 2485-2493.

[52] A. G. Evans, Z. Suo, R. Z. Wang, I. A. Aksay, M. Y. He, and J. W. Hutchinson. Model for the robust mechanical behavior of nacre. *Journal of Materials Research* 16 (2001) 2475-2484.

[53] H. J. Gao, B. H. Ji, I. L. Jager, E. Arzt, and P. Fratzl. Materials become insensitive to flaws at nanoscale: lessons from nature. *Proceedings of the National Academy of Sciences of the United States of America* 100 (2003) 5597-5600.

[54] M. A. Meyers, P. Y. Chen, M. I. Lopez, Y. Seki, and A. Y. M. Lin. Biological materials: a materials science approach. *Journal of the Mechanical Behavior of Biomedical Materials* 4 (2011) 626-657.

[55] J. Zhao, C. Chen, Y. Liang, and J. Wang. Mechanical properties and structure of *Haliotis discus hannai ino* and *Hemifusus tuba* conch shells: a comparative study. *Acta Mechanica Sinica* 26 (2010) 21-25.

[56] Y. Liang, J. Zhao, L. Wang, and F. M. Li. The relationship between mechanical properties and crossed-lamellar structure of mollusk shells. *Materials Science and Engineering A* 483-484 (2008) 309-312.

[57] Z. H. Xu, and X. D. Li. Deformation strengthening of biopolymer in nacre. *Advanced Functional Materials* 21 (2011) 3883-3888.

[58] B. H. Ji, and H. J. Gao. Mechanical properties of nanostructure of biological materials. *Journal of the Mechanics and Physics of Solids* 52 (2004) 1963-1990.

[59] B. H. Ji, and H. J. Gao. How do slender mineral crystals resist buckling in biological materials? *Philosophical Magazine Letters* 84 (2004) 631-641.

[60] S. Kamat, H. Kessler, R. Ballarini, M. Nassirou, and A. H. Heuer. Fracture mechanisms of the *Strombus gigas* conch shell: II-micromechanics analyses of multiple cracking and large-scale crack bridging. *Acta Materialia* 52 (2004) 2395-2406.

[61] H. Kessler, R. Ballarini, R. L. Mullen, L. T. Kuhn, and A. H. Heuer. A biomimetic example of brittle toughening: (I) steady state multiple cracking. *Computational Materials Science* 5 (1996) 157-166.

[62] J. Cook, J. E.Gordon, C. C. Evans, and D. M. Marsh. A mechanism for the control of crack propagation in all-brittle systems. *Proceedings of the Royal Society of London* 282A (1964) 508-520.

[63] W. Yang, I. H. Chen, B. Gludovatz, E. A. Zimmermann, R. O. Ritchie, and M. A. Meyers. Natural flexible dermal armor. *Advanced Materials* 25 (2013) 31-48.

[64] W. Yang, N. Kashani, X. W. Li, G. P. Zhang, and M. A. Meryers. Structural characterization and mechanical behavior of a bivalve shell (*Saxidomus purpuratus*). *Materials Science and Engineering C* 31 (2011) 724-729.

[65] N. M. Neves, and J. F. Mano. Structure/mechanical behavior relationships in crossed-lamellar sea shells. *Materials Science and Engineering C* 25 (2005) 113-118.

[66] S. J. Eichihorn, D. J. Scurr, P. M. Mummery, M. Golshan, S. P. Thompson, and R. J. Cernik. The role of residual stress in the fracture properties of a natural ceramic. *Journal of Materials Chemistry* 15 (2005) 947-952.

[67] B. H. Ji, and H. J. Gao. A study of fracture mechanisms in biological nano-composites via the virtual internal bond model. *Materials Science and Engineering A* 366 (2004) 96-103.

[68] X. D. Li, and P. Nardi. Micro/nanomechanical characterization of a natural nanocomposite material - the shell of Pectinidae. *Nanotechnology* 15 (2004) 211-217.

[69] W. Yang, G. P. Zhang, H. S. Liu, and X. W. Li. Microstructural characterization and hardness behavior of a biological *Saxidomus purpuratus* shell. *Journal of Materials Science and Technology* 27 (2011) 139-146.

[70] N. Nassif, N.Pinna, N. Gehrke, M. Antonietti, C. Jager, and H. Cölfen. Amorphous layer around aragonite platelets in nacre. *Proceedings of the National Academy of Sciences of the United States of America* 102 **(**2005) 12653-12655.

[71] E. Baer, A. Hiltner, and R. J. Morgan. Biological and synthetic hierarchical composites. *Physics Today* 45 (1992) 60-67.

[72] P. Ball. Life's lessons in design. *Nature* 409 (2001) 413-416.

[73] X. D. Li, and Z. W. Huang. Unveiling the formation mechanism of pseudo-single-crystal aragonite platelets in nacre. *Physical Review Letters* 102 (2009) 075502.

[74] G. S. Zhang, and X. D. Li. Uncovering aragonite nanoparticle self-assembly in nacre–a natural armor. *Crystal Growth & Design* 12 (2012) 4306-4310.

[75] L. Romana, P. Thomas, P. Bilas, J. L. Mansot, and M. Merrifiels. Use of nanoindentation technique for a better understanding of the fracture toughness of *Strombus gigas* conch shell. *Materials Characterization* 76 (2013) 55-68.

[76] C. Bignardi, M. Petraroli, and N. M. Pugno. Nanoindentations on conch shells of gastropoda and bivalvia molluscs reveal anisotropic evolution against external attacks. *Journal of Nanoscience and Nanotechnology* 10 (2010) 6453-6460.

[77] J. Chen, and S. J. Bull. Multi-cycling nanoindentation study on thin optical coatings on glass. *Journal of Physics D: Applied Physics* 41 (2008) 074009.

[78] V. Yamakov, D. Wolf, S. R. Phillpot, A. K. Mukherjee, and H. Gleiter. Dislocation processes in the deformation of nanocrystalline aluminum by molecular-dynamics simulation. *Nature* 1 (2002) 1-5.

[79] H. Van Swygenhoven, and P. M. Derlet. Grain-boundary sliding in nanocrystalline fcc metals. *Physical Review B* 64 (2001) 224105.

[80] X. D. Li, Z. H. Xu, and R. Z. Wang. In situ observation of nanograin rotation and deformation in nacre. *Nano Letters* 6 (2006) 2301-2304.

[81] R. Li, L. H. Bao, and X. D. Li. Synthesis, structural, optical and mechanical characterization of SrB_2O_4 nanorods. *CrystEngComm* 13 (2011) 5858-5862.

[82] H. Z. Li, Z. H. Xu, and X. D. Li. Multiscale hierarchical assembly strategy and mechanical prowess in conch shells (*Busycon carica*). *Journal of Structural Biology* (In press).

[83] Z. W. Huang, and X. D. Li. Origin of flaw-tolerance in nacre. *Scientific Reports* 3 (2013) 1693.

[84] H. Ni, and X. D. Li. Young's modulus of ZnO nanobelts measured using atomic force microscopy and nanoindentation techniques. *Nanotechnology* 17 (2006) 3591-3597.

[85] H. D. Espinosa, A. L. Luster, F. J. Latourte, O. Y. Loh, D. Gregoire, and P. D. Zavattieri. Tablet-level origin of toughening in abalone shells and translation to synthetic composite materials. *Nature Communications* 2 (2011) 173.

[86] L. Landau, and E. M. Lifshitz. *Theory of elasticity*. Pergamon Press, New York, 1986.

[87] H. Ni, X. D. Li, and H. S. Gao. Elastic modulus of amorphous SiO_2 nanowires. *Applied Physics Letters* 88 (2006) 043108.

[88] X. Y. Tao, L. X. Dong, X. N. Wang, and W. K. Zhang. B_4C-nanowires/carbon-microfiber hybrid structures and composites from cotton T-shirts. *Advanced Materials* 22 (2010) 2055-2059.

[89] K. Zheng, X. D. Han, L. H. Wang, Y. F. Zhang, Y. H. Yue, Y. Qin, X. N. Zhang, and Z. Zhang. Atomic mechanisms governing the elastic limit and the incipient plasticity of bending Si nanowires. *Nano Letters* 9 (2009) 2471-2476.

[90] X. D. Han, K. Zheng, Y. F. Zhang, X. N. Zhang, Z. Zhang, and Z. L. Wang. Low-temperature in situ large-strain plasticity of silicon nanowires. *Advanced Materials* 19 (2007) 2112-2118.

[91] J. W. McTigue, and H. R. Wenk. Microstructures and orientation relationships in the dry-state aragonite-calcite and calcite-lime phase transformations. *American Mineralogist* 70 (1985) 1253-1261.

[92] C. Rodriguez-Navarro, E. Ruiz-Agudo, A. Luque, A. B. Rodriguez-Navarro, and M. Ortega-Huertas. Thermal decomposition of calcite: mechanisms of formation and textural evolution of CaO nanocrystals. *American Mineralogist* 94 (2009) 578-593.

[93] L. Ba, Y. Qin, and Z. Q. Wu. Electron beam induced crystallization of a GeAu amorphous film. *Journal of Applied Physics* 80 (1996) 6170-6174.

[94] C. L. Chen, K. Arakawa, J. G. Lee, and H. Mori. Electron-irradiation-induced phase transformation in alumina. *Scripta Materialia* 63 (2010) 1013-1016.

[95] A. Kis, G. Csanyi, J. P. Salvetat, T. N. Lee, E. Couteau, A. J. Kulik, W. Benoit, J. Brugger, and L. Forro. Reinforcement of single-walled carbon nanotube bundles by intertube bridging. *Nature Materials* 3 (2004) 153-157.

[96] J. F. Zang, L. H. Bao, R. A. Webb, and X. D. Li. Electron beam irradiation stiffens zinc tin oxide nanowires. *Nano Letters* 11 (2011) 4885-4889.

[97] R. F. Egerton, P. Li, and M. Malac. Radiation damage in the TEM and SEM. *Micron* 35 (2004) 399-409.

[98] K. A. Mkhoyan, J. Silcox, M. A. Mcguire, and F. J. Disalvo. Radiolytic purification CaO by electron beams. *Philosophical Magazine* 86 (2006) 2907-2917.

[99] E. D. Cater, and P. R. Buseck. Mechanism of decomposition of dolomite, $Ca_{0.5}Mg_{0.5}CO_3$, in the electron microscope. *Ultramicroscopy* 18 (1985) 241-252.

[100] J. J. Hren, J. I. Goldstein, and D. C. Joy. *Introduction to analytical electron microscopy*. Plenum Press, New York and London, 1979.

[101] M. Davis. Size-specific predator-prey relationships between queen conch and spiny lobsters. *Proceedings of the Gulf and Caribbean Fisheries Institute* 45 (1999) 908-912.

[102] D. E. Jory, and E. S. Iversen. Queen conch predators: not a roadlock to mariculture. *Proceedings of the Gulf and Caribbean Fisheries Institute* 35 (1983) 108-111.

[103] Y. Oaki, and H. Imai, The hierarchical architecture of nacre and its mimetic material. *Angewandte Chemie-International Edition in English* 44 (2005) 6571-6575.

[104] Q. Wei, K. T. Ramesh, E. Ma, L. J. Kecskes, L. Magness, R. Dowding, V. U. Kazykhanov, and R. Z. Valiev. Mechanical behavior and dynamic failure of high-strength ultrafine grained tungsten under uniaxial compression. *Acta Materialia* 54 (2006) 77-87.

[105] Q. Wei. Strain rate effects in the ultrafine grain and nanocrystalline regimes - influence on some constitutive responses. *Journal of Materials Science* 42 (2007) 1709-1727.

[106] A. J. Kalkman, A. H. Verbruggen, and S. Radelaar. High-temperature tensile tests and activation volume measurement of free-standing submicron Al films. *Journal of Applied Physics* 92 (2002) 6612-6615.

[107] L. Lu, S. X. Li, and K. Lu. An abnormal strain rate effect on tensile behavior in nanocrystalline copper. *Scripta Materialia* 45 (2001) 1163-1169.

[108] J. W. Hutchinson, and Z. Suo. Mixed mode cracking in layered materials. *Advanced in Applied Mechanics* 29 (1992) 63-191.

[109] G. L. Hu, C. Q. Chen, K. T. Ramesh, and J. W. McCauley. Mechanisms of dynamic deformation and dynamic failure in aluminum nitride. *Acta Materialia* 60 (2012) 3480-3490.

[110] M. Y. He, and J. W. Hutchinson. Crack deflection at an interface between dissimilar elastic materials. *International Journal of Solids and Structures* 25 (1989) 1053-1067.

[111] A. Aryaei, A. H. Jayatissa, and A. C. Jayasuriya. Nano and micro mechanical properties of uncross-linked and cross-linked chitosan films. *Journal of the Mechanical Behavior of Biomedical Materials* 5 (2012) 82-89.

[112] V. Prakash, and N. Mehta. Uniaxial compression and combined compression-and-shear response of amorphous polycarbonate at high loading rates. *Polymer Engineering & Science* 52 (2012) 1217-1231.

[113] M. Upmanyu, D. J. Srolovitz, A. E. Lobkovsky, J. A. Warren, and W. C. Carter. Simultaneous grain boundary migration and grain rotation. *Acta Materialia* 54 (2006) 1707-1719.

[114] S. Kumar, X. Li, A. Haque, and H. Gao. Is stress concentration relevant for nanocrystalline metals? *Nano Letters* 11 (2011) 2510-2516.

[115] H. Van Swygenhoven. Grain boundaries and dislocations. *Science* 296 (2002) 66-67.

[116] E. M. Bringa, A. Caro, Y. Wang, M. Victoria, J. M. McNaney, B. A. Remington, R. F. Smith, B. R. Torralva, and H. Van Swygenhoven. Ultrahigh strength in nanocrystalline materials under shock loading. *Science* 309 (2005) 1838-1841.

[117] S. Yip. The strongest size. *Nature* 391 (1998) 532-533.

[118] Z. Shan, E. A. Stach, M. K. Wiezorek, J. A. Knapp, D. M. Follstaedt, and S. X. Mao. Grain boundary-mediated plasticity in nanocrystalline nickel. *Science* 305 (2004) 654-657.

[119] P. Brownell, and R. D. Farley. Prey-localizing behavior of the nocturnal desert scorpion, Paruroctonus mesaensis: orientation to substrate vibrations. *Animal Behaviour* 27 (1979) 185-193.

[120] J. S. Rudwick. Sensory spines in the Jurassic brachiopod *Acanthothiris*. *Palaeontology* 8 (1965) 604-617.

[121] A. Checa, and D. Martin-Ramos. Growth and function of spines in the Jurassic ammonite *Aspidoceras*. *Palaeontology* 32 (1989) 645-655.

[122] D. E. Jory, and E. S. Iverson. Shell strength of queen conch, *Strombus gigas* L: aquaculture implications. *Aquaculture and Fishery Management* 19 (1988) 45-51.

[123] E. S. Iverson, S. P. Bannerot, and D. E. Jory. Evidence of survival value related to burying behavior in queen conch *Strombus gigas*. *Fishery Bulletin* 88 (1990) 383-387.

[124] G. Karambelas, S. Santhanam, and Z. N. Wing. Strombus gigas inspired biomimetic ceramic composites via SHELL-Sequential Hierarchical Engineered Layer Lamination. *Ceramics International* 39 (2013) 1315-1325.

[125] A. G. Evans, and F. W. Zok. The physics and mechanics of fiber-reinforced brittle-matrix composites. *Journal of Materials Science* 29 (1994) 3857-3896.

[126] S. Baskaran, S. D. Nunn, D. Popovic, and J. W. Halloran. Fibrous monolithic ceramics: I, fabrication, microstructure, and indentation behavior. *Journal of the American Chemical Society* 76 (1993) 2209-2216.

[127] L. Chen, R. Ballarini, H. Kahn, and A. H. Heuer. Bioinspired micro-composite structure. *Journal of Materials Research* 22 (2007) 124-131.

[128] V. S. Kaul, and K. T. Faber. Synthetic crossed-lamellar microstructures in oxide ceramics. *Journal of Ceramic Processing Research* 6 (2005) 218-222.

[129] C. Salinas, and D. Kisailus. Fracture mitigation strategies in gastropod shells. *JOM* 65 (2013) 473-480.

[130] H. O. Fabritius, C. Sachs, P. R. Triguero, and D. Raabe. Influence of structural principles on the mechanics of a biological fiber-based composite material with hierarchical organization: the exoskeleton of the lobster (*Homarus americanus*). *Advanced Materials* 21 (2009) 391-400.

[131] P. Lawrence. Some theoretical considerations of fibre pull-out from an elastic matrix. *Journal of Materials Science* 7 (1972) 1-6.

[132] X. Y. Chen, I. J. Beyerlein, and L. C. Brinson. Curved-fiber pull-out model for nanocomposites. Part 2 Interfacial debonding and sliding. *Mechanics of Materials* 41 (2009) 293-307.

[133] Q. Chen, and N. M. Pugno. Bio-mimetic mechanisms of natural hierarchical materials: a review. *Journal of the Mechanical Behavior of Biomedical Materials* 19 (2013) 3-33.

[134] X. F. Yang. A self-constraint strengthening mechanism and its application to seashells. *Journal of Materials Research* 10 (1995) 1485-1490.

[135] S. Mann. Molecular recognition in biomineralization. *Nature* 332 (1988) 119-124.

[136] S. Sudo, T. Fujikawa, T. Nagakura, T. Ohkubo, K. Sakaguchi, M. Tanaka, K. Nakashima, and T. Takahashi. Structures of mollusk shell framework proteins. *Nature* 387 (1997) 563-564.

[137] R. Knitter, C. Odemer, and J. Haubelt. Thermal investigation on abalone nacre. *Ceramic Forum International* 85 (2008) 38-42.

[138] S. Weiner, I. Sagi, and L. Addadi. Choosing the crystallization path less traveled. *Science* 309 (2005) 1027-1028.

[139] L. Yang, C. E. Killian, M. Kunz, N. Tamura, and P. U. P. A. Gilbert. Biomineral nanoparticles are space-filling. *Nanoscale* 3 (2011) 603-609.

[140] D. R. Dasgupta. The oriented transformation of aragonite into calcite. *Mineralogical Magazine* 33 (1964) 924-928.

[141] Z. W. Huang, and X. D. Li. Nanoscale structural and mechanical characterization of heat treated nacre. *Materials Science and Engineering C* 29 (2009) 1803-1807.

[142] A. Singh, S. Dash, M. Kamruddin, P. K. Ajikumar, A. K. Tyagi, V. S. Raghunathan, and B. Raj. Formation of nanocrystalline calcia by the decomposition of calcite. *Journal of American Ceramic Society* 85 (2002) 927-932.

[143] S. Weiner, W. Traub, and S. B. Parker. Macromolecules in mollusc shells and their functions in biomineralization. *Philosophical Transactions of the Royal Society of London B* 304 (1984) 425-434.